CALCULATION OF COUPLING BETWEEN TAPERED FIBER MODES AND WHISPERING-GALLERY MODES OF A SPHERICAL MICROLASER

By

MICHAEL JOSEPH HUMPHREY

Bachelor of Science
University of Maryland
College Park, Maryland
1994

Submitted to the Faculty of the
Graduate College of the
Oklahoma State University
in partial fulfillment of
the requirements for
the Degree of
DOCTOR OF PHILOSOPHY
July 2004

CALCULATION OF COUPLING BETWEEN TAPERED FIBER MODES AND WHISPERING-GALLERY MODES OF A SPHERICAL MICROLASER

Thesis Approved:

Donna K. Bandy
Thesis Advisor

Albert T. Rosenberger

Paul A. Westhaus

Don H. Adams

Al Carlozzi
Dean of the Graduate College

ACKNOWLEDGMENTS

I would like to thank all of the people who have helped to make this possible. I thank my family for their support and encouragement.

I thank my advisor Dr. Donna K. Bandy, for her guidance, support, and encouragement. Without her, this certainly would not have been accomplished. She has provided me with opportunities to study interesting physics and to direct the research of several undergraduates over the years.

I would like to thank Dr. Albert T. Rosenberger who has been very generous with his help and support, far beyond the call of duty, and who has provided me with excellent opportunities to learn about optics.

I also would like to express my sincere appreciation to Prof. Paul Westhaus for recruiting me into the Physics Department and his assistance during my study at Oklahoma State University.

I thank Dr. Don H. Adams for serving on my committee and providing analogies between optical and mechanical systems.

I thank the other members of the research group for their help and discussions about the research. In particular, I would like to thank Dr. Ahmer Naweed, George Farca, and Siyka Shopova. I especially thank Elijah Dale for his help in automating and running computer programs.

I would like to thank the rest of the faculty and staff of the Physics Department, especially the office staff.

Finally, I thank the Physics Department for providing the opportunity for my graduate study and part of my financial support. Further financial support was provided by the

Oklahoma Center for the Advancement of Science and Technology, Project Nos. AR012-064 and AR022-052, and by the National Science Foundation, Award Nos. ECS-0115442 and ECS-0329924.

TABLE OF CONTENTS

LIST OF TABLES

Table Page

LIST OF FIGURES

Figure Page

Figure Page

CHAPTER 1

INTRODUCTION

Whispering-gallery modes (WGMs) are the natural electromagnetic eigenmodes of solid spheres with large radial and azimuthal indices. They are activated by external coherent signals and propagate around the equator of the spherical shaped object spatially confined by total internal reflection to a narrow region near the surface. They are elemental to understanding many of the newly defined, extremely small resonators. The origin of WGMs is rooted in the surround sound of acoustical whisperings within old architectures and the combination of curiosity and sequential development of first principles of physics.

There is a famous historical monument in Peking, China, called the Temple of the Sky where "miracles" occur. Associated with this temple is a rugged wall of stone that roughly forms the shape of a closed cylinder. The miracle is that low utterances of a person, spoken while facing one direction along the wall, return back moments later to that person as if someone just behind the speaker *whispered* exactly the same sounds. In the 19th century Lord Rayleigh[1] proposed a physical explanation for this whisper on the basis of his own experiments in an ancient gallery located at St. Paul's Cathedral in London, England. Under the dome of this cathedral, whispers spoken in one direction returned to the speaker after a small delay just as in the case of the wall of stone in China. Early wave theory explained the reflection of acoustic "rays", but it was Lord Rayleigh who proposed the propagation of these waves along the spherical structure. His experiment involved a whistle as a sound source and a burning candle as a detector. The 20th century brought a better understanding of electromagnetic waves and knowledge of their existence as spatial structures within spherical solid objects primarily through comparison with their acoustical counterpart.

Whispering-gallery modes are a specific class of spherical modes that are used to study many optical problems. Understanding their operating features is important for the development of any system that incorporates them. Mathematical representation of natural modes in dielectric spheres is generally attributed to Mie[2] and Debye,[3] but the detailed study of WGMs is the result of the works by Richtmyer[4] and Stratton.[5] More recently, L. A. Vainstein provided important new insights into the theory of WGMs.[6]

Renewed interest in WGMs has inspired creative investigations into many different microtechnologies.[7–39] Microspheres, in particular, are very appealing objects because of the small effective volumes of their WGMs and their high-Q factors.[7–9] Fused-silica microspheres have extremely low WGM losses that make them better suited as high-Q microresonators.[8,37] Such microresonators are shown to have potential use in many areas, including cavity quantum electrodynamics,[18] laser stabilization,[13] microlasers,[39–41] nonlinear optics,[10,22,23] and evanescent-wave sensing.[24,42] The utility of a microsphere resonator can be limited because of the morphology dependence of the resonant frequencies of the WGMs – i.e., the resonant frequencies are fixed by the geometry of the sphere and thus not easily tunable. However, experimental advances in compression tuning[43–45] and locking of microsphere WGM resonances[44,45] have improved these conditions by providing for tuning over a greater range with faster response. Many of these optical systems employ the technique of coupling light into and out of the WGMs of the microspheres by using modes of tapered optical fibers (see Fig. 1.1). Although common, this technique brings light to experimental challenges that are associated with less than ideal conditions in the coupling process.

Tapering a fiber, by any of several methods, introduces some interesting effects that must be considered. The fiber configuration often used is the bitaper. A bitaper consists of a non-tapered portion of the fiber at the first end. This is followed by a taper transition region where the radius of the fiber decreases with distance. The portion of the fiber after the transition is known as the taper. This is followed by a second taper transition region of increasing fiber radius and ends with another non-tapered portion. The non-tapered portion of a single-mode fiber is designed to support only the fundamental mode because of the small size of the core relative to the transmission wavelength and because of the low index

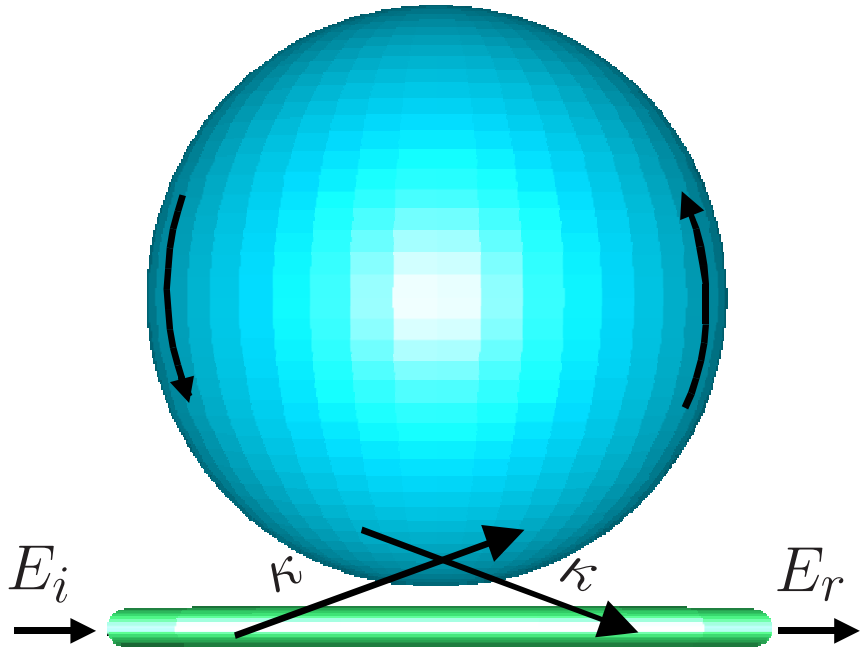

Figure 1.1. Microsphere-Fiber System

contrast between the core and the cladding. However, in the tapered portion of the fiber, the light is guided by the cladding-air interface and thus the tapered fiber can support multiple modes. In an ideal adiabatic taper transition, the taper angle is small enough so that the fundamental HE_{11} mode can be considered unperturbed as it evolves from being core guided to cladding guided. Within a non-ideal or non-adiabatic taper transition, the cladding guided HE_{11} mode couples to higher-order fiber modes of the same symmetry. The next higher-order fiber mode in the same family is the HE_{12} mode. Before coupling to the microsphere, the only modes in the tapered portion of the fiber are these two modes, if the taper transition is sufficiently adiabatic. After coupling with the microsphere, other higher-order fiber modes may be present. This is because the microsphere mode may couple to any mode supported by the taper. The radius of the tapered portion of the fiber can be chosen to maximize the coupling of the fiber HE_{11} mode to the microsphere mode, while minimizing the losses incurred by the coupling of the microsphere's WGM to the higher-order fiber modes of different families, because the light in these fiber modes does not couple back into the HE_{11} mode at the transmission end of the bitaper. Early arguments[30,46] assume that optimal coupling is accomplished by phase matching the microsphere mode to the fundamental

fiber mode. However, in agreement with other recent results, [47] it is actually accomplished by tapering the fiber to a smaller radius than that for phase matching.

Calculation of the WGM spectra for modes of different radial order q and polar order $l - |m|$ includes non-ideal factors that are present under experimental conditions. In practice, the microsphere usually has an eccentricity. This eccentricity removes the frequency degeneracy of the polar modes. Also, the fact that the tapered fiber may not be exactly aligned with the equatorial plane of the microsphere increases the number of WGMs to which the fiber may couple. With perfect alignment, only the even (symmetric) polar modes of the microsphere are excited. With imperfect alignment, both the odd (antisymmetric) and even polar modes are excited. Presented here are calculations that detail the effects of varying the size of the tapered-fiber radius and explore the WGM spectra associated with the non-ideal aspects of an experiment.

Chapter 2 describes waveguides and their electromagnetic modes. In particular, fused-silica microspheres and fibers are treated. For microspheres, the spectra of their modes are discussed. For fibers, comparisons are made between traditional fiber modes and the modes of tapered fibers.

Chapter 3 describes mode coupling. The discussion includes an introduction to coupled mode theory. This is followed by the application of coupled mode theory to the fiber-microsphere system, and also to the tapered fiber.

Chapter 4 describes applications of the coupled-mode analysis in the fiber-microsphere system. Included are calculations of optimal fiber radius, WGM spectra, and a discussion of microsphere lasing.

Chapter 5 concludes by summarizing the results and highlighting some of the interesting physics encountered in this study.

CHAPTER 2

WAVEGUIDES

2.1 Ray Picture

The easiest way to describe the operation of a waveguide is with the ray picture. Waveguides consist of a material of higher index of refraction surrounded by a material of lower index of refraction. From Snell's Law, it is known that if the angle of incidence of a ray originating from the higher index side of an interface is above a certain critical angle, then the ray will be reflected by total internal reflection. A fused-silica microsphere has an index of 1.44 which is surrounded either by the index of air ($n_{\text{air}} = 1.00$) or by that of a liquid (e.g., $n_{\text{methanol}} = 1.33$ for use in a liquid sensing measurement). Light, once inside a microsphere, travels around its equator by making numerous reflections. Because a microsphere is a cavity as well as a waveguide, the light forms a mode when the round-trip pathlength is a multiple of the light's wavelength. This is shown in Fig. 2.1, where the blue circle represents the surface of the microsphere and the red line represents the path of the internally reflected light. In this case, the mode consists of eight reflections of the light. A common type of optical fiber is the step-index fiber. This consists of a core of slightly higher index and a cladding of slightly lower index. Like in the microsphere case, light travels along the fiber by making numerous reflections at the core-cladding interface. This is shown in Fig. 2.2. The blue lines represent the surface of the fiber and the red line represents the path of the internally reflected light. Although the ray picture is useful for understanding the basic operation of waveguides, it has recently been shown that it is unreliable for performing calculations.[48] For accurate calculations and predictions to be made, the wave nature of the light must be considered.

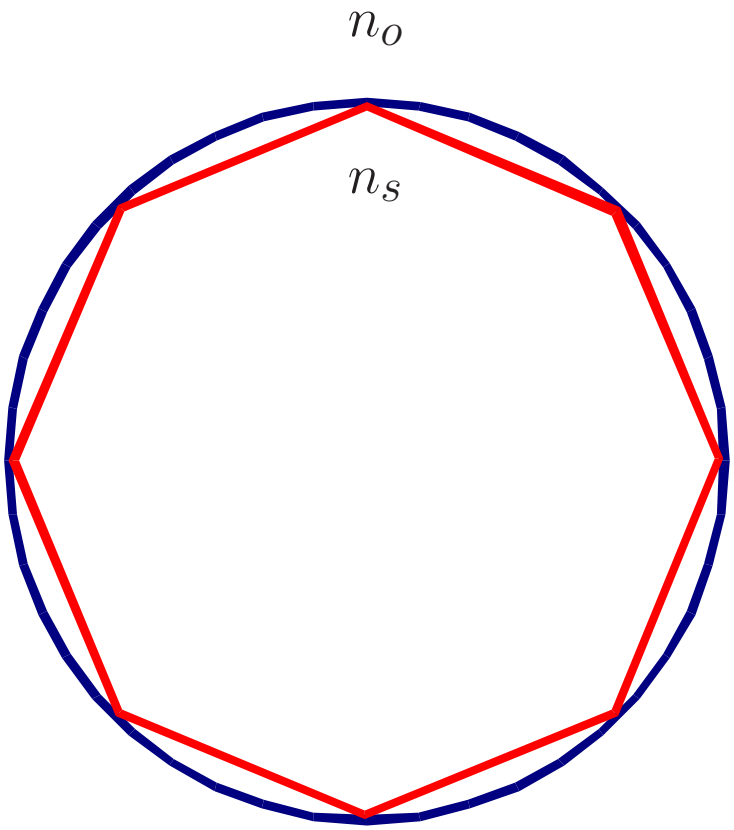

Figure 2.1. WGM Ray Trace. The blue circle represents the surface of the microsphere and the red line represents the path of the internally reflected light. n_s and n_o are the indices of refraction of the microsphere and the surrounding medium, respectively. In this case the mode consists of eight reflections of the light.

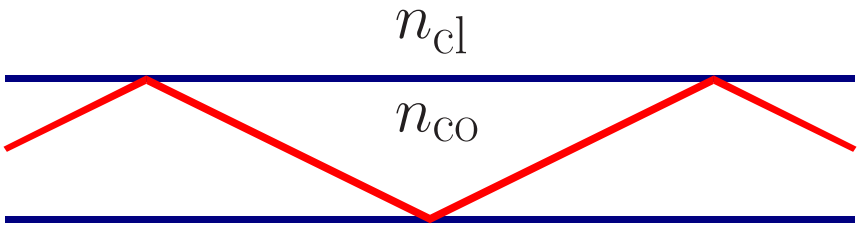

Figure 2.2. Step-Index Fiber Ray Trace. The blue lines represent the surface of the fiber and the red line represents the path of the internally reflected light. n_{co} and n_{cl} are the indices of refraction of the core and cladding, respectively.

2.2 Unguided and Guided Wave Propagation

The fundamental requirement for an electromagnetic wave to propagate is that its fields satisfy the wave equation

$$\nabla^2\mathbf{E} - \mu\epsilon\frac{\partial^2\mathbf{E}}{\partial t^2} = \mu\frac{\partial^2\mathbf{P}}{\partial t^2}, \tag{2.1}$$

where $\mathbf{E}$, $\mathbf{P}$, t, c, μ, and ϵ are the electric field, polarization, time, speed of light, permeability, and permittivity, respectively, in the SI system of units. The bold variables represent vector quantities. For a medium that is not polarized, the wave equation is

$$\nabla^2\mathbf{E} - \mu\epsilon\frac{\partial^2\mathbf{E}}{\partial t^2} = 0. \tag{2.2}$$

The simplest solution of this is the plane wave in vacuum,

$$\mathbf{E}(\mathbf{r},t) = \mathbf{E_0}e^{i(\omega_0 t - \mathbf{k_0}\cdot\mathbf{r})}, \tag{2.3}$$

where ω_0 is the angular frequency of the light and $\mathbf{k_0} = \frac{\omega_0}{c}\hat{\mathbf{k}}$ is the wave vector. However, even in free space, electromagnetic wave profiles do vary in the plane transverse to the direction of propagation. The electric field for a wave traveling in free space is transverse to the direction of propagation (as long as the beam diameter is large compared to the wavelength). In this case, the electric field can be expressed as

$$E(x,y,z) = E_0\psi(x,y,z)e^{-ik_0 z}. \tag{2.4}$$

Substitution of this into the wave equation, and assuming that ψ is slowly varying in z, results in

$$\nabla_t^2\psi - i2k_0\frac{\partial\psi}{\partial z} = 0, \tag{2.5}$$

where ∇_t^2 is the transverse Laplacian for divergence. Gaussian modes are one particularly useful set of solutions of the wave equation under this condition and light propagates with these modes as Gaussian beams. Equation (2.5) has the same form as the Schrödinger equation. Just as solutions to the Schrödinger equation are discrete in form, families of solutions of the Maxwell wave equation are also discrete in form. Analogies between optical systems and quantum mechanical systems are helpful in describing waveguides, and later, the microsphere-fiber system.

The fields for a waveguide are calculated using the same basic principle as those in free-space. However, there are two important differences. One is that the longitudinal components cannot be assumed to be small relative to the transverse components. This is because of the beam confinement possible in a waveguide (especially in the case of a

tapered fiber) and also, the presence of the index change. The other difference is that special attention must be paid to the boundary conditions of the electric and magnetic fields.

The first step in determining the fields of a waveguide is to write the expressions for the boundary conditions of the fields. This is analogous to a particle in a potential well. The particle's wavefunction has one form for the interior region and another form for the exterior region. The electric and magnetic fields of a waveguide also have different forms for the interior and exterior portions. The exterior portion of the field is known as the evanescent part. From the boundary conditions, a characteristic equation is obtained. The roots of the characteristic equation provide the propagation constants of the allowed modes. The propagation constant β is basically the effective wavenumber and can be expressed as

$$\beta = \frac{n_{\text{eff}}\omega}{c}, \tag{2.6}$$

where n_{eff} is the effective index of refraction. Modes of a waveguide have a dependence of $e^{-i\beta z}$ in the direction of propagation. The higher the order of the mode in a waveguide, the lower the propagation constant. This corresponds to the mode traveling faster along the waveguide. This is because the higher-order modes have a higher fraction of their energy contained in the evanescent part of the field. In a fiber, the fundamental mode has an effective index close to that of the core, while the highest-order mode has an effective index close to that of the cladding.

2.3 Microsphere Modes

There are two kinds of microsphere modes - transverse magnetic (TM) and transverse electric (TE). In the case of TM modes, the magnetic field is tangent to the surface of the sphere and perpendicular to the direction of propagation. The electric field thus has components normal to the surface of the sphere and parallel to the direction of propagation. In the case of TE modes, these properties are reversed. With the use of the scalar Debye potentials,[49,50] the solutions to the Maxwell equations become

$$\frac{\partial^2 U}{\partial r^2} + \frac{1}{r^2\cos\theta}\frac{\partial}{\partial\theta}\left(\cos\theta\frac{\partial U}{\partial\theta}\right) + \frac{1}{r^2\cos^2\theta}\frac{\partial^2 U}{\partial\phi^2} + k^2 U = 0, \quad \text{TM Modes}, \tag{2.7a}$$

$$\frac{\partial^2 V}{\partial r^2} + \frac{1}{r^2\cos\theta}\frac{\partial}{\partial\theta}\left(\cos\theta\frac{\partial V}{\partial\theta}\right) + \frac{1}{r^2\cos^2\theta}\frac{\partial^2 V}{\partial\phi^2} + k^2 V = 0, \quad \text{TE Modes}, \tag{2.7b}$$

where U and V are the scalar potentials and $k = \frac{\omega}{c}$. Here, the convention is used that the angle θ is zero at the equator rather than the north pole. The electric and magnetic fields are found from the scalar potentials:

$$\left.\begin{aligned} E_r &= \left(\frac{\partial^2}{\partial r^2} + k^2\right)U, & H_r &= 0, \\ E_\theta &= \frac{1}{r}\frac{\partial^2 U}{\partial r \partial \theta}, & H_\theta &= -ik\frac{1}{r}\frac{\partial U}{\partial \phi}, \\ E_\phi &= \frac{1}{r\cos\theta}\frac{\partial^2 U}{\partial r \partial \phi}, & H_\phi &= ik\frac{1}{r}\frac{\partial U}{\partial \theta}, \end{aligned}\right\} \text{TM Modes} \tag{2.8}$$

$$\left.\begin{aligned} H_r &= \left(\frac{\partial^2}{\partial r^2} + k^2\right)V, & E_r &= 0, \\ H_\theta &= \frac{1}{r}\frac{\partial^2 V}{\partial r \partial \theta}, & E_\theta &= ik\frac{1}{r}\frac{\partial V}{\partial \phi}, \\ H_\phi &= \frac{1}{r\cos\theta}\frac{\partial^2 V}{\partial r \partial \phi}, & E_\phi &= -ik\frac{1}{r}\frac{\partial V}{\partial \theta}. \end{aligned}\right\} \text{TE Modes} \tag{2.9}$$

The fields are separable and can be expressed as

$$\Psi_{qlm}(r,\theta,\phi) = N_s \psi_r(r)\psi_\theta(\theta)\psi_\phi(\phi), \tag{2.10}$$

where Ψ is the electric field in the case of TE modes and is the magnetic field in the case of TM modes. N_s is a normalization constant. The subscripts indicate the order of the mode (q is the radial mode order, found from the boundary conditions, and the difference between l and $|m|$ is the polar mode order). From the above, the differential equations for the dependences on the coordinates are

$$\frac{d^2}{dr^2}\psi_r + \frac{2}{r}\frac{d}{dr}\psi_r + \left(k^2 n_s^2 - \frac{l(l+1)}{r^2}\right)\psi_r = 0, \tag{2.11a}$$

$$\frac{1}{\cos\theta}\frac{d}{d\theta}\left(\cos\theta\frac{d}{d\theta}\psi_\theta\right) - \frac{m^2}{\cos^2\theta}\psi_\theta + l(l+1)\psi_\theta = 0, \tag{2.11b}$$

$$\frac{d^2\psi_\phi}{d\phi^2} + m^2\psi_\phi = 0. \tag{2.11c}$$

The solutions are found to be

$$\psi_r(r) = \begin{cases} j_l(kn_s r), & r \le R_s, \\ h_l(kn_s r), & r > R_s, \end{cases} \tag{2.12a}$$

$$\psi_\theta(\theta) = P_l^m(\sin\theta), \tag{2.12b}$$

$$\psi_\phi(\phi) = e^{\pm im\phi}, \tag{2.12c}$$

where j_l and h_l are the spherical Bessel functions of first kind and spherical Hankel functions (also known as Bessel functions of third kind), respectively. P_l^m are the associated Legendre polynomials, and R_s is the radius of the sphere. The characteristic equations found from the continuity conditions are

$$\left.\begin{aligned}\frac{\left[(kR_s)^{1/2}J_\nu(kR_s)\right]'}{(kR_s)^{1/2}J_\nu(kR_s)} &= \left(\frac{\epsilon}{\mu}\right)^{1/2}\frac{\left[(k_0R_s)^{1/2}H_\nu^{(1)}(k_0R_s)\right]'}{(k_0R_s)^{1/2}H_\nu^{(1)}(k_0R_s)},\end{aligned}\right\}\ \text{TM Modes} \tag{2.13a}$$

$$\left.\begin{aligned}\frac{\left[(kR_s)^{1/2}J_\nu(kR_s)\right]'}{(kR_s)^{1/2}J_\nu(kR_s)} &= \left(\frac{\mu}{\epsilon}\right)^{1/2}\frac{\left[(k_0R_s)^{1/2}H_\nu^{(1)}(k_0R_s)\right]'}{(k_0R_s)^{1/2}H_\nu^{(1)}(k_0R_s)},\end{aligned}\right\}\ \text{TE Modes} \tag{2.13b}$$

where $\nu = l + 1/2$ relates the spherical Bessel functions j_l and h_l to the regular Bessel functions J_ν and H_ν

For the sphere sizes considered in this study, the values of l and $|m|$ are large. The computation of the spherical Bessel functions and Associated Legendre Polynomials becomes time consuming under these conditions. The computation time is greatly reduced by approximating the spherical Hankel function as an exponential, and the Associated Legendre Polynomials with Hermite-Gauss functions. The forms of the fields as used in the calculations are[32]

$$\psi_r(r) = \begin{cases} j_l(kn_sr), & r \le R_s, \\ j_l(kn_sR_s)e^{-\alpha_s(r-R_s)}, & r > R_s, \end{cases} \tag{2.14a}$$

$$\psi_\theta(\theta) = H_N\left(\sqrt{m}\theta\right)e^{-\frac{m}{2}\theta^2}, \qquad m \gg 1 \gg \theta, \tag{2.14b}$$

$$\psi_\phi(\phi) = e^{\pm im\phi}, \tag{2.14c}$$

where

$$\alpha_s = \sqrt{\beta_l^2 - k^2n_o^2}, \qquad \beta_l = \frac{\sqrt{l(l+1)}}{R_s},$$
$$N = l - |m|.$$

For TE modes,

$$E_\theta(r,\theta,\phi) = \Psi_{qlm}(r,\theta,\phi). \tag{2.15}$$

Because the transverse electric field is parallel to the surface of the microsphere, $E_\phi = 0$ and the total electric field is given by

$$\mathbf{E}(r,\theta,\phi) = E_\theta(r,\theta,\phi)\hat{\theta}. \tag{2.16}$$

For TM modes,

$$H_\theta(r,\theta,\phi) = \Psi_{qlm}(r,\theta,\phi), \tag{2.17}$$

and the electric field is given by

$$\begin{aligned}\mathbf{E}(r,\theta,\phi) &= -i\frac{1}{\omega\epsilon_o n^2}\nabla\times\hat{\theta}H_\theta \\ &= -i\frac{1}{\omega\epsilon_o n^2}\left(i\frac{m}{r\cos\theta}H_\theta\hat{r} + \left(\frac{1}{r}H_\theta + \frac{d}{dr}H_\theta\right)\hat{\phi}\right).\end{aligned} \tag{2.18}$$

The characteristic equation is found to be

$$\left(\eta_s\alpha_s + \frac{l}{R_s}\right) j_l(kn_sR_s) = kn_s j_{l+1}(kn_sR_s), \tag{2.19}$$

where

$$\eta_s = \begin{cases} 1, & \text{TE Modes,} \\ \dfrac{n_s^2}{n_o^2}, & \text{TM Modes.}\end{cases}$$

A plot of a microsphere TE mode is shown in Fig. 2.3. In this plot, the color change indicates the surface of the sphere.

The propagation constant for a microsphere is

$$\beta_m = \frac{m}{R_s}. \tag{2.20}$$

This can be explained using the ray picture. For a fundamental polar mode, where $l = m$, an integer number of wavelengths fit along the circumference of the microsphere, or

$$l = \frac{2\pi R_s n_{\text{eff}}}{\lambda}, \tag{2.21}$$

where λ is the vacuum wavelength. As the value of m is decreased, the polar mode order is increased. In this case, under the ray picture, the path of the light travels along a "zig-zag" path instead of directly along the greater circle of the microsphere. The propagation constant along the actual path is

$$\beta_l = \frac{\sqrt{l(l+1)}}{R_s}. \tag{2.22}$$

The propagation constant β_m is the projection of β_l along the circumference.

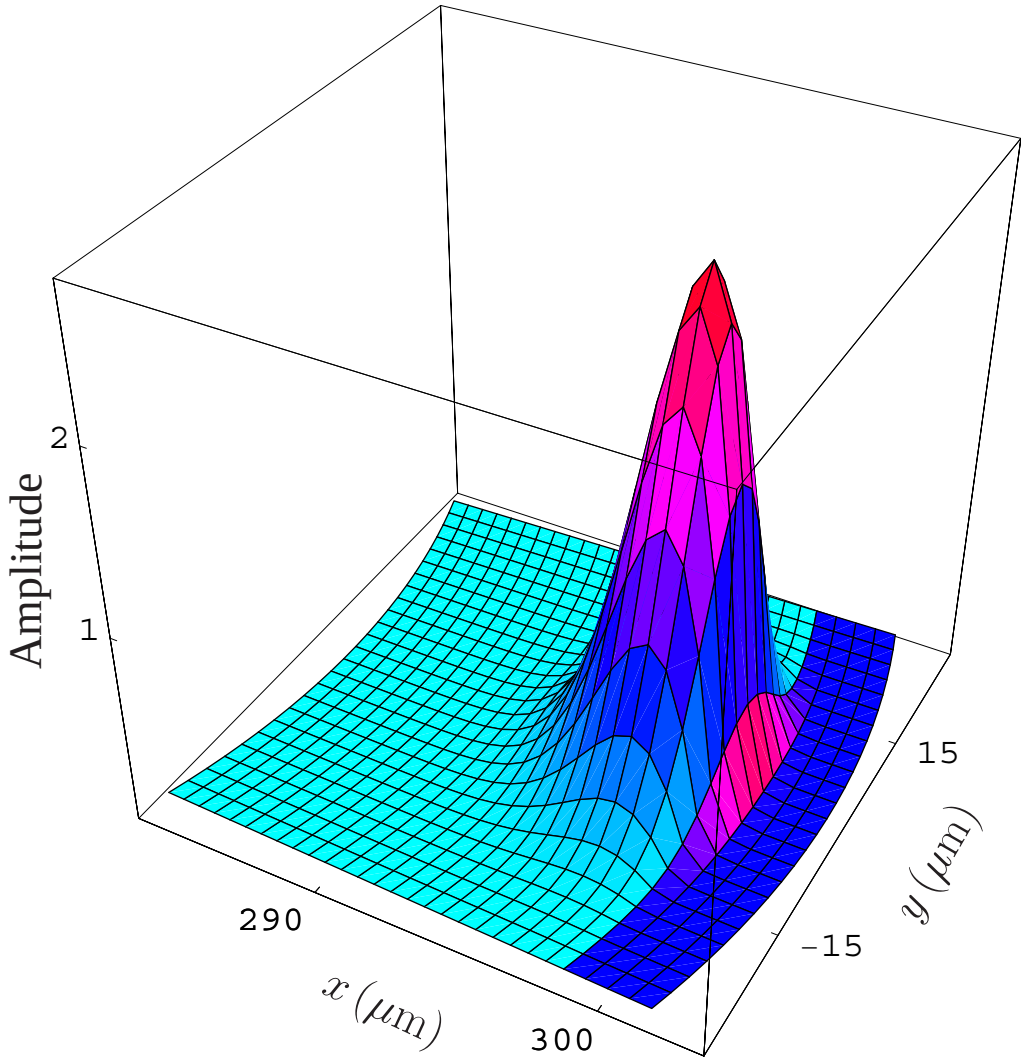

Figure 2.3. Fundamental Microsphere TE Mode ($R_s = 300\,\mu\text{m}$, $\lambda = 1550\,\text{nm}$, $q = 1$, $l = m = 1730$). The surface of the sphere is indicated by the color change. The equator is at $y = 0$.

In perfectly spherical microspheres, the polar modes are frequency degenerate. This degeneracy is broken by introducing an eccentricity to the microsphere. The frequencies of WGMs in such microspheres are given by[13,51]

$$\nu^i_{qlm} \cong \delta\left[l + \frac{1}{2} + a_q\left(\frac{l+1/2}{2}\right)^{1/3} - \Delta^i \pm \varepsilon^2\left(\frac{l-|m|}{2}\right)\right], \tag{2.23}$$

where i denotes TE or TM, $\delta = c/2\pi R_s n_s$ is the microsphere's nominal free-spectral range, a_q is the absolute value of the q^{th} zero of the Airy function, $\Delta^{\text{TE}} = n/\sqrt{n^2-1}$, and $\Delta^{\text{TM}} = \left(n\sqrt{n^2-1}\right)^{-1}$, where $n = n_s/n_o$; the positive sign is used for an oblate spheroid

and the negative sign for the prolate case, where the eccentricity is given in terms of the ellipsoid major and minor radii R_+ and R_- as $\varepsilon^2 = \left(R_+^2 - R_-^2\right)/R_+^2$.[13] The different forms of Δ^i give the polarization shift of the WGM frequencies.

2.4 Fiber Modes

The fields of fiber modes are calculated by solving the wave equation in cylindrical coordinates.[52] The direction of propagation is taken to be the z-direction. The wave equation in the longitudinal direction is

$$\left(\nabla^2 + k^2\right) \begin{pmatrix} E_z \\ H_z \end{pmatrix} = 0, \tag{2.24}$$

where

$$\nabla^2 = \frac{\partial^2}{\partial r^2} + \frac{1}{r}\frac{\partial}{\partial r} + \frac{1}{r^2}\frac{\partial^2}{\partial \theta^2} + \frac{\partial^2}{\partial z^2}. \tag{2.25}$$

Assuming that the waves are harmonic, the wave equation in the longitudinal direction is now

$$\left(\frac{\partial^2}{\partial r^2} + \frac{1}{r}\frac{\partial}{\partial r} + \frac{1}{r^2}\frac{\partial^2}{\partial \theta^2} + \left(k^2 - \beta^2\right)\right) \begin{pmatrix} E_z \\ H_z \end{pmatrix} = 0. \tag{2.26}$$

The solutions are separable and take the form

$$\begin{pmatrix} E_z \\ H_z \end{pmatrix} = \psi(r) e^{\pm il\theta}, \qquad l = 0, 1, 2, ..., \tag{2.27}$$

so that the wave equation is

$$\frac{\partial^2 \psi}{\partial r^2} + \frac{1}{r}\frac{\partial \psi}{\partial r} + \left(k^2 - \beta^2 - \frac{l^2}{r^2}\right)\psi = 0, \tag{2.28}$$

which is the Bessel differential equation. For the modes to be confined and finite, the solutions take the form

$$\psi(r) = \begin{cases} cJ_l(hr), & k^2 - \beta^2 > 0, \\ cK_l(qr), & k^2 - \beta^2 < 0, \end{cases} \tag{2.29}$$

where

$$h^2 = k^2 - \beta^2,$$
$$q^2 = \beta^2 - k^2.$$

Here, h and q are the magnitudes of the vectors $\mathbf{h} = \mathbf{k} - \boldsymbol{\beta}$ and $\mathbf{q} = \boldsymbol{\beta} - \mathbf{k}$. Thus, they indicate the deviations of the wave vectors from the propagation vector.

The fibers used in this study have a circular step-index profile

$$n(r) = \begin{cases} n_1, & \text{for} \quad r < R_f, \\ n_2, & \text{for} \quad r > R_f, \end{cases} \tag{2.30}$$

where R_f is the radius of the core. The exact solutions for the modes of such fibers are given by (see Appendix A)

core ($r < R_f$):

$$E_r = -\frac{i\beta}{h^2}\left(AhJ_l'(hr) + \frac{i\omega\mu l}{\beta r}BJ_l(hr)\right)\cos(\omega t + l\theta - \beta z), \tag{2.31a}$$
$$E_\theta = \frac{\beta}{h^2}\left(\frac{il}{r}AJ_l(hr) - \frac{\omega\mu}{\beta}BhJ_l'(hr)\right)\sin(\omega t + l\theta - \beta z), \tag{2.31b}$$
$$E_z = AJ_l(hr)\cos(\omega t + l\theta - \beta z), \tag{2.31c}$$

$$H_r = \frac{\beta}{h^2}\left(BhJ_l'(hr) - \frac{i\omega\epsilon_1 l}{\beta r}AJ_l(hr)\right)\sin(\omega t + l\theta - \beta z), \tag{2.31d}$$
$$H_\theta = -\frac{i\beta}{h^2}\left(\frac{il}{r}BJ_l(hr) + \frac{\omega\epsilon_1}{\beta}AhJ_l'(hr)\right)\cos(\omega t + l\theta - \beta z), \tag{2.31e}$$
$$H_z = BJ_l(hr)\cos(\omega t + l\theta - \beta z), \tag{2.31f}$$

and cladding ($r > R_f$):

$$E_r = \frac{i\beta}{q^2}\left(CqK_l'(qr) + \frac{i\omega\mu l}{\beta r}DK_l(qr)\right)\cos(\omega t + l\theta - \beta z), \tag{2.32a}$$

$$E_\theta = -\frac{\beta}{q^2}\left(\frac{il}{r}CK_l(qr) - \frac{\omega\mu}{\beta}DqK_l'(qr)\right)\sin(\omega t + l\theta - \beta z), \tag{2.32b}$$

$$E_z = CK_l(qr)\cos(\omega t + l\theta - \beta z), \tag{2.32c}$$

$$H_r = -\frac{\beta}{q^2}\left(DqK_l'(qr) - \frac{i\omega\epsilon_2 l}{\beta r}CK_l(qr)\right)\sin(\omega t + l\theta - \beta z), \tag{2.32d}$$

$$H_\theta = \frac{i\beta}{q^2}\left(\frac{il}{r}DK_l(qr) + \frac{\omega\epsilon_2}{\beta}CqK_l'(qr)\right)\cos(\omega t + l\theta - \beta z), \tag{2.32e}$$

$$H_z = DK_l(qr)\cos(\omega t + l\theta - \beta z), \tag{2.32f}$$

where the convention is used that the tangential components of the electric field are real and the longitudinal components are imaginary. This requires A and C to be imaginary, and B and D to be real. A can be chosen to be imaginary, and the other amplitudes are calculated from A using the boundary conditions.

The propagation constants are found by applying the continuity conditions for the fields at the core-cladding interface. In general, the modes are broken down into two classes, HE and EH. These modes are neither TE nor TM because all of their field components are nonzero. Thus, they are often referred to as hybrid modes. The characteristic equations for these modes are:

EH modes:

$$\frac{J_{l+1}(hR_f)}{hR_fJ_l(hR_f)} = \frac{n_1^2 + n_2^2}{2n_1^2}\frac{K_l'(qR_f)}{qR_fK_l(qR_f)} + \left(\frac{l}{(hR_f)^2} - R\right), \tag{2.33}$$

and HE modes:

$$\frac{J_{l-1}(hR_f)}{hR_fJ_l(hR_f)} = -\frac{n_1^2 + n_2^2}{2n_1^2}\frac{K_l'(qR_f)}{qR_fK_l(qR_f)} + \left(\frac{l}{(hR_f)^2} - R\right), \tag{2.34}$$

where

$$R = \sqrt{\left(\frac{n_1^2 - n_2^2}{2n_1^2}\right)^2\left(\frac{K_l'(qR_f)}{qR_fK_l(qR_f)}\right)^2 + \frac{l^2}{n_1^2}\left(\frac{\beta}{k_o}\right)^2\left(\frac{1}{h^2R_f^2} + \frac{1}{q^2R_f^2}\right)^2}. \tag{2.35}$$

Because h and q are related to β, the propagation constants are found by finding the roots. When $l = 0$, the EH and HE modes are reduced to TM and TE modes, respectively, and their propagation constants are found from

TM modes,

$$\frac{J_1(hR_f)}{hR_f J_0(hR_f)} = -\frac{n_2^2}{n_1^2}\frac{K_1(qR_f)}{qR_f K_0(qR_f)}, \tag{2.36}$$

and TE modes

$$\frac{J_1(hR_f)}{hR_f J_0(hR_f)} = -\frac{K_1(qR_f)}{qR_f K_0(qR_f)}. \tag{2.37}$$

The number of roots to these characteristic equations (2.33–2.37) depends on how large the fiber is compared to the wavelength. As the size of the fiber becomes small compared to that of the wavelength, fewer modes are able to satisfy the boundary conditions. Another way of saying this is that there are fewer ways that the light can be arranged to fit in the fiber. The HE_{11} mode, which is characterized by a single maximum, is the lowest-order mode supported by a fiber. No matter how small a fiber is, the HE_{11} mode is supported. This does not mean that the guiding of the field is always strong. For very small fibers, a large fraction of the mode is evanescent. Table 2.1 shows the arrangement of the propagation constants for all the modes of a fiber of radius 1.8 μm and indices of refraction of $n_1 = 1.44$ and $n_2 = 1.00$. These conditions are appropriate for a tapered fiber. The table shows the modes for guided light of 1550 nm wavelength.

2.4.1 Linearly Polarized Modes

For ordinary fibers, the indices of refraction of the core and cladding are very similar. Under this condition, the modes can be approximated to be linearly polarized. This means that the directions of the transverse components of the fields do not change with position. The fields of these modes are found to be

TABLE 2.1. Fiber Mode Propagation Constants ($R_f = 1.8\,\mu$m, $n_1 = 1.44$, $n_2 = 1.00$, $\lambda = 1550\,$nm)

TE/TM	HE_{1m}	HE_{2m}	EH_{1m}	HE_{3m}	EH_{2m}	HE_{4m}	EH_{3m}	HE_{5m}	$\beta(10^6\,\mathrm{m}^{-1})$
	HE_{11}								5.70852
TE_{01}									5.52879
		HE_{21}							5.50387
TM_{01}									5.48988
			EH_{11}						5.25528
				HE_{31}					5.22249
	HE_{12}								5.12826
					EH_{21}				4.92304
						HE_{41}			4.85606
TE_{02}									4.75933
		HE_{22}							4.66893
TM_{02}									4.65044
							EH_{31}		4.52000
								HE_{51}	4.38898
			EH_{12}						4.23848
				HE_{32}					4.14214
	HE_{13}								4.13354

for the core ($r < R_f$),

$$E_x = AJ_l(hr)e^{il\theta}\exp[i(\omega t - \beta z)], \tag{2.38a}$$

$$E_y = 0, \tag{2.38b}$$

$$E_z = i\frac{h}{\beta}\frac{A}{2}\left[J_{l+1}(hr)e^{i(l+1)\theta} - J_{l-1}(hr)e^{i(l-1)\theta}\right]\exp[i(\omega t - \beta z)], \tag{2.38c}$$

$$H_x \simeq 0, \tag{2.38d}$$

$$H_y = \frac{\beta}{\omega\mu}AJ_l(hr)e^{il\theta}\exp[i(\omega t - \beta z)], \tag{2.38e}$$

$$H_z = \frac{h}{\omega\mu}\frac{A}{2}\left[J_{l+1}(hr)e^{i(l+1)\theta} + J_{l-1}(hr)e^{i(l-1)\theta}\right]\exp[i(\omega t - \beta z)], \tag{2.38f}$$

and for the cladding ($r > R_f$),

$$E_x = BK_l(qr)e^{il\theta}\exp[i(\omega t - \beta z)], \tag{2.39a}$$

$$E_y = 0, \tag{2.39b}$$

$$E_z = i\frac{q}{\beta}\frac{B}{2}\left[K_{l+1}(qr)e^{i(l+1)\theta} + K_{l-1}(qr)e^{i(l-1)\theta}\right]\exp[i(\omega t - \beta z)], \tag{2.39c}$$

$$H_x \simeq 0, \tag{2.39d}$$

$$H_y = \frac{\beta}{\omega\mu}BK_l(qr)e^{il\theta}\exp[i(\omega t - \beta z)], \tag{2.39e}$$

$$H_z = \frac{q}{\omega\mu}\frac{B}{2}\left[K_{l+1}(qr)e^{i(l+1)\theta} - K_{l-1}(qr)e^{i(l-1)\theta}\right]\exp[i(\omega t - \beta z)]. \tag{2.39f}$$

The characteristic equation used to calculate the propagation constants is

$$h\frac{J_{l+1}(hR_f)}{J_l(hR_f)} = q\frac{K_{l+1}(qR_f)}{K_l(qR_f)}. \tag{2.40}$$

The lowest-order linearly polarized (LP_{lm}) mode is the LP_{01} mode. The next higher-order mode in this family is the LP_{02} mode. If the difference between the core and cladding indices cannot be considered negligible, the LP_{01} mode must be expressed by the HE_{11} mode and the LP_{02} mode by the HE_{12} mode. As is discussed in later chapters, the HE_{11} and HE_{12} modes are important to understand. The following section describes these and other modes that are considered in this study.

2.4.2 Lower-Order Modes

There are seven fiber modes that are considered in this study. The first is the HE_{11} mode. As was previously mentioned, this is the fundamental mode and is characterized by a single maximum. This can be seen in Fig. 2.4. The 3-D plot is of the amplitude of the transverse component of the electric field as a function of transverse coordinates. The cross-section of the fiber is in the xy-plane. The abrupt color change from blue to red indicates the surface of the fiber. Notice that for $x = 0$ the electric field is continuous at the surface and for $y = 0$ the electric field is discontinuous at the surface. This is because of the orientation of the field. In the orientation shown here, the electric field is parallel to the surface at $x = 0$. The boundary conditions require that the fields be continuous when the field is parallel to the surface. The field is perpendicular to the surface at $y = 0$. The boundary conditions require that the fields undergo a step change when the field is perpendicular to a change in permittivity. This is given by the relation

$$E_1^{\perp} n_1^2 = E_2^{\perp} n_2^2. \tag{2.41}$$

This means that the amplitude of the field is $(1.44)^2$ times larger on the outside of the surface than on the inside. Another effect of the transverse component of the field being perpendicular to the surface is that the longitudinal component becomes nonzero. The longitudinal component of the field is shown in Fig. 2.5. Again, the color change indicates the surface of the fiber. In this figure, the longitudinal component of the field is zero at the surface where the transverse component in Fig. 2.4 is continuous, and the longitudinal component is nonzero at the surface where the transverse component in Fig. 2.4 is discontinuous. The polarization of the transverse component of the electric field is shown in Fig. 2.6, where the arrows point in the direction of the electric field and the lengths of the arrows indicate the magnitude of the field. This plot shows that the mode is nearly linearly polarized. For the size fiber shown here, only small distortions are seen. For smaller fibers, the distortions become more pronounced.

The next mode is the HE_{12} mode. This is the next higher-order mode in the same family as the HE_{11} mode and is characterized by a maximum at the center of the fiber surrounded by a minimum ring before reaching the surface. Whereas the HE_{11} mode would

be seen as a single bright spot when viewed from a perspective perpendicular to the fiber's cross-section, the HE_{12} mode would appear as a bright spot surrounded by a ring. The transverse and longitudinal components of its fields are shown in Fig. 2.7 and Fig. 2.8, respectively. The polarization of the transverse component of the field is shown in Fig. 2.9. In this figure, near the surface of the fiber, the field is close to being linearly polarized but not as close as in the case of the HE_{11} mode.

In addition to the HE_{11} and HE_{12} modes, modes that have propagation constants between the HE_{11} and HE_{12} modes are also considered in this study. Table 2.1 indicates the modes of interest are the TE_{01}, HE_{21}, TM_{01}, EH_{11}, and HE_{31} modes. The vector plots of the transverse components of their fields are shown in Figs. 2.10–2.14. There are several points worth noting about the respective modes in these figures. From Table 2.1, it is seen that the propagation constants of the TE_{01}, HE_{21}, and TM_{01} modes are very close. For fibers that satisfy the LP-approximation, the superposition of these modes forms the LP_{11} mode. The plots of the HE_{l1} modes demonstrate the effect of changing the mode index l. The field lines are divided into sections of π/l for $l > 1$. The EH_{11} mode has two dark spots corresponding to the two locations around which the fields circulate. The TM_{01} mode is the only mode that has a discontinuous transverse field at all points on the surface. The TE_{01} mode is unique among these modes because its transverse field is continuous at every point on the surface of the fiber. This means that all of its energy is in the transverse component of the field. An effect of this is seen in Chapter 4.

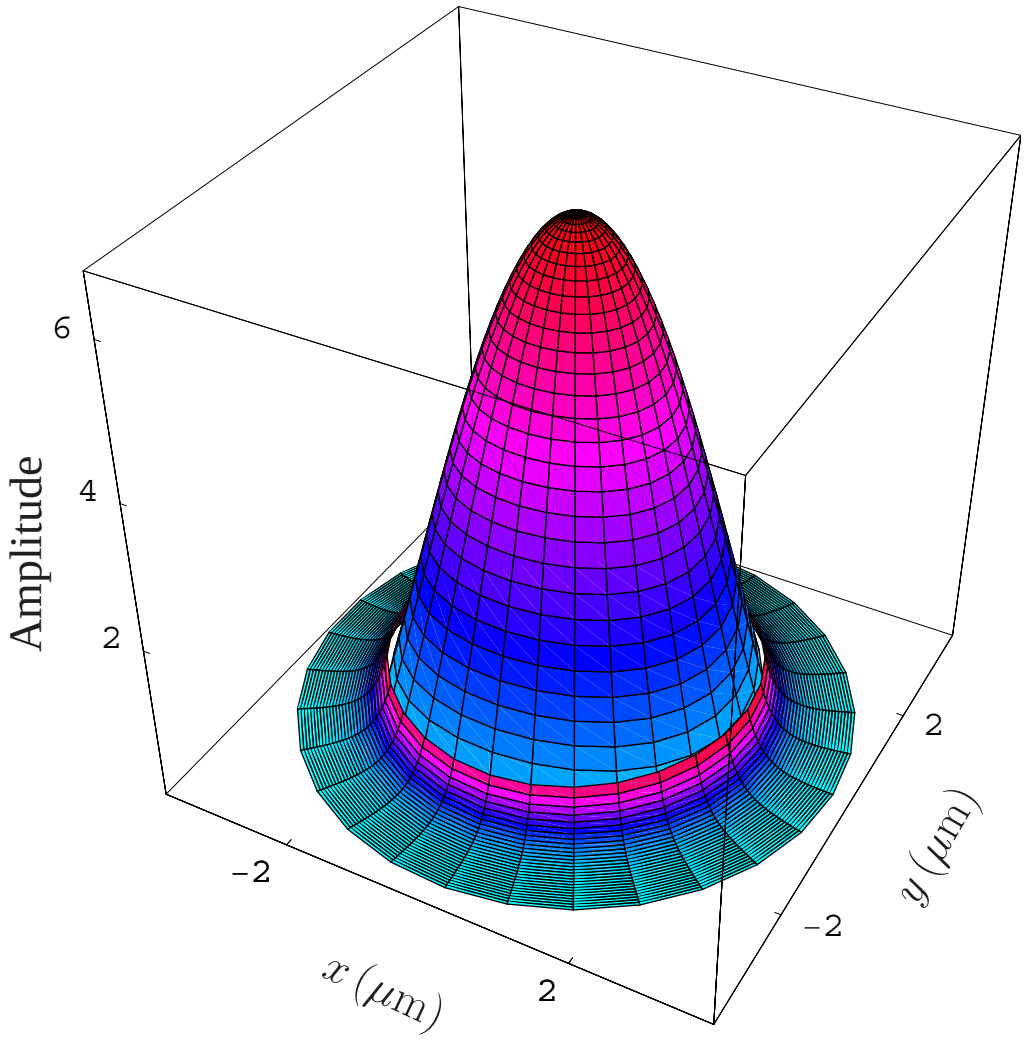

Figure 2.4. Fiber HE_{11} Mode Transverse Field Amplitude as a Function of Transverse Coordinates ($R_f = 2.47\,\mu\mathrm{m}$, $\lambda = 1550\,\mathrm{nm}$). The surface of the fiber is indicated by the color change.

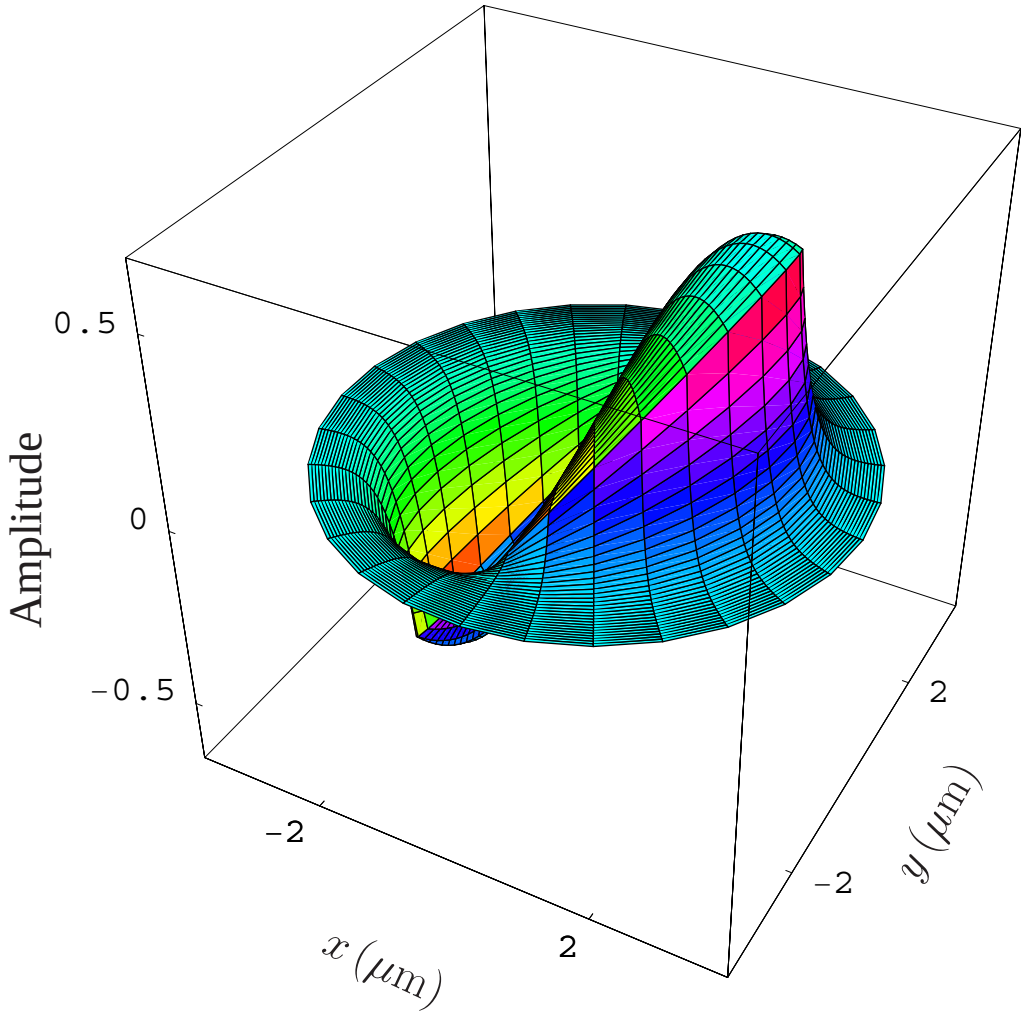

Figure 2.5. Fiber HE_{11} Mode Longitudinal Field Amplitude as a Function of Transverse Coordinates ($R_f = 2.47\,\mu\mathrm{m}$, $\lambda = 1550\,\mathrm{nm}$). The surface of the fiber is indicated by the color change.

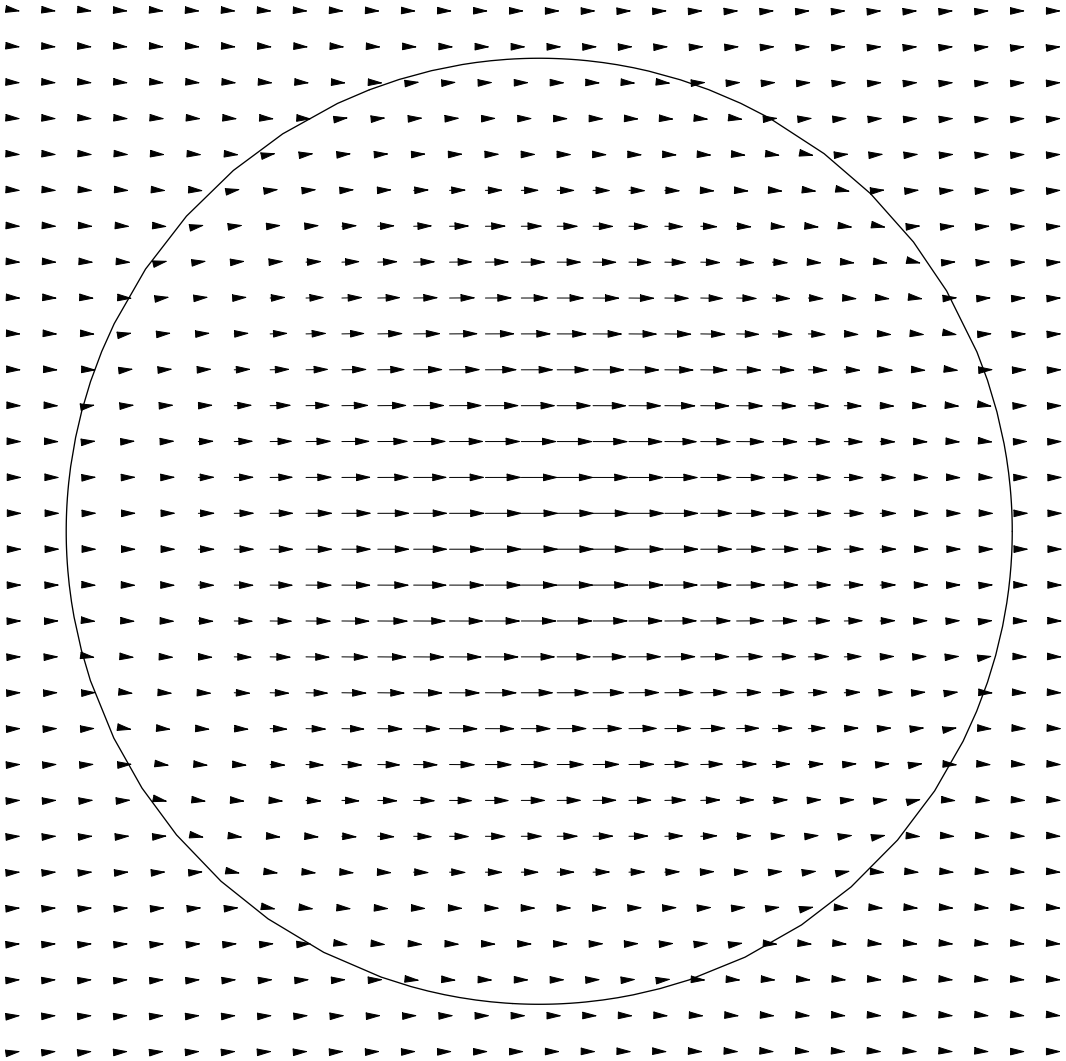

Figure 2.6. Fiber Cross-Section with HE_{11} Mode Tranverse Field Polarization ($R_f = 2.47\,\mu\mathrm{m}$, $\lambda = 1550\,\mathrm{nm}$). The surface of the fiber is indicated by the circle.

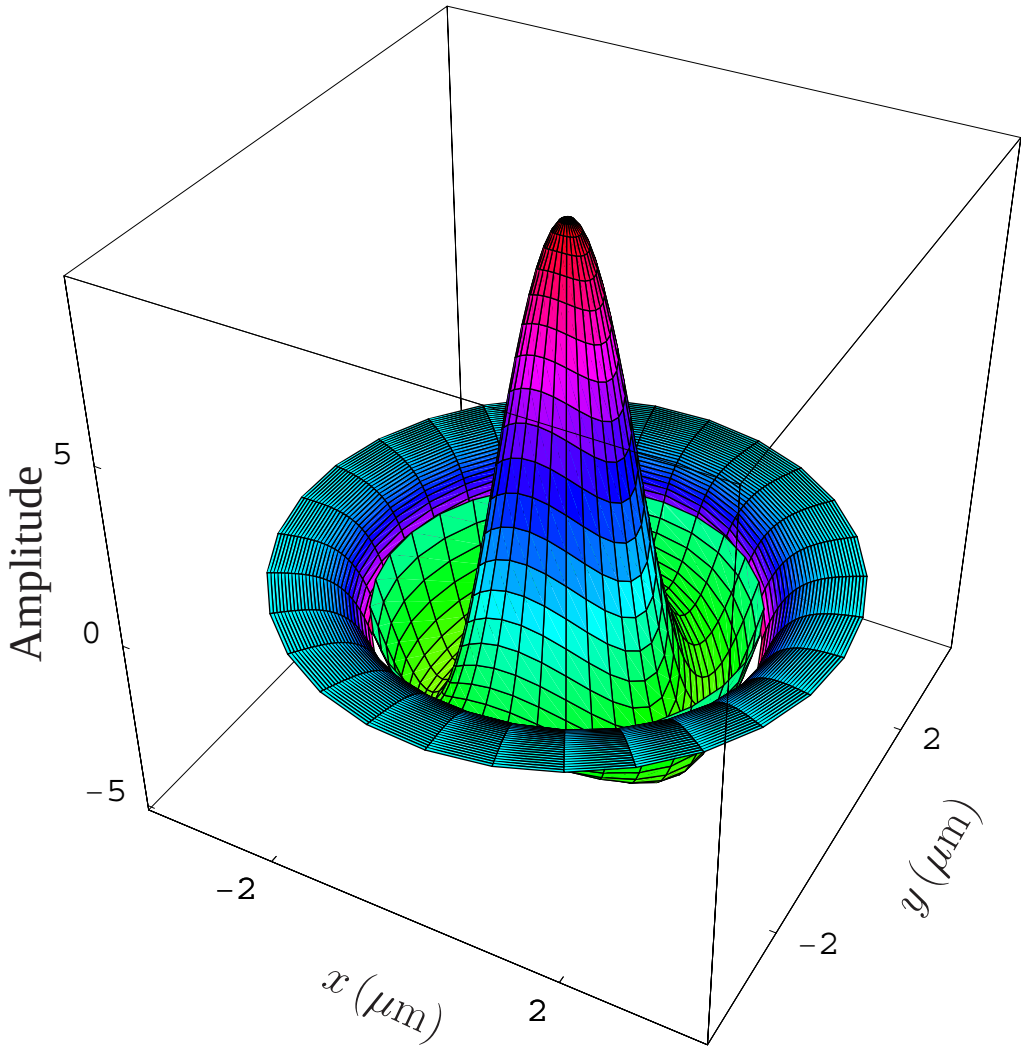

Figure 2.7. Fiber HE_{12} Mode Transverse Field Amplitude as a Function of Transverse Coordinates ($R_f = 2.47\,\mu\mathrm{m}$, $\lambda = 1550\,\mathrm{nm}$). The surface of the fiber is indicated by the color change.

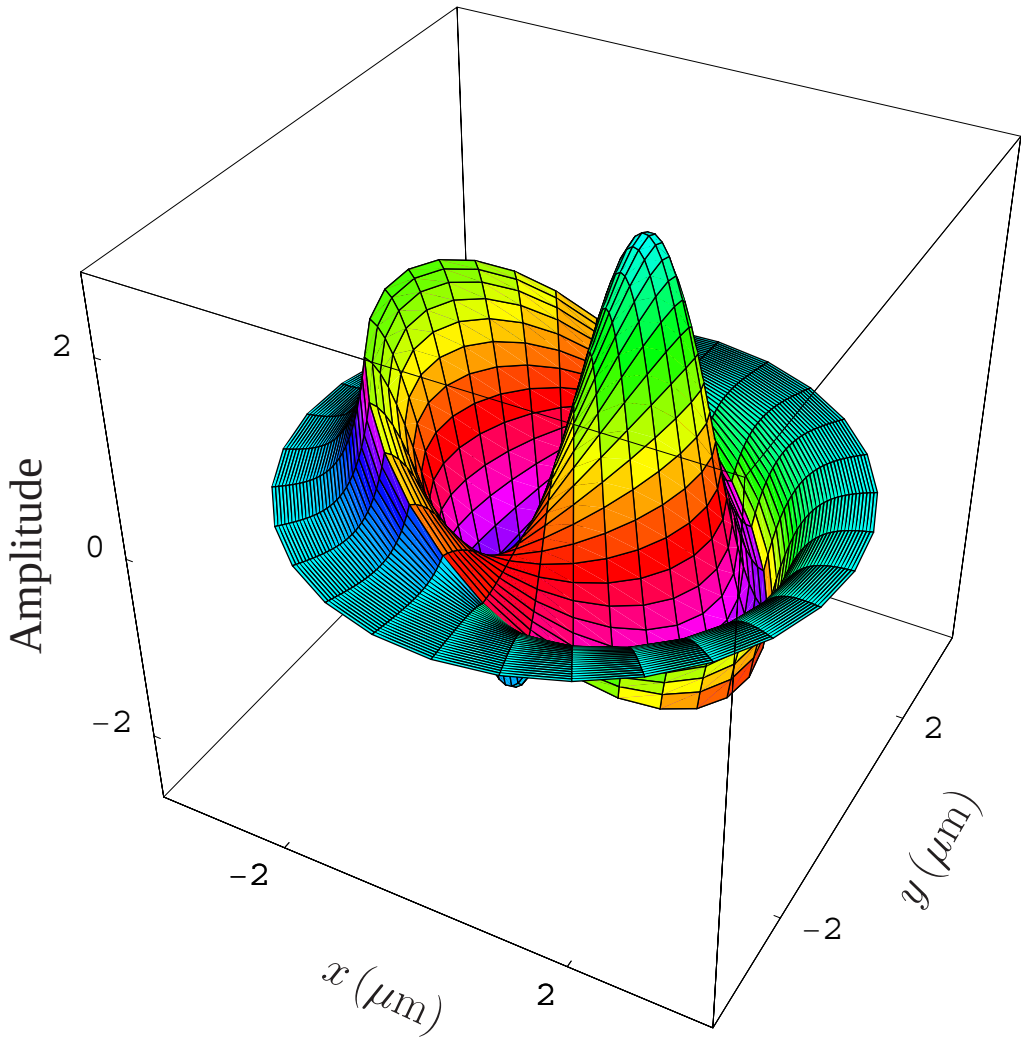

Figure 2.8. Fiber HE_{12} Mode Longitudinal Field Amplitude as a Function of Transverse Coordinates ($R_f = 2.47\,\mu\mathrm{m}$, $\lambda = 1550\,\mathrm{nm}$). The surface of the fiber is indicated by the color change.

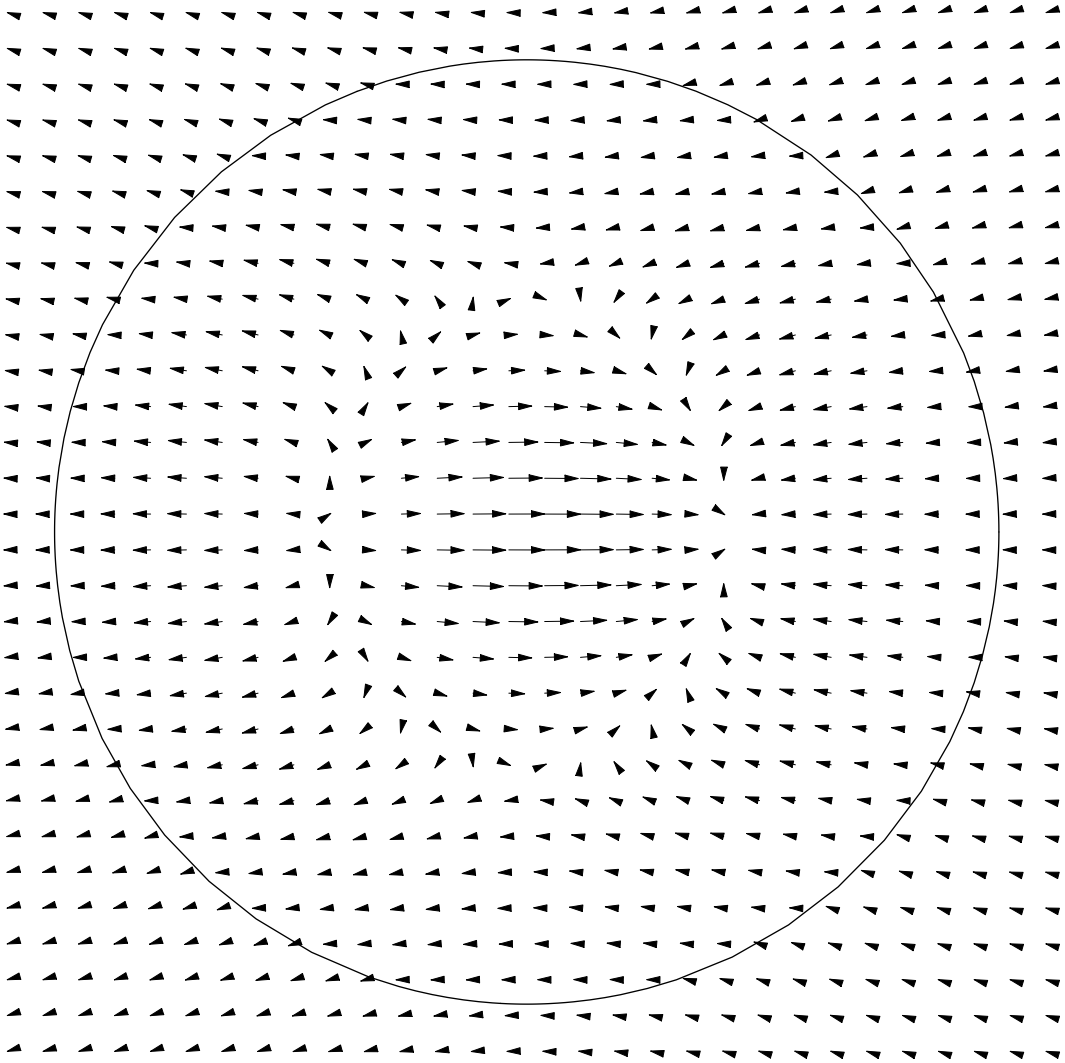

Figure 2.9. Fiber Cross-Section with HE_{12} Mode Transverse Field Polarization ($R_f = 2.47\,\mu\mathrm{m}$, $\lambda = 1550\,\mathrm{nm}$). The surface of the fiber is indicated by the circle.

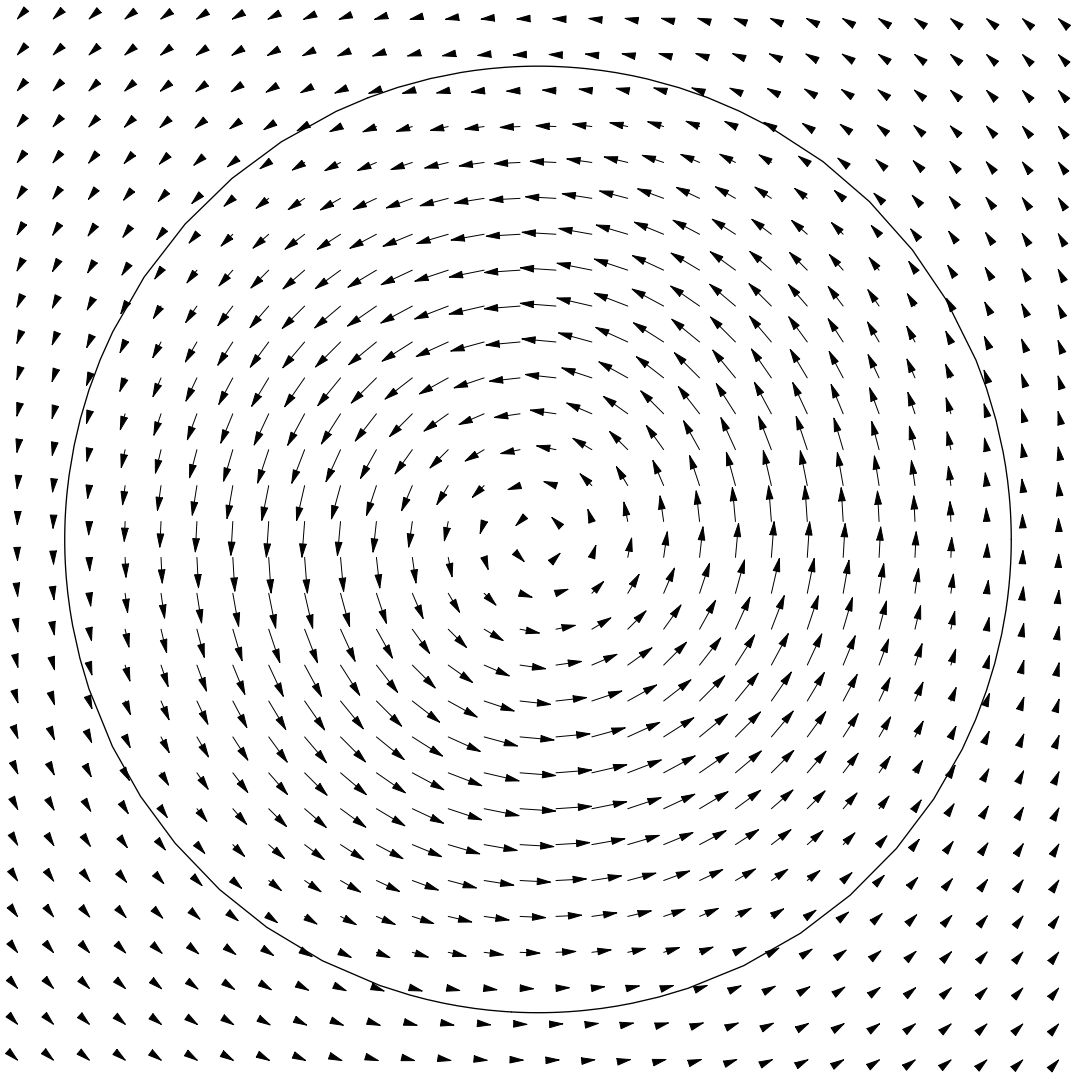

Figure 2.10. Fiber Cross-Section with TE_{01} Mode Transverse Field Polarization ($R_f = 2.47\,\mu\mathrm{m}$, $\lambda = 1550\,\mathrm{nm}$). The surface of the fiber is indicated by the circle.

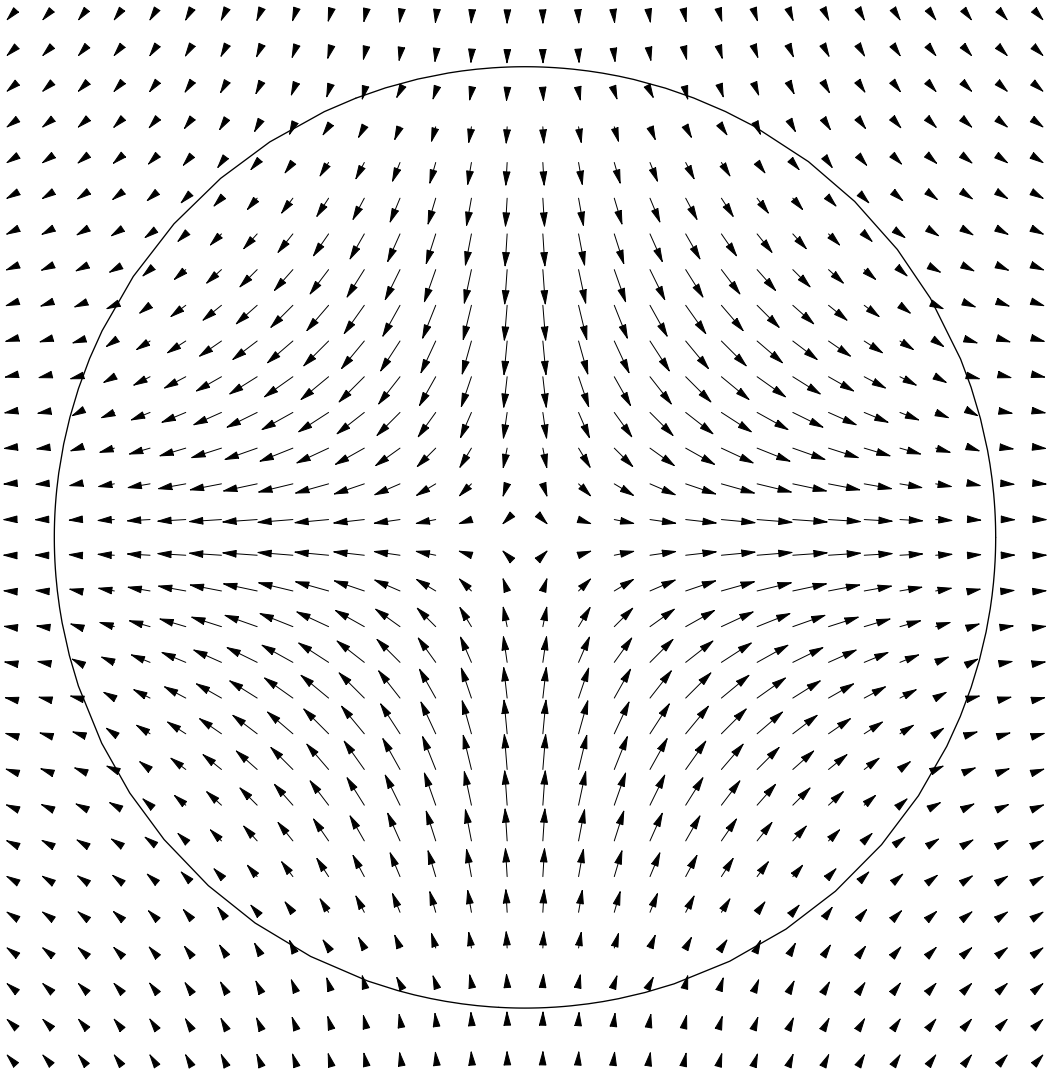

Figure 2.11. Fiber Cross-Section with HE_{21} Mode Transverse Field Polarization ($R_f = 2.47\,\mu\mathrm{m}$, $\lambda = 1550\,\mathrm{nm}$). The surface of the fiber is indicated by the circle.

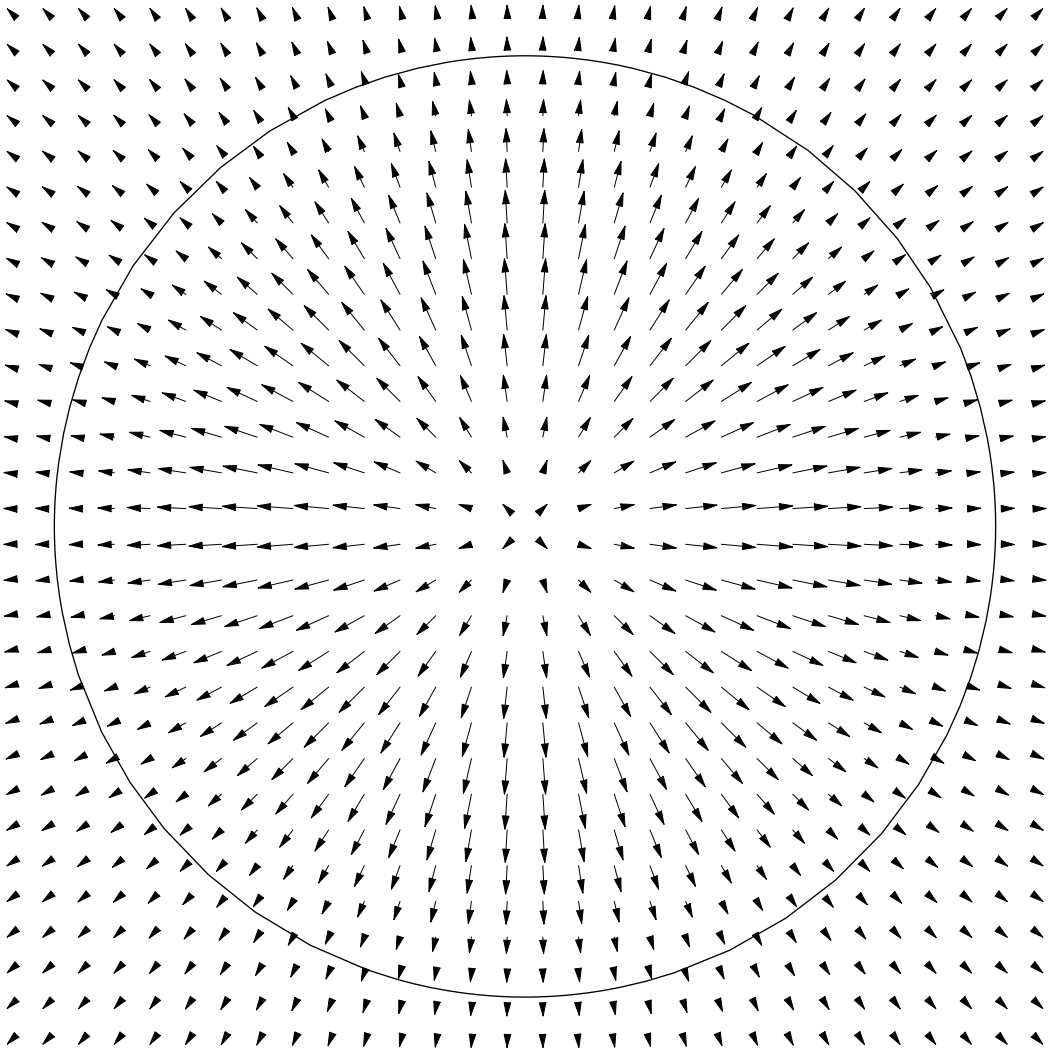

Figure 2.12. Fiber Cross-Section with TM_{01} Mode Transverse Field Polarization ($R_f = 2.47\,\mu\mathrm{m}$, $\lambda = 1550\,\mathrm{nm}$). The surface of the fiber is indicated by the circle.

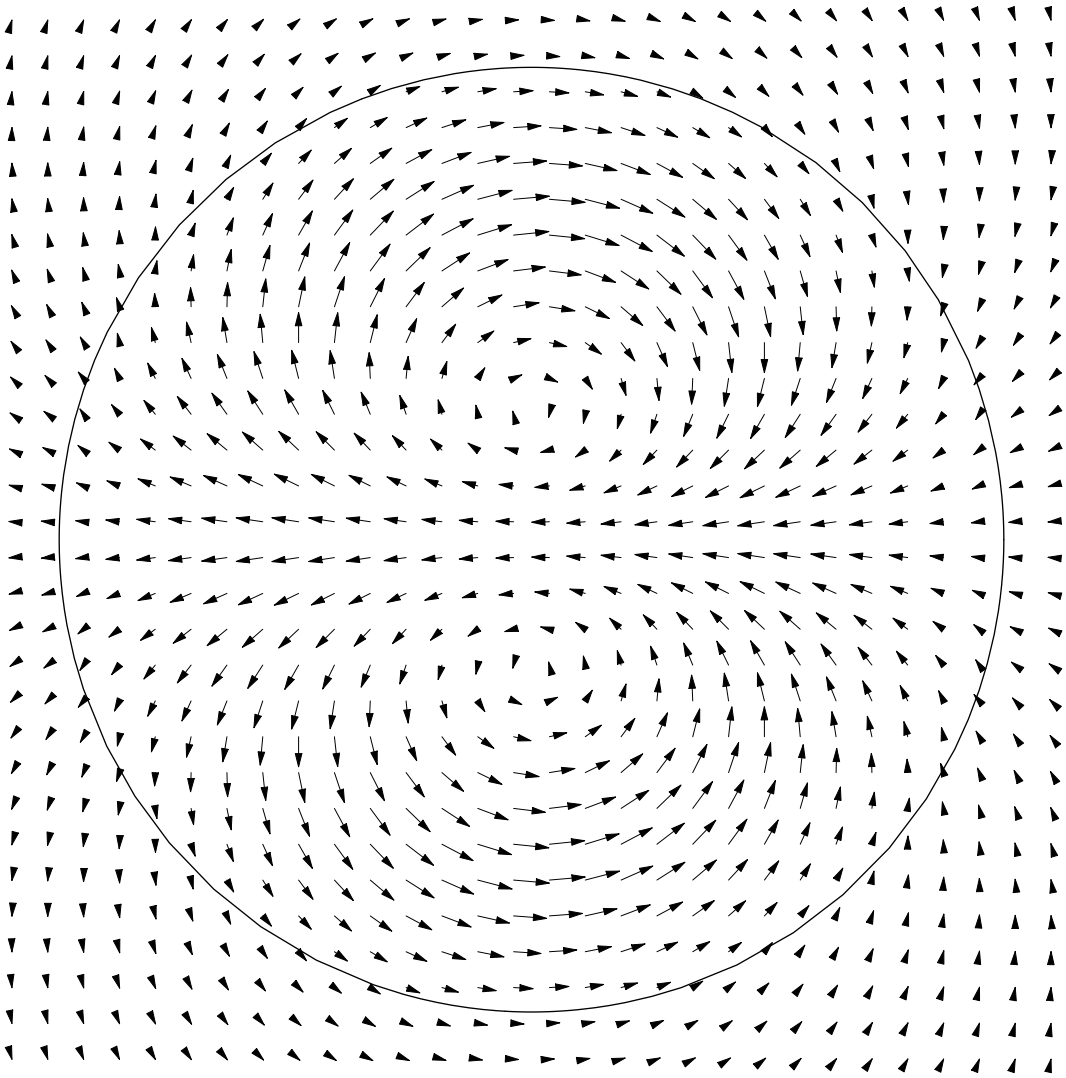

Figure 2.13. Fiber Cross-Section with EH_{11} Mode Transverse Field Polarization ($R_f = 2.47\,\mu\mathrm{m}$, $\lambda = 1550\,\mathrm{nm}$). The surface of the fiber is indicated by the circle.

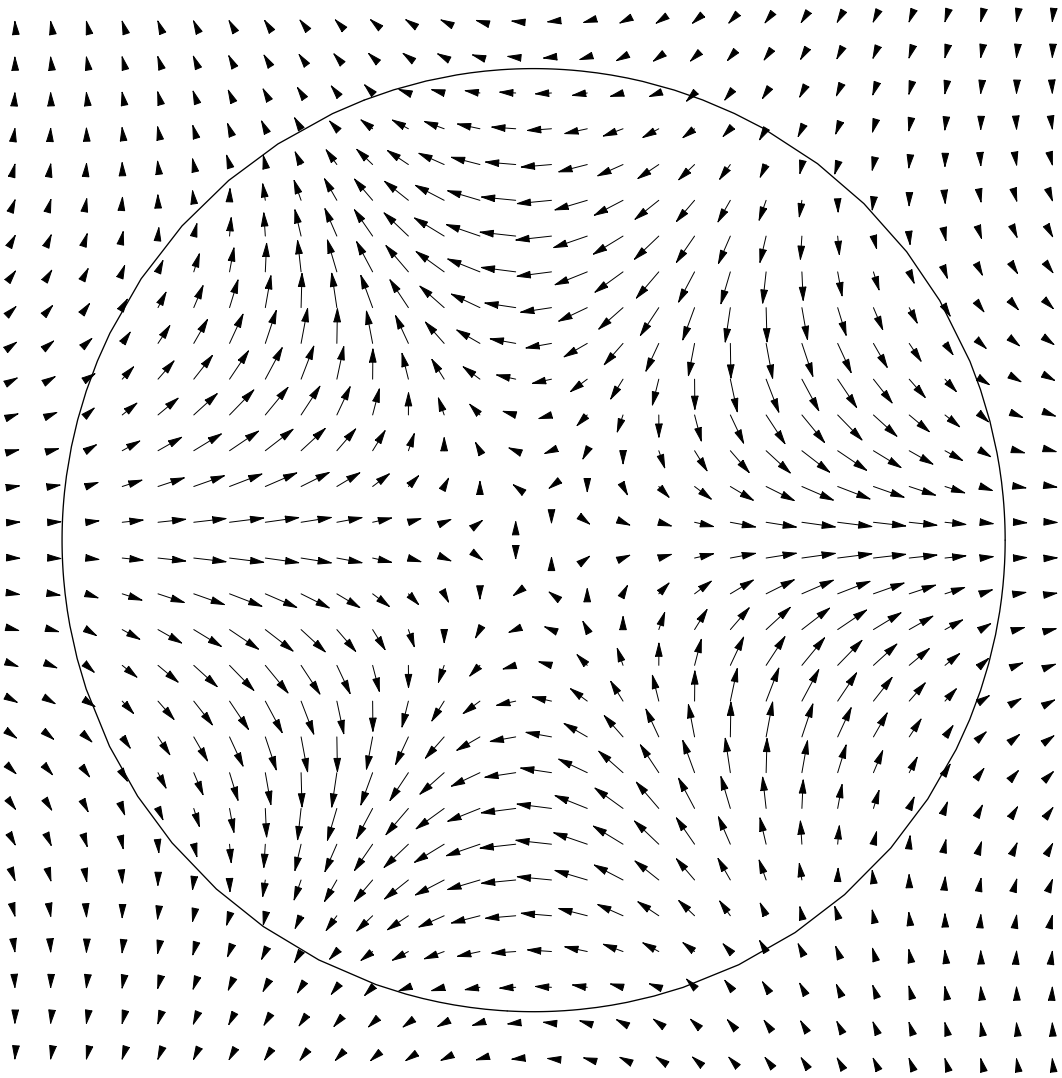

Figure 2.14. Fiber Cross-Section with HE_{31} Mode Transverse Field Polarization ($R_f = 2.47\,\mu\mathrm{m}$, $\lambda = 1550\,\mathrm{nm}$). The surface of the fiber is indicated by the circle.

CHAPTER 3

MODE COUPLING

There are conditions in which electromagnetic modes may couple. One is when a single isolated waveguide contains a perturbation, such as an imperfection in the waveguide construction. The presence of the perturbation prevents any single mode of the unperturbed waveguide from being a solution of the perturbed waveguide by itself. The solution is a superposition of the unperturbed modes. The tapered fiber is another example of this. The section of the fiber that has a varying radius is a perturbation of the cylindrical fiber. The superposition of the cylindrical fiber modes is a solution of the non-cylindrical fiber. Another situation in which modes couple is when separate waveguides are in close enough proximity so that the evanescent portions of their modes penetrate the opposite waveguide. A common example of this is cross-talk between fibers in a fiber-optic cable. In the system studied here, it is the means by which light is coupled into the microsphere from the fiber and *vice versa*. In both types of coupling described here, the perturbations result in energy being transfered between unperturbed modes. This chapter describes coupled-mode theory and applies it to both fiber-microsphere coupling and to coupling between modes in the tapered fiber. This chapter also shows that the two factors that determine the amount of coupling are the amount of spatial overlap of the modes and the phase-matching between them. For cases where the coupling cannot be considered a small perturbation, other means of analysis are required. Such methods are not presented here, but an example is the vector-modal solution method.[53]

3.1 Coupled-Mode Theory

Coupled-mode theory quantifies the coupling between modes by assuming the interactions between the modes only result in small perturbations. By this it is meant that

although energy is transfered between the two modes, the shapes of the modes are not being significantly distorted by the interaction. The basis of coupled-mode theory is the application of the reciprocity relation to the system of interest.[54–56] The reciprocity relation for two modes is derived in Appendix B. In integral form, over an infinitesimal range Δz in the direction of propagation, it is

$$\begin{aligned}\frac{\partial}{\partial z}\iint \left(\mathbf{E}_1 \times \mathbf{H}_2^* + \mathbf{E}_2^* \times \mathbf{H}_1\right) \cdot \hat{z}\,\mathrm{d}x\,\mathrm{d}y \\ = i\omega \iint (\epsilon_1(x,y) - \epsilon_2(x,y))\mathbf{E}_1 \cdot \mathbf{E}_2^*\,\mathrm{d}x\,\mathrm{d}y,\end{aligned} \tag{3.1}$$

where $\mathbf{E}_1$ and $\mathbf{H}_1$ are the electric and magnetic fields of one mode, and $\mathbf{E}_2$ and $\mathbf{H}_2$ are the fields of the second mode, ω is the angular frequency of the light, and $\epsilon_1(x,y)$ and $\epsilon_2(x,y)$ are the permittivity profiles of the two modes. Physically, the reciprocity relation means that the net power flow between two lossless waveguides is symmetrical.

For the case of two parallel waveguides, a and b, each supporting a single mode, the perturbation to the mode of waveguide a can be determined. The permittivity profiles are given as

$$\epsilon_1(x,y) = \epsilon(x,y), \tag{3.2a}$$

$$\epsilon_2(x,y) = \epsilon_a(x,y), \tag{3.2b}$$

where the permittivity profiles $\epsilon_a(x,y)$ and $\epsilon(x,y)$ are for waveguide a and the composite system, respectively. The transverse fields of the coupled system are taken to be a linear combination of the transverse fields of the individual waveguides as follows:

$$\mathbf{E}_1^t = a(z)\,\mathbf{E}_a^t(x,y) + b(z)\,\mathbf{E}_b^t(x,y), \tag{3.3a}$$

$$\mathbf{H}_1^t = a(z)\,\mathbf{H}_a^t(x,y) + b(z)\,\mathbf{H}_b^t(x,y), \tag{3.3b}$$

where $a(z)$ and $b(z)$ are the amplitudes of the modes in waveguides a and b as functions the longitudinal coordinate. The longitudinal fields are similarly expressed as a linear combination of the longitudinal components of the fields

$$\mathbf{E}_1^z = a(z)\,\frac{\epsilon_a}{\epsilon}\,\mathbf{E}_a^z(x,y) + b(z)\,\frac{\epsilon_b}{\epsilon}\,\mathbf{E}_b^z(x,y), \tag{3.4a}$$

$$\mathbf{H}_1^z = a(z)\,\mathbf{H}_a^z(x,y) + b(z)\,\mathbf{H}_b^z(x,y). \tag{3.4b}$$

The fields of the perturbed waveguide are expressed in the usual amplitude and phase relation as follows:

$$\mathbf{E}_2 = \mathbf{E}_a(x,y)e^{-i\beta_a z}, \tag{3.5a}$$

$$\mathbf{H}_2 = \mathbf{H}_a(x,y)e^{-i\beta_a z}. \tag{3.5b}$$

The fields and permittivity profiles are substituted into Eq. (3.1). The previous procedure is repeated with waveguide b being perturbed. In this case, the permittivity profiles are

$$\epsilon_1(x,y) = \epsilon(x,y), \tag{3.6a}$$

$$\epsilon_2(x,y) = \epsilon_b(x,y). \tag{3.6b}$$

Here, $\epsilon_b(x,y)$ is the permittivity profile of waveguide b. The transverse and longitudinal fields of the coupled system are the same as those with waveguide a being perturbed (see Eqs. (3.3) and (3.4)). The fields of the perturbed waveguide are given as

$$\mathbf{E}_2 = \mathbf{E}_b(x,y)e^{-i\beta_b z}, \tag{3.7a}$$

$$\mathbf{H}_2 = \mathbf{H}_b(x,y)e^{-i\beta_b z}. \tag{3.7b}$$

The result of substituting the fields into the reciprocity relation, first with waveguide a being perturbed, and second with waveguide b being perturbed, is that, at any z,

$$\kappa_{ba}(z) - \kappa_{ab}(z) = \frac{1}{2}(C_{ab}(z) + C_{ba}(z))(\beta_b - \beta_a), \tag{3.8}$$

where

$$\kappa_{ab}(z) = \frac{\omega}{4}\iint_{-\infty}^{\infty}(\epsilon(x,y) - \epsilon_b(x,y))\left(\mathbf{E}_b^t \cdot \mathbf{E}_a^{t\,*} + \frac{\epsilon_a}{\epsilon}E_b^z E_a^{z*}\right)\mathrm{d}x\,\mathrm{d}y, \tag{3.9a}$$

$$C_{ab}(z) = \frac{1}{2}\iint_{-\infty}^{\infty}\left(\mathbf{E}_2^t \times \mathbf{H}_1^{t\,*}\right)\cdot\hat{z}\,\mathrm{d}x\,\mathrm{d}y. \tag{3.9b}$$

κ_{ab} and C_{ab} are known as coupling coefficients, as they quantify the amount of coupling between two normalized modes. Coefficients κ_{ba} and C_{ba} are calculated using Eqs. (3.9a) and (3.9b) by swapping the subscripts. Coefficient κ is of primary interest here because it determines the probability that a photon tunnels from one mode to another. Coefficient C represents the energy associated with the overlap of the two modes. An important fact is that $\kappa_{ab} \neq \kappa_{ba}$ if $\beta_a \neq \beta_b$. This is because modes with higher propagation constants have smaller evanescent fractions than modes with lower propagation constants.

3.1.1 Coupled-Mode Equations

Without coupling, the amplitudes of the fields of two modes, in waveguides a and b, can be described by the differential equations

$$\frac{\mathrm{d}E_a(z)}{\mathrm{d}z} = -i\beta_a E_a(z), \tag{3.10a}$$

$$\frac{\mathrm{d}E_b(z)}{\mathrm{d}z} = -i\beta_b E_b(z). \tag{3.10b}$$

The solutions to these equations are

$$E_a(z) = E_a(0)e^{-i(\beta_a z+\phi_a)}, \tag{3.11a}$$

$$E_b(z) = E_b(0)e^{-i(\beta_b z+\phi_b)}. \tag{3.11b}$$

With coupling, the modal amplitudes are

$$\frac{\mathrm{d}E_a(z)}{\mathrm{d}z} = -i\beta_a E_a(z) + i\kappa_{ab}(z)E_b(z), \tag{3.12a}$$

$$\frac{\mathrm{d}E_b(z)}{\mathrm{d}z} = -i\beta_b E_b(z) + i\kappa_{ba}(z)E_a(z). \tag{3.12b}$$

These equations are known as the coupled-mode equations for two parallel waveguides.

3.1.2 Energy Conservation

A common misconception in mode-coupling theory is that for energy to be conserved the coupling coefficients must be equal, or $\kappa_{ab} = \kappa_{ba}$. However, according to coupled-mode theory, these coefficients are not equal. It is roughly explained that, for unequal coupling coefficients, energy is radiated during coupling to unbound (or radiation) modes. This is not the case. The source of the confusion lies in the method used to calculate the energy. In general, the Poynting vector **S** is used to calculate the energy flow of an electromagnetic wave,

$$\mathbf{S} = \frac{1}{2}\,\mathbf{E} \times \mathbf{H}^*. \tag{3.13}$$

For two modes that are not coupled, the total energy flow becomes

$$\begin{aligned}\mathbf{S}_{\text{tot}} &= \mathbf{S}_1 + \mathbf{S}_2 \\ &= \frac{1}{2}(\mathbf{E}_1 \times \mathbf{H}_1^* + \mathbf{E}_2 \times \mathbf{H}_2^*),\end{aligned} \tag{3.14}$$

where $\mathbf{S}_1$ and $\mathbf{S}_2$ represent the energy flow of each mode. The power as a function of z can be written as

$$P(z) = |a(z)|^2 + |b(z)|^2, \tag{3.15}$$

where $a(z)$ and $b(z)$ are the same as in Eqs. (3.3) and (3.4). When the power is calculated as such, the two coupling coefficients must be equal. This is not correct when calculating power in a coupled system. For the coupled system the Poynting vector is

$$\begin{aligned}\mathbf{S}_{\text{tot}} &= \frac{1}{2}\,\mathbf{E}_{\text{tot}} \times \mathbf{H}^*_{\text{tot}} \\ &= \frac{1}{2}\,(\mathbf{E}_1 + \mathbf{E}_2) \times (\mathbf{H}^*_1 + \mathbf{H}^*_2) \\ &= \frac{1}{2}[(\mathbf{E}_1 \times \mathbf{H}^*_1) + (\mathbf{E}_1 \times \mathbf{H}^*_2) + (\mathbf{E}_2 \times \mathbf{H}^*_1) + (\mathbf{E}_2 \times \mathbf{H}^*_2)].\end{aligned} \tag{3.16}$$

In this case, the power as a function of z is written as

$$P(z) = |a(z)|^2 + |b(z)|^2 + (C_{ab}(z) + C_{ba}(z))\Re[a(z)b^*(z)], \tag{3.17}$$

where, again, $a(z)$ and $b(z)$ are the same as in Eqs. (3.3) and (3.4). Only the real part of $a(z)b^*(z)$ represents energy flow. The imaginary part represents stored energy. Radiation losses are ignored here because they are negligible in this study. The condition that must be satisfied for the energy to be constant is

$$\kappa_{ba}(z) - \kappa_{ab}(z) = \frac{1}{2}(C_{ab}(z) + C_{ba}(z))(\beta_b - \beta_a), \tag{3.18}$$

which is already satisfied with coupled-mode theory. A quantum mechanical analog is useful here. A diatomic molecule that has a shared electron between the two atoms exhibits the same behavior as in coupled-mode theory. The atom that attracts the electron more strongly has the electron more often than the atom that attracts the electron less strongly. This is intuitively correct and is a result of the overlap integrals of the wavefunctions being unequal, just as they are in the case of two non-identical waveguides.

3.2 Fiber-Microsphere System

Calculations for the fiber-microsphere system involve the calculation of κ_{sf}, the coupling into the microsphere mode from the fiber mode, and κ_{fs}, the coupling into the fiber

mode from the microsphere mode by use of the overlap integrals. Figure 3.1 shows the microsphere and fiber modes when the fiber is placed in contact with the microsphere. The utility of the coupling coefficients is great when taking into account a weak coupling condition.

3.2.1 Weak Coupling

Assuming that one microsphere mode is interacting with one fiber mode, the coupled-mode equations for the fiber-microsphere system are given by

$$\frac{\mathrm{d}E_s(z)}{\mathrm{d}z} = -i\beta_s E_s(z) + i\kappa_{sf}(z)E_f(z), \tag{3.19a}$$

$$\frac{\mathrm{d}E_f(z)}{\mathrm{d}z} = -i\beta_f E_f(z) + i\kappa_{fs}(z)E_s(z), \tag{3.19b}$$

where the subscripts "s" and "f" refer to the microsphere and fiber, respectively. Using the coupled-mode equations in this form requires the numerical integration of these simultaneous differential equations to understand how power transfers between the modes. The problem with this is that it takes many passes across the interaction region before the microsphere's field amplitude builds up and the system comes to equilibrium. For a typical desktop computer analysis, the amount of time the calculations take makes this method prohibitive for general use. The method does, however, allow the z-dependences of the fields to be known. An example is shown in Fig. 3.2. The plots show the z-dependences of the real parts of the fields of the microsphere and fiber modes after equilibrium has been reached. The inflection in the center of the fiber field plot indicates the phase shift associated with coupling when there is no intracavity loss.

Assuming weak coupling, the coupled-mode equations can be approximated as

$$\frac{\mathrm{d}E_s(z)}{\mathrm{d}z} \cong -i\beta_s E_s(z) + i\kappa_{sf}(z)|E_f(-\infty)|e^{-i(\beta_f z-\phi_f)}, \tag{3.20a}$$

$$\frac{\mathrm{d}E_f(z)}{\mathrm{d}z} \cong -i\beta_f E_f(z) + i\kappa_{fs}(z)|E_s(-\infty)|e^{-i(\beta_s z-\phi_s)}. \tag{3.20b}$$

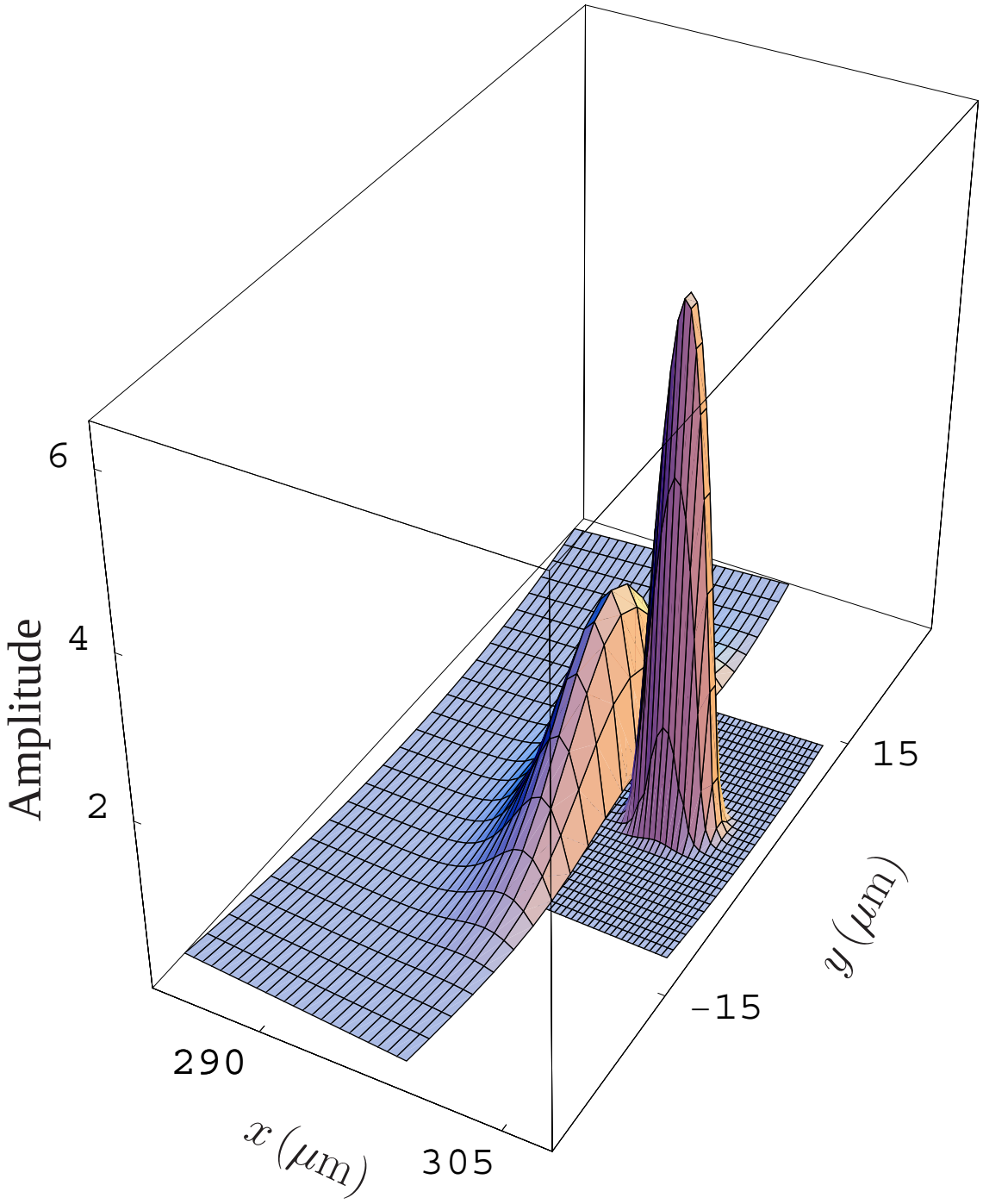

Figure 3.1. Mode Overlap for Fiber-Microsphere System. ($R_s = 300\,\mu$m, $R_f = 2.47\,\mu$m, $\lambda = 1550\,$nm). The WGM amplitude shown here is a fundamental TE mode as a function of the transverse profile. The mode's indices are $q = 1$, $l = m = 1730$.

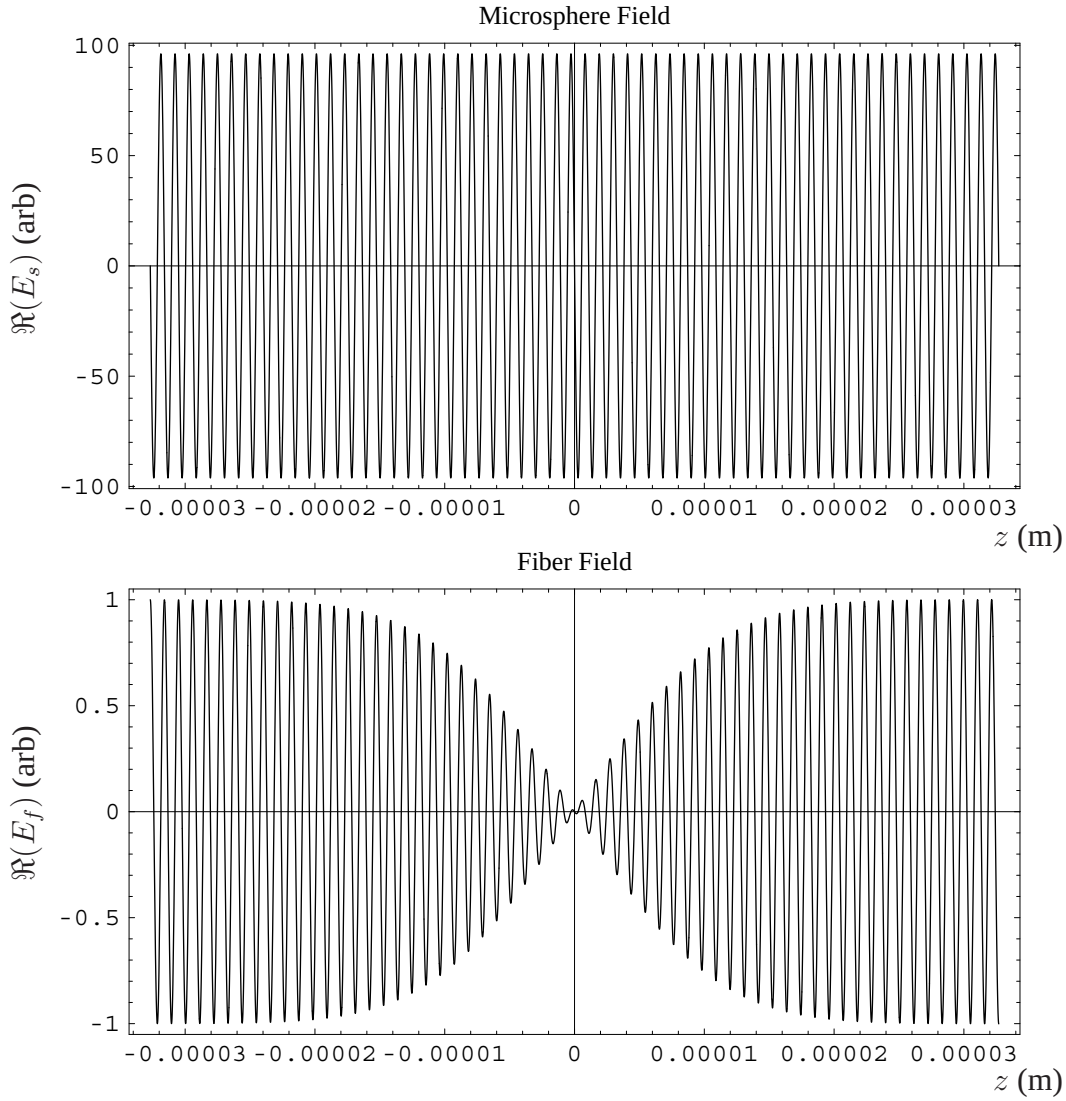

Figure 3.2. Integration of the Coupled-Mode Equations. The plots show the z-dependences of the real parts of the fields of the microsphere and fiber modes after equilibrium has been reached.

where ϕ_f and ϕ_s are the initial phase shifts of the fiber and microsphere modes, respectively. The solutions are

$$E_s(z) = |E_s(-\infty)|e^{-i(\beta_s z-\phi_s)} + i|E_f(-\infty)|e^{-i(\beta_s z-\phi_s)} \int_{-\infty}^{z} \kappa_{sf}(z')e^{-i[(\beta_f-\beta_s)z'-\phi_f]}\,\mathrm{d}z', \tag{3.21a}$$

$$E_f(z) = |E_f(-\infty)|e^{-i(\beta_f z-\phi_f)} + i|E_s(-\infty)|e^{-i(\beta_f z-\phi_f)} \int_{-\infty}^{z} \kappa_{fs}(z')e^{-i[(\beta_s-\beta_f)z'-\phi_s]}\,\mathrm{d}z'. \tag{3.21b}$$

The behavior of the modal fields after many passes is demonstrated by choosing $|E_f(-\infty)| = 1$ and $\phi_f = 0$. After many passes $|E_s(-\infty)| \approx 100$ and $\phi_s = \pi/2$. This can be seen in Fig. 3.2. The difference in the phases is a result of the imaginary number preceding the coupling coefficients in the coupled-mode equations. As a comparison, it is evident that this is a little different from the behavior in the single-mirror ring-cavity analogy. In the mirror cavity analogy, the phase of the reflected light is shifted by π and the transmitted light maintains its original phase. With the coupled-mode equations, there is no phase change in the "reflected" light, but there is a net phase shift of π for the transmitted light ($\pi/2$ as the light enters the microsphere and $\pi/2$ as the light exits the microsphere). The field in the fiber past the coupling region can be approximated by

$$\begin{aligned} E_f(z_{\text{final}}) &= |E_f(-\infty)| - |E_s(-\infty)|\tilde{\kappa}_{fs}, \\ -|E_f(-\infty)| &= |E_f(-\infty)| - |E_s(-\infty)|\tilde{\kappa}_{fs}, \\ -2|E_f(-\infty)| &= -|E_s(-\infty)|\tilde{\kappa}_{fs}, \end{aligned}$$

or

$$|E_s(-\infty)| = \frac{2|E_f(-\infty)|}{\tilde{\kappa}_{fs}}, \tag{3.22}$$

where

$$\tilde{\kappa}_{fs} = \int_{-\infty}^{\infty} \kappa_{fs}(z) e^{i(\beta_s - \beta_f)z}\, \mathrm{d}z. \tag{3.23}$$

This is similar to what is obtained using a ring-cavity model with unequal transmission coefficients (see Appendix C). The difference comes from the fact that, in the coupling region, light can tunnel from one waveguide to another and then back again. In an ordinary ring cavity, light does not return through a mirror once it has passed through it.

Equation (3.23) shows that the strength of the coupling is a combination of the amount of overlap and the amount of phase-matching between the modes. The relation between the fields implies that the coupling coefficient can be used to calculate the external quality factor (Q) of the microsphere when coupled to a fiber mode. The transmission from the microsphere to the fiber is just $T_{fs} = |\tilde{\kappa}_{fs}|^2$. This means that the quality factor due to

coupling is

$$\begin{aligned} Q &= \frac{4\pi^2 R_s n_{\text{eff}}}{\lambda_0 |\tilde{\kappa}_{fs}|^2} \\ &= \frac{2m\pi}{|\tilde{\kappa}_{fs}|^2}, \end{aligned} \tag{3.24}$$

where m is the third index of the microsphere mode.

3.2.2 Fiber-to-Microsphere Coupling (FMC)

The coupling strength from the fiber into the microsphere is found from the overlap integral

$$\kappa_{sf}(z) = \frac{\omega}{4} \iint_{-\infty}^{\infty} \left(\epsilon(x,y) - \epsilon_f(x,y)\right) \left(\mathbf{E}_f^t \cdot \mathbf{E}_s^{t\,*} + \frac{\epsilon_s(x,y)}{\epsilon(x,y)} E_f^z E_s^{z*} \right) \mathrm{d}x\, \mathrm{d}y, \tag{3.25}$$

where $\epsilon(x,y)$ is the permittivity profile for the composite system, $\epsilon_f(x,y)$ is the permittivity profile for the fiber, $\epsilon_s(x,y)$ is the permittivity profile for the microsphere, and $\mathbf{E}_{f(s)}^t$ and $E_{f(s)}^z$ are the transverse and longitudinal components of the electric field of the fiber (microsphere). In this case, the permittivity profiles are of the step-index kind and the coupling coefficient reduces to

$$\kappa_{sf} = \frac{\omega \epsilon_o}{4} \left(n_s^2 - n_o^2\right) \iint_{A_s} \left(\mathbf{E}_f^t \cdot \mathbf{E}_s^{t\,*} + E_f^z E_s^{z*} \right) \mathrm{d}x\, \mathrm{d}y. \tag{3.26}$$

Because the integration is over the interior of the microsphere, the integration over the transverse slice is represented in polar coordinates,

$$\kappa_{sf} = \frac{\omega \epsilon_o}{4} \left(n_s^2 - n_o^2\right) \iint_{A_s} \left(\mathbf{E}_f^t \cdot \mathbf{E}_s^{t\,*} + E_f^\phi E_s^{\phi *} \right) r\, \mathrm{d}r\, \mathrm{d}\theta. \tag{3.27}$$

Accounting for both phase mismatch and field overlap the strength is

$$\tilde{\kappa}_{sf} = \int_{-\pi}^{\pi} \kappa_{sf}(\phi) e^{-i\Delta\beta r\phi}\, r\, \mathrm{d}\phi, \tag{3.28}$$

where $\Delta\beta = \beta_s - \beta_f$. The total coupling strength, found by combining the integrals in Eqs. (3.27) and (3.28), is

$$\tilde{\kappa}_{sf} = \frac{\omega \epsilon_o}{4} \left(n_s^2 - n_o^2\right) \iiint_{V_s} \left(\mathbf{E}_f^t \cdot \mathbf{E}_s^{t\,*} + E_f^z E_s^{z*} \right) \cos\left(m\phi - r\beta_f \sin\phi\right)\, r^2\, \mathrm{d}r\, \mathrm{d}\theta\, \mathrm{d}\phi. \tag{3.29}$$

Note that the real part of the interference term is sufficient for calculating the effects of phase mismatch.

Because the integration is performed over the volume of the microsphere, the fiber fields must be expressed in the microspheres coordinate system. The axes of the fiber coordinate system are oriented so that the fiber's y-axis points toward the microsphere and its x-axis is parallel to the microsphere's $\hat{\theta}$-vector at the nearest point. The transverse and longitudinal components of the fiber become

$$\begin{aligned}\mathbf{E}_f^t &= \hat{r}\left(E_f^x \sin\theta - E_f^y \cos\theta\cos\phi + E_f^z \sin\phi\right) \\ &\quad + \hat{\theta}\left(E_f^x \cos\theta + E_f^y \sin\theta\cos\phi\right), \qquad (3.30a)\\ \mathbf{E}_f^\phi &= \hat{\phi}\left(E_f^y \cos\theta\sin\phi + E_f^z \cos\phi\right). \qquad (3.30b)\end{aligned}$$

The terms of the integrand may now be expressed as:

•Microsphere TE Mode

$$\begin{aligned}\mathbf{E}_f^t \cdot \mathbf{E}_s^{t\,*} &= E_s^{\theta *}\left(E_f^x \cos\theta + E_f^y \sin\theta\cos\phi\right), \qquad (3.31a)\\ E_f^z E_s^{z*} &= 0. \qquad (3.31b)\end{aligned}$$

•Microsphere TM Mode

$$\begin{aligned}\mathbf{E}_f^t \cdot \mathbf{E}_s^{t\,*} &= E_s^{r*}\left(E_f^x \sin\theta - E_f^y \cos\theta\cos\phi + E_f^z \sin\phi\right), \qquad (3.32a)\\ E_f^z E_s^{z*} &= E_s^{\phi *}\left(E_f^y \cos\theta\sin\phi + E_f^z \cos\phi\right). \qquad (3.32b)\end{aligned}$$

3.2.3 Microsphere-to-Fiber Coupling (MFC)

The range of the overlap integral when coupling from the microsphere to the fiber is taken over the fiber. The coupling coefficient is calculated by evaluating

$$\tilde{\kappa}_{fs} = \frac{\omega\epsilon_o}{4}\left(n_f^2 - n_o^2\right)\iiint_{V_f}\left(\mathbf{E}_s^t \cdot \mathbf{E}_f^{t\,*} + E_s^z E_f^{z*}\right)\cos\left[m\tan^{-1}\left(\frac{z}{r}\right) - \beta_f z\right] r\,\mathrm{d}r\,\mathrm{d}\theta\,\mathrm{d}z. \qquad (3.33)$$

Notice that Eq. (3.33) is in cylindrical coordinates rather than spherical coordinates that are used when going from the fiber to the microsphere. The transverse and longitudinal

components of the microsphere fields as expressed in the fiber coordinate system are

$$\mathbf{E}_s^t = \hat{x}\left(E_s^{r_2}\sin\theta_2 + E_s^{\theta_2}\cos\theta_2\right) + \hat{y}\left(-E_s^{r_2}\cos\theta_2\cos\phi + E_s^{\theta_2}\sin\theta_2\cos\phi + E_s^{\phi}\sin\phi\right), \tag{3.34a}$$

$$\mathbf{E}_s^z = \hat{z}\left(E_s^{\phi}\cos\phi\right), \tag{3.34b}$$

where $r_2 = r_2(r,\theta,z)$ and $\theta_2 = \theta_2(r,\theta)$ are the microsphere coordinates as functions of the fiber coordinates.

•TE Mode

$$\mathbf{E}_s^t \cdot \mathbf{E}_f^{t\,*} = E_s^{\theta_2}\left(E_f^{x*}\cos\theta_2 + E_f^{y*}\sin\theta_2\cos\phi\right), \tag{3.35a}$$

$$E_s^z E_f^{z*} = 0. \tag{3.35b}$$

•TM Mode

$$\mathbf{E}_s^t \cdot \mathbf{E}_f^{t\,*} = E_s^{r_2}E_f^{x*}\sin\theta_2 + \left(-E_s^{r_2}\cos\theta_2\cos\phi + E_s^{\phi}\sin\phi\right)E_f^{y*}, \tag{3.36a}$$

$$E_s^z E_f^{z*} = E_s^{\phi}E_f^{z*}\cos\phi. \tag{3.36b}$$

3.3 Tapered Fiber

As was mentioned in the introduction to this chapter, tapering of a fiber can be treated as a perturbation to the cylindrical case. In the untapered portion of the fiber, the fiber is a single-mode step-index fiber. This is because of the small size of the core relative to the transmission wavelength and because of the low index contrast between the core and the cladding. In this portion of the fiber, the HE_{11} mode can be approximated as the LP_{01} mode. In the portion of the fiber where the tapering is occurring, more of the mode extends into the cladding of the fiber. Eventually, where the core is very small, the cladding takes over the role of the core and the air (or liquid) outside of the fiber assumes the role of the cladding. In the non-cylindrical section, or taper transition region, a superposition of modes is required to satisfy the Maxwell equations. This means that power can transfer from the HE_{11} mode to other modes. According to coupled-mode theory, the amount of this transfer is dependent on the overlap between the modes and the phase-matching between

them. Due to symmetry, the only modes that have non-zero overlap with the HE_{11} mode are those in the same family – the HE_{1m} family. If the taper transition is gentle enough, the phase-matching effects result in the HE_{12} mode being the only mode that can have a non-negligible amount of coupling.

A taper transition is considered adiabatic if its shape permits only a negligible amount of coupling to the HE_{12} mode. Whether or not a taper transition is adiabatic is important because of the effects in the fiber-microsphere system. If two fiber modes couple into the microsphere, the system has many more variables and becomes more difficult to analyze. However, it has been found that under certain conditions coupling from two fiber modes can increase the effective absorption length in a sensing experiment, making it much better for sensing low concentrations of a substance.[57] These considerations mean that it is important to know the conditions for taper transition adiabicity.

A simple model is the length-scale criterion for taper transition adiabicity.[58,59] In this model, a local taper-length scale is defined to be the base of the right triangle that has the radius of the fiber as the opposite side. The local taper transition angle is given by

$$\Omega(z) = \tan^{-1}\left[\frac{\mathrm{d}r}{\mathrm{d}z}\right]. \tag{3.37}$$

The local taper length can be approximated as

$$z_t \approx \frac{r(z)}{\Omega(z)}, \tag{3.38}$$

because the taper transition angle is always small. For a taper transition to be adiabatic, the local taper length must be much greater than the local beat length (such as in acoustical waves), or $z_t \gg z_b$, where the local beat length is given by

$$z_b = \frac{2\pi}{\beta_{11}(r) - \beta_{12}(r)}, \tag{3.39}$$

where β_{11} and β_{12} are the propagation constants of the HE_{11} and HE_{12} modes. The upper limit of the taper transition angle can be calculated by setting taper length equal to the beat length. By combining Eqs. (3.37)–(3.39), this is expressed by the differential equation

$$\frac{\mathrm{d}r}{\mathrm{d}z} = \tan\left[\frac{r(\beta_{11}(r) - \beta_{12}(r))}{2\pi}\right]. \tag{3.40}$$

This can be solved numerically by fitting expressions for the propagation constants, which are found in the methods discussed in Chapter 2. For the section of the fiber that has a radius large enough to only core guide the HE_{11} mode, the angle of the taper transition can be steep, but not arbitrarily so. Although the HE_{12} and other higher-order modes are cut off, coupling to them is still possible. This is because they are actually radiation modes of the fiber. These modes have propagation constants equal to the wavenumber of the cladding, or

$$\beta_{12} = k_0 n_{\text{cl}}, \tag{3.41}$$

where n_{cl} is the index of refraction of the cladding. As the fiber radius decreases, it reaches a section where the propagation constant of the HE_{11} mode in the core is close to when guided by the cladding. At this point, the angle of the taper transition must be decreased. This is because the HE_{11} mode undergoes the transition from being core guided to cladding guided. At this portion of the taper transition, the cladding can easily guide many modes, as its diameter is large compared to the wavelength of the light. Immediately after the transition, the taper transition angle must be very small because the propagation constants of the fiber modes are very close. As the fiber radius is further decreased, the angle of the taper transition may again be increased. This is because the higher-order modes' propagation constants decrease more than the propagation constant for the fundamental mode as the fiber radius is decreased. As the size of the fiber is reduced even further, the HE_{12} mode is cut off. This means that it must again be treated as a radiation mode. An example of the taper transition shape for the region where the cladding guides both the HE_{11} and the HE_{12} modes is shown in Fig. 3.3. The figure shows the shape of the taper transition when $z_t = z_b$. For the taper transition to be truly adiabatic, the length needs to be multiplied by several orders of magnitude. This is useful because in an experiment the length of the taper transition needs to be minimized. This method can be used to provide such a taper transition.

This chapter has discussed coupled-mode theory and how it applies to coupling between microsphere and fiber modes, and also how it applies to coupling between fiber

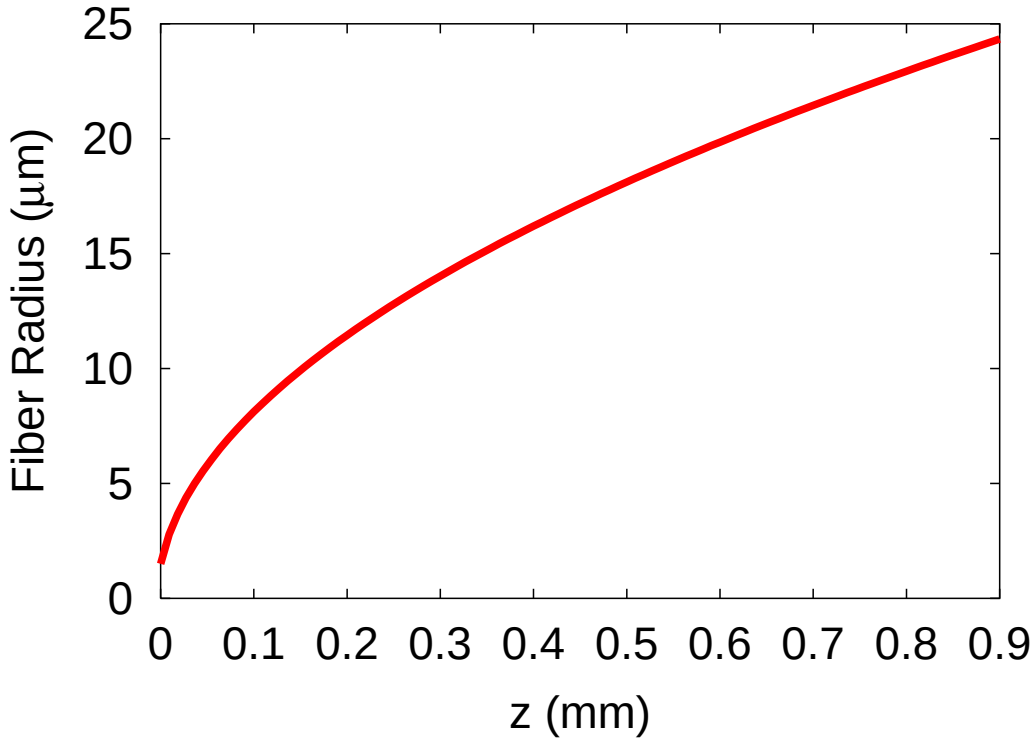

Figure 3.3. Taper Transition Profile as a Function of Longitudinal Distance. The profile has been found for the region where the cladding guides both the HE_{11} and the HE_{12} modes. In this case, the taper length is equal to the beat length.

modes within a tapered fiber. The next chapter uses this development to calculate the optimal fiber radius of a microsphere-fiber system, to calculate the WGM spectrum of the system, and to study the lasing of a coated microsphere.

CHAPTER 4

APPLICATIONS

Coupled-mode theory as it pertains to the fiber-microsphere system was presented in Chapter 3. Chapter 4 uses the coupled-mode theory to explain optimal and imperfect conditions for this system. The amount of coupling between fiber and microsphere modes is strongly dependent on the sizes of the fiber and sphere. The first section of this chapter presents calculations of the optimal taper size for a microsphere of given size. This is followed by calculations of whispering-gallery mode spectra with imperfect alignment of the fiber and microsphere. The chapter concludes with a laser model that incorporates the WGMs and some unusual effects of their presence.

4.1 Optimal Fiber Radius

The optimal taper radius is that which maximizes coupling from the fiber HE_{11} mode to the microsphere mode while minimizing coupling of the microsphere mode to the higher-order fiber modes. As was discussed in Sec. 3.3, higher-order fiber modes not in the HE_{1m} family do not couple to the HE_{11} mode in the taper transitions. This means that power in these modes is lost at the second end of the bitaper. Figure 4.1 shows the approximate activation of modes along the entire system. Before the first taper transition, all of the light is in the HE_{11} mode because the untapered portion of the fiber is only single mode. After the first taper transition, the power is divided between the HE_{11} and HE_{12} modes. Both of these modes couple into the microsphere mode. Light in the microsphere's WGM can then couple into all of the modes supported by the fiber taper. Shown in Fig. 4.1 are the modes that have propagation constants between the HE_{11} and HE_{12} modes. In order of descending propagation constant, the modes in this second portion of the fiber taper are: HE_{11}, TE_{01}, HE_{21}, TM_{01}, EH_{11}, HE_{31}, and HE_{12}. These are the modes that are discussed in Sec. 2.4.2.

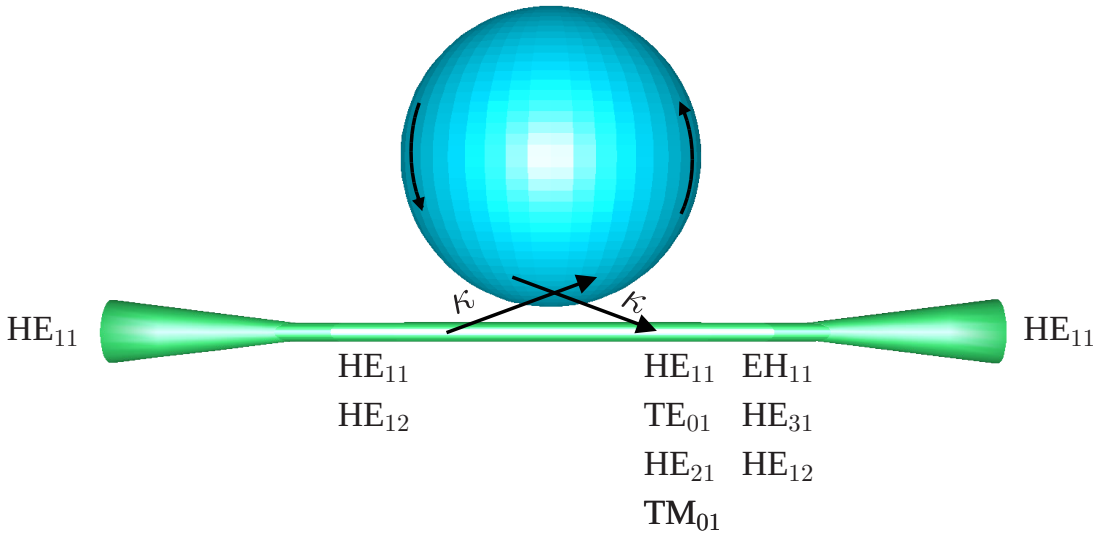

Figure 4.1. Taper-Coupled Microsphere

The optimal taper radius is determined by calculating the coupling coefficient between the fiber and microsphere. Under conditions defined below for FMC, the coupling coefficients for the HE_{11} and HE_{12} fiber modes are calculated with respect to coupling to either the TE or TM WGMs of the microsphere as a function of the radius of the fiber taper. Any maxima that develop in the curves reflect optimal coupling conditions for a given radius of the microsphere. These optimal coupling conditions can be explained in terms of the two factors identified in Chapter 3: the amount of overlap of the respective fiber-microsphere modes and the phase matching between them.

Figure 4.2 shows the dependence of FMC on the radius of the taper with respect to both the HE_{11} and HE_{12} fiber modes. The conditions of the numerical calculations are chosen such that the fiber and microsphere are placed in contact with each other and that the microsphere size remains fixed. In Fig. 4.2, the most important feature is reflected by the coupling of the fiber HE_{11} mode to the TE or TM fundamental modes of the microsphere. Here the strongest couplings occur at maxima where the fiber radius is smaller than the radius for perfect phase matching between modes (indicated by lines A and B). The reason for the increase in the coupling strength for smaller radii than for the phase-matching point is seen directly from Eq. (3.29). As the taper radius is decreased (from the point of phase

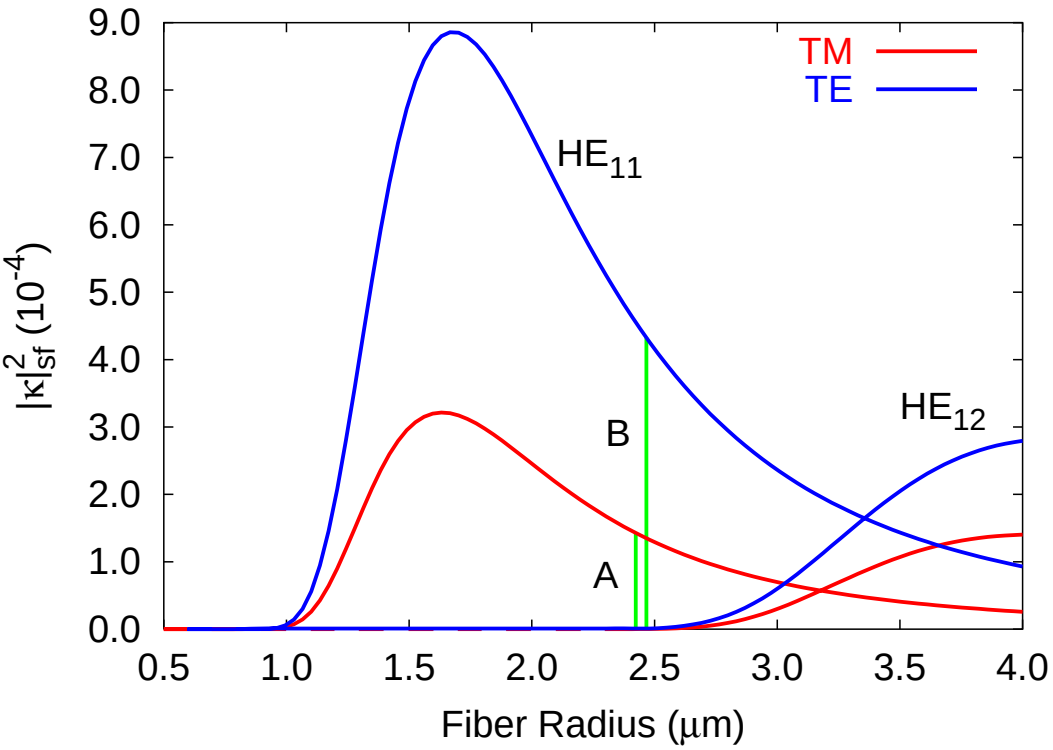

Figure 4.2. Optimal Fiber Radius. ($R_s = 300\,\mu$m, $\lambda = 1550$ nm) with FMC. The lines that peak on the left are for HE_{11} coupling and lines that peak on the right are for HE_{12} coupling. The vertical green lines A and B indicate where the fiber HE_{11} mode is perfectly phase-matched to the fundamental microsphere TM and TE modes, respectively.

matching), the spatial overlap of the fields is increased. At the same time, the increasing phase mismatch causes destructive interference between the two modes. The increasing effect of the spatial overlap is stronger than the decreasing effect of the phase mismatch until the radius that maximizes the coupling coefficient is reached. For radii below this, the decreasing effect of the phase mismatch is stronger than the increasing effect of the spatial overlap.

The HE_{11} and HE_{12} modes have their strongest coupling at different taper radii. Thus by changing the taper radius, the coupling can be selected to identify either of these modes. Similarly, at a certain radius of the taper, the coupling can be chosen to incorporate a superposition of the two modes. See, for example, a radius in the range of 3.0 – 3.5 μm in Fig. 4.2. Both the HE_{11} mode and the HE_{12} mode couple less strongly to the microsphere

TM modes than to the microsphere TE modes. This can be explained by the nature of the microsphere TE and TM modes themselves. When coupling to the TE modes, the electric fields in the coupling region are parallel to the surfaces of the microsphere and fiber. When coupling to the TM modes, the transverse electric fields are perpendicular to the surfaces and are discontinuous. This is accompanied by nonzero longitudinal field components. Figure 4.2 indicates that the contributions of the transverse and longitudinal components of the fields in Eq. (3.29) are opposing for both the HE_{11} and the HE_{12} modes because the coupling is stronger to the TE mode than to the TM mode.

In the previous discussion, only the fiber-to-microsphere mode coupling is examined. It is appropriate, however, to consider also the microsphere-to-fiber light coupling. In the latter process, there are more taper modes available for the microsphere WGMs to excite. The coupling strengths are calculated for all modes with propagation constants between that of the HE_{11} and HE_{12} modes as functions of the radius as in FMC; but, in this case, the range of integration of the overlap integral is over the volume of the fiber, as was shown in Chapter 3 (see Eq. (3.33)). For comparison, the fundamental microsphere TE and TM modes are selected to be individually coupled to the taper modes (see Figs. 4.3 and 4.4, respectively). In both cases, the strongest coupling strength for a small taper radius of ~ 1.5 μm is the HE_{11} mode. Close behind are the next maximal coupling coefficients corresponding to the TE_{01} (in Fig. 4.3) and the TM_{01} (in Fig. 4.4) with the HE_{21} taper mode in third place for radii in the range of ~ 2.6 – 2.7 μm. As was mentioned in Sec. 2.4.2, a superposition of the TE_{01}, HE_{21}, and TM_{01} fiber modes forms the LP_{11} mode in the LP-approximation. The reason that coupling from the TE microsphere modes to the TE_{01} mode is noticeably stronger than to the HE_{21} mode is that all of the TE_{01}'s power is in the transverse direction. The strength of the coupling from the TM microsphere mode to the HE_{21} and TM_{01} modes is almost identical because both of these fiber modes have both transverse and longitudinal components. Note in Figs. 4.3 and 4.4 that if a radius is selected at ~ 2.5 μm (the HE_{11} phase-matched point indicated by lines A and B in Fig. 4.2), the strength of the coupling to the fiber TE_{01}, HE_{21}, and TM_{01} modes is very close to that of the HE_{11} mode.

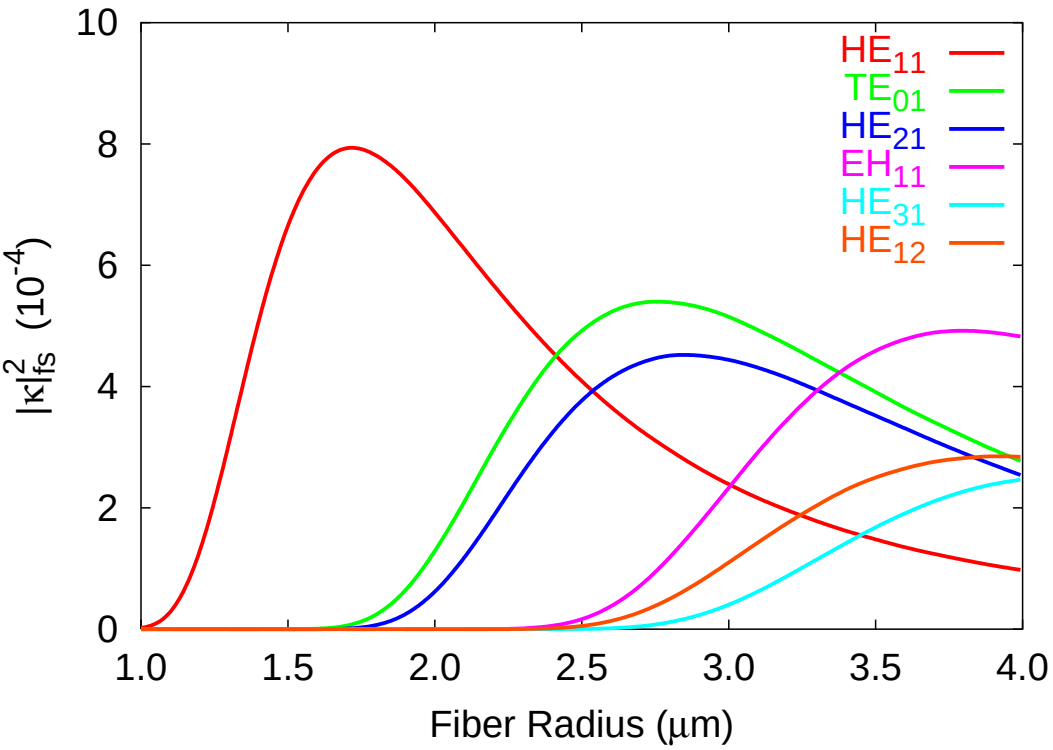

Figure 4.3. Coupling from Fundamental Microsphere TE mode to Higher-Order Fiber Modes

With MFC, coupling with the higher-order modes (HE_{12}, HE_{31}, and EH_{11}) of the taper occurs at larger radii (3.0 μm – 4.0 μm) and is sequentially different in strength with respect to the TE and TM modes of the microsphere. In the case of the TE mode coupling (Fig. 4.3), the third highest coupling strength corresponds to the EH_{11} taper mode followed by the HE_{12} and the HE_{31}. There is no unexpected behavior in the functional development of these higher-order modes as their coupling strengths are calculated as functions of the increase in radius – i.e., for any given range of the radius, the sequence of behavior of the relative coupling strengths stays consistent as the radius increases. There are interesting differences in the case of the TM mode coupling to the higher-order fiber modes (Fig. 4.4). First, note that the third highest coupling strength corresponds to the HE_{12} taper mode followed by the HE_{31} and the EH_{11}, a sequence that is completely different from TE mode coupling (Fig. 4.3). Second, not only is the order of the coupling strength between these modes different from the TE mode coupling, but there is a functional crossing of coupling

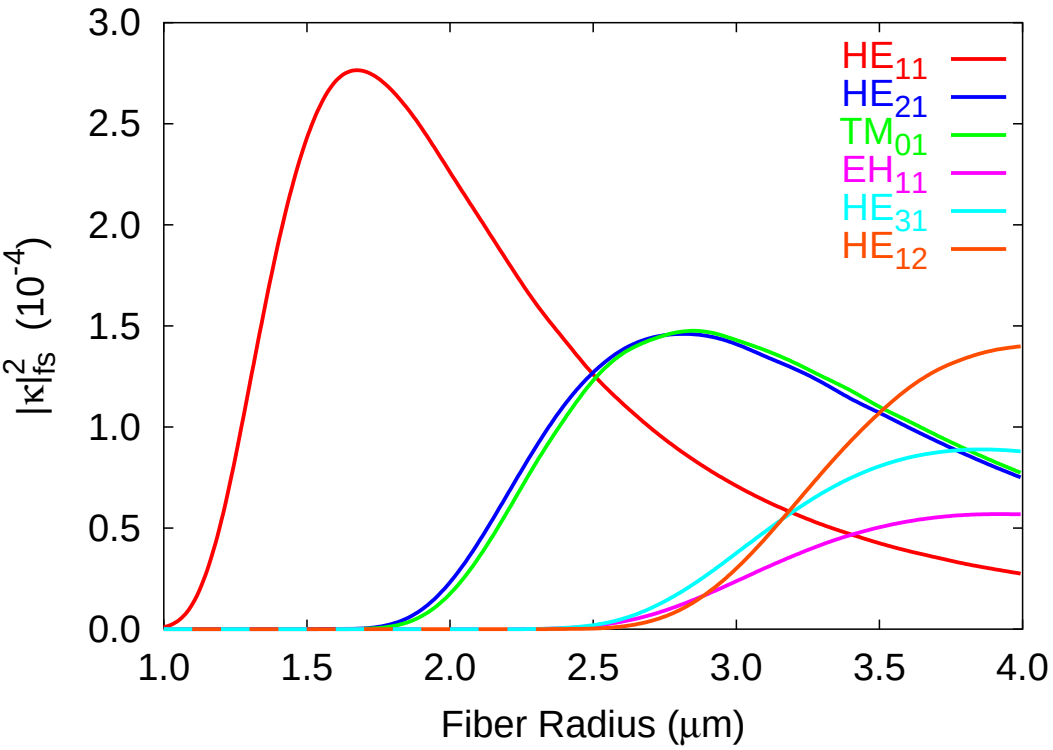

Figure 4.4. Coupling from Fundamental Microsphere TM Mode to Higher-Order Fiber Modes.

strengths for these three modes within the radius range of $\sim$ 2.5 – 3.2 μm. Because the range of the coupling strengths is small and this is MFC, it is not clear that this crossing behavior is physically determinable.

The dependence of the optimal taper radius on the microsphere size for FMC of the HE_{11} taper mode is shown in Figs. 4.5 and 4.6. For a given wavelength, the ratio of the optimal radius to the phase-matched radius is weakly dependent on the size of the microsphere. The greatest ratio occurs for a microsphere radius of $\sim$ 100 μm for all four wavelengths, ranging from 800 – 1900 nm, with the largest ratio reflected in the largest wavelength of 1900 nm. (see Fig. 4.5 for HE_{11} FMC). Similarly, in Fig. 4.6, the ratio of the peak coupling strength to the phase-matched coupling strength is calculated and, as in the previous case, is found to be weakly dependent on the microsphere size. For all four wavelengths, the coupling strength is roughly doubled by using the optimal taper radius rather than the phase-matched radius. Similar results are found also when optimizing for

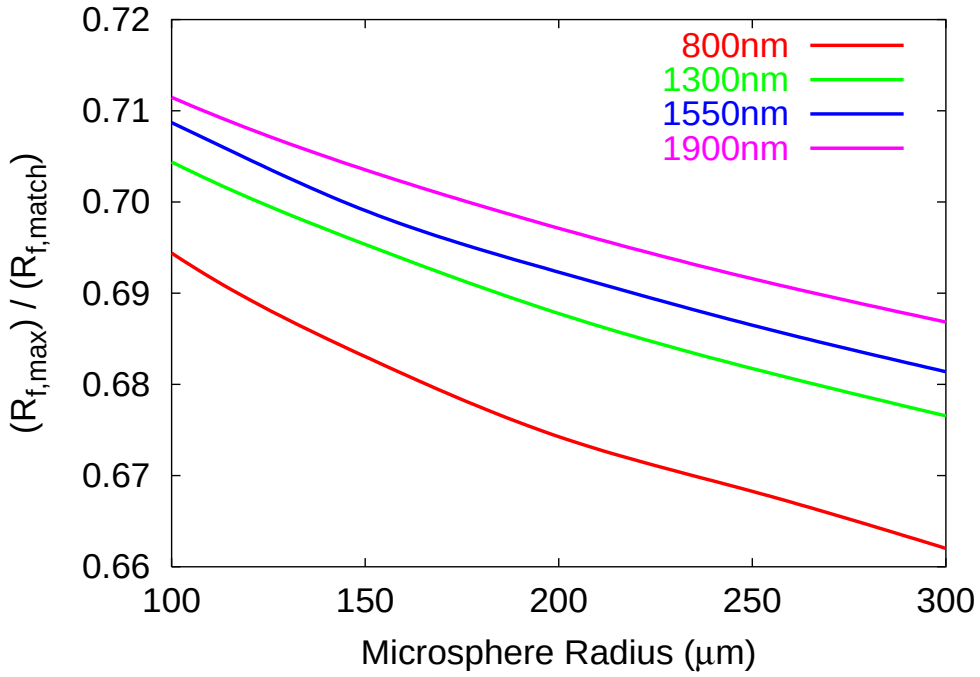

Figure 4.5. Ratio of Optimal Radius to Phase-Matched Radius (Fiber HE_{11} to Microsphere TE Coupling).

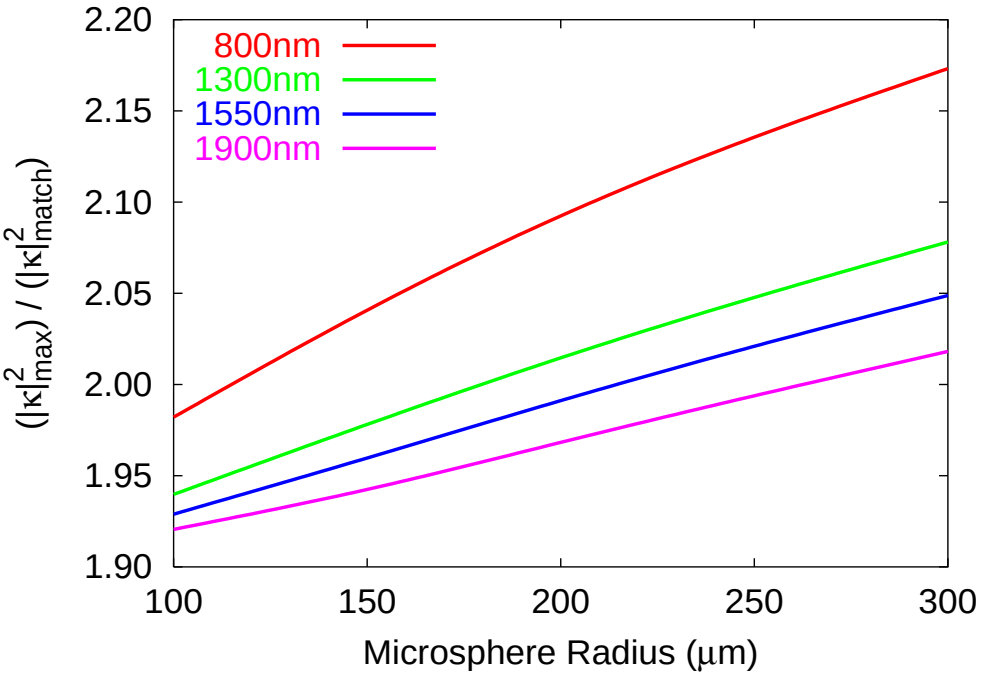

Figure 4.6. Ratio of Optimal Coupling Coefficient to Phase-Matched Coupling Coefficient (Fiber HE_{11} to Microsphere TE Coupling).

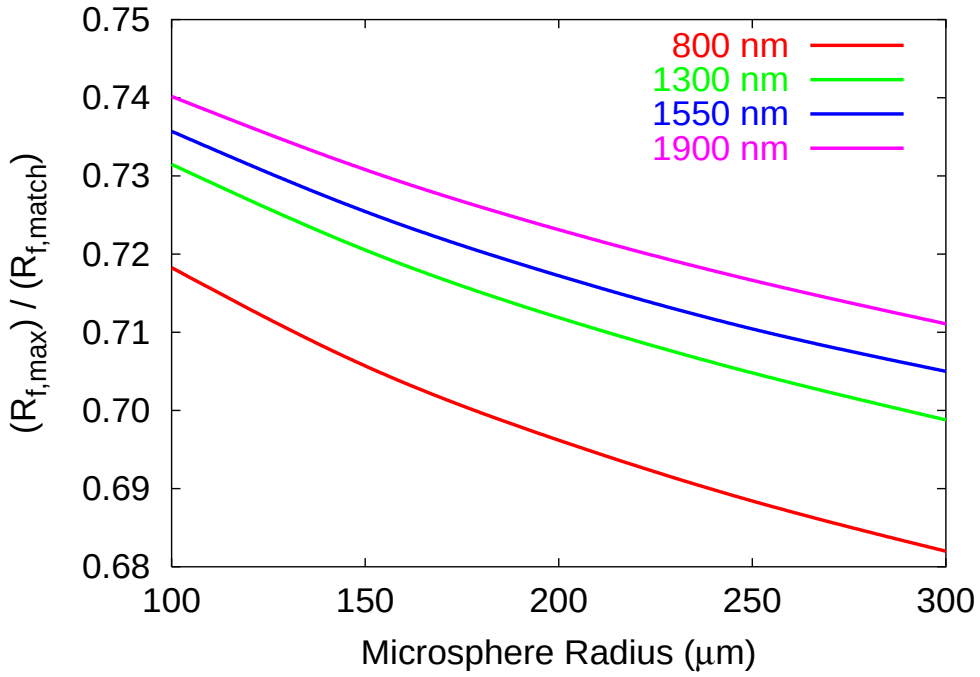

Figure 4.7. Ratio of Optimal Radius to Phase-Matched Radius (Fiber HE_{12} to Microsphere TE Coupling).

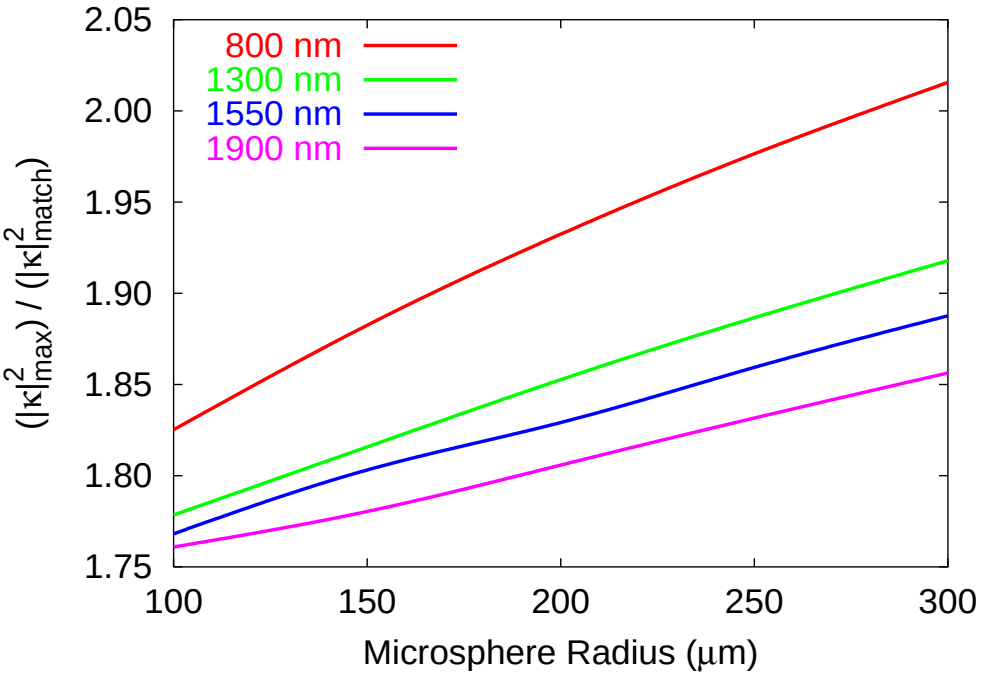

Figure 4.8. Ratio of Optimal Coupling Coefficient to Phase-Matched Coupling Coefficient (Fiber HE_{12} to Microsphere TE Coupling).

the HE_{12} taper mode. This is shown in Figs. 4.7 and 4.8. The only difference is that in the latter case of HE_{12} coupling the peak–to–phase-matched radius ratio is a little higher than for HE_{11} coupling while the peak–to–phase-matched coupling coefficient ratio is a little smaller. The peak–to–phase-matched radius ratio and the peak–to–phase-matched coupling coefficient ratios are useful because the phase-matched radius is easy to calculate. Once the phase-matched radius and the corresponding coupling coefficient are calculated, the optimal fiber radius and its coupling coefficient can be quickly determined.

The dependence of the coupling on microsphere size is more fully understood when a comparison of the actual coupling coefficients is considered in addition to only considering the ratios. The dependence of FMC of the HE_{11} mode is shown in Fig. 4.9. The figure shows that as the microsphere size is decreased the optimal taper radius decreases while the coupling strength increases. The optimal taper radius decreases because the propagation constant of the microsphere decreases with smaller sizes. The taper size must then be decreased for better phase matching. The coupling coefficients increase with decreasing microsphere size because the spatial overlap of the fields is increased. The same trends are found for HE_{12} MFC, as is shown in Fig. 4.10.

The dependence of the coupling strength on the wavelength is shown in Figs. 4.11 and 4.12 for FMC. These figures show that as the wavelength increases from 800 nm to 1900 nm the optimal taper radius increases as does the coupling strength. The coupling strength increases because the evanescent portions of the modes increase. The optimal taper radius increases because the taper size must be increased to maintain a small amount of phase mismatch with the WGM. This is because increasing the wavelength causes a larger decrease in the propagation constant for the fiber mode than that for the microsphere mode, as the wavelength of the light is closer to the size of the fiber than to the size of the microsphere.

The effects of immersing the entire fiber-microsphere system in a fluid other than air are also interesting and are shown in Fig. 4.13. In this figure, the blue lines indicate the coupling when the system is in air ($n_{\text{air}} = 1.00$) and the red lines indicate the coupling when the system in in a liquid ($n_{\text{liquid}} = 1.33$). The figure shows that the optimal taper radius for HE_{11} is only slightly changed by the immersion. The shift of the optimal taper radius for

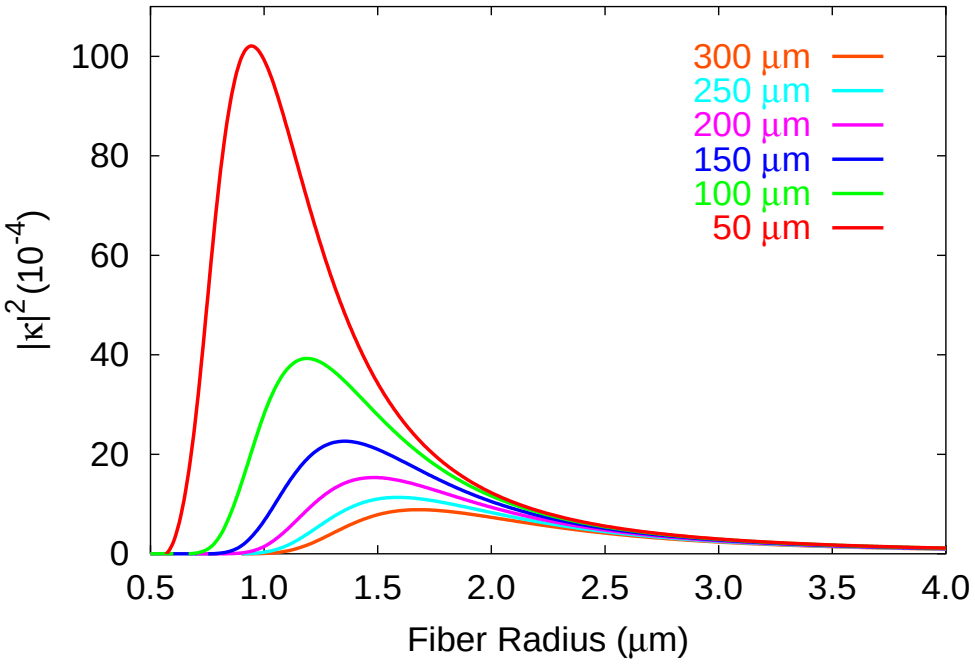

Figure 4.9. Optimal Fiber Radius for Different Microsphere Sizes. FMC for fiber HE_{11} mode to microsphere TE mode.

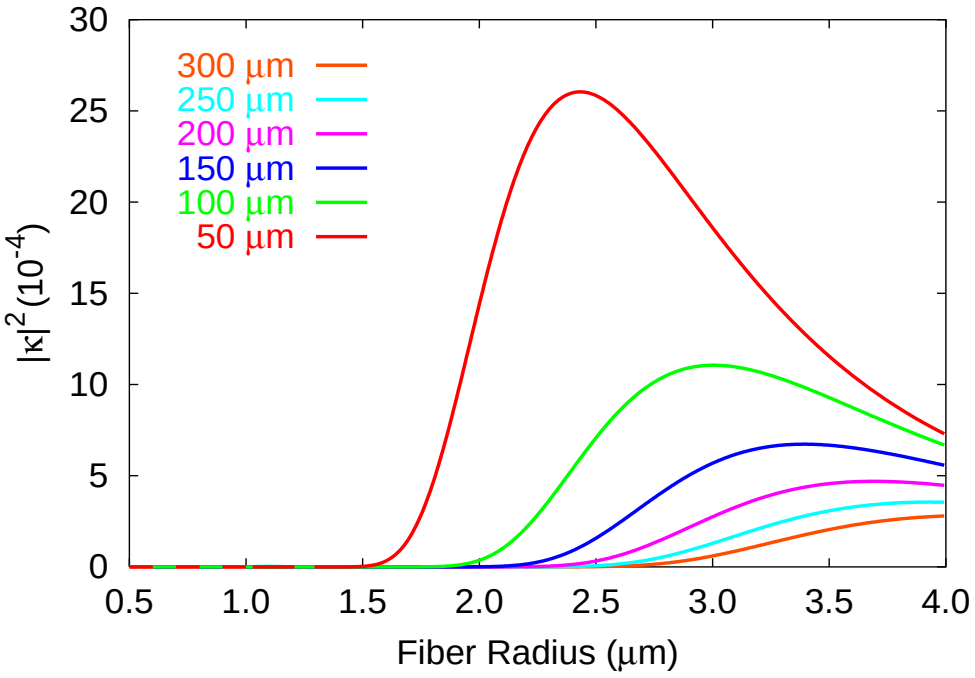

Figure 4.10. Optimal Fiber Radius for Different Microsphere Sizes. FMC for fiber HE_{12} mode to microsphere TE mode.

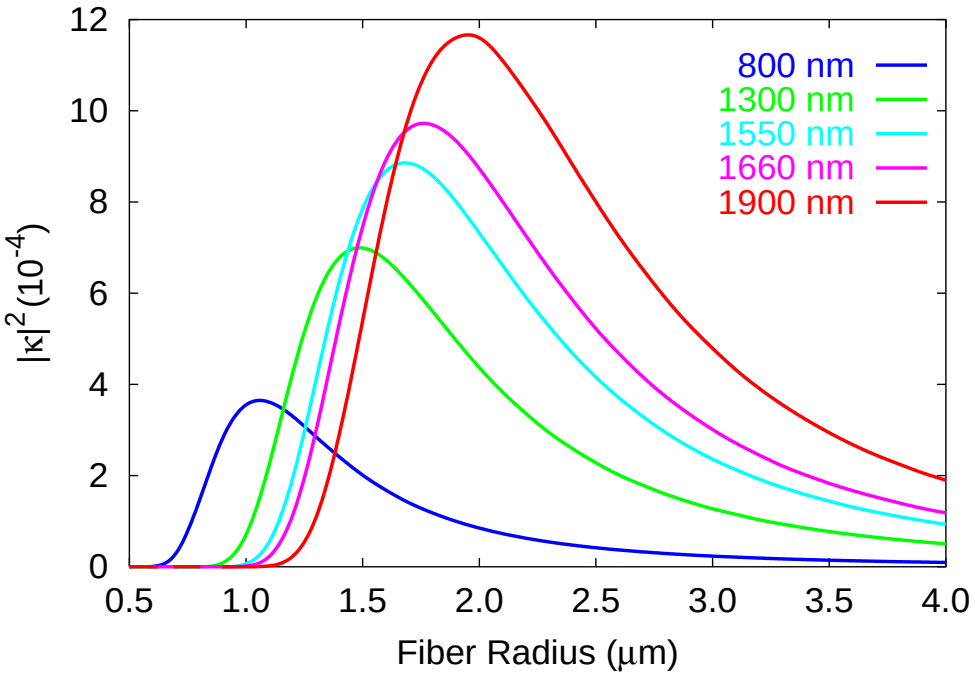

Figure 4.11. Optimal Fiber Radius for Different Wavelengths. FMC for fiber HE_{11} mode to microsphere TE mode.

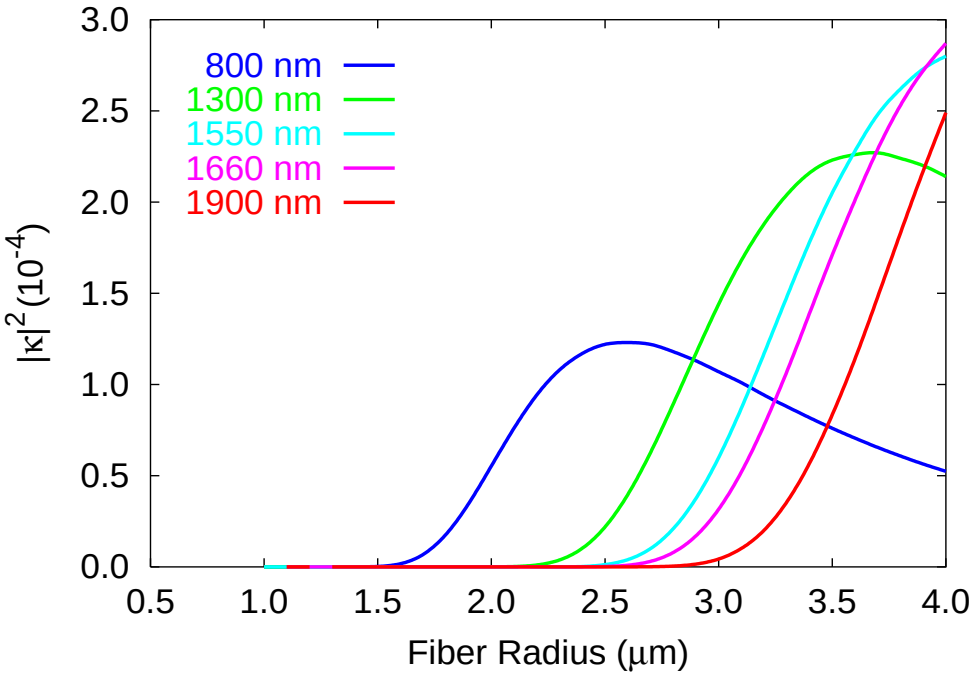

Figure 4.12. Optimal Fiber Radius for Different Wavelengths. FMC for fiber HE_{12} mode to microsphere TE mode.

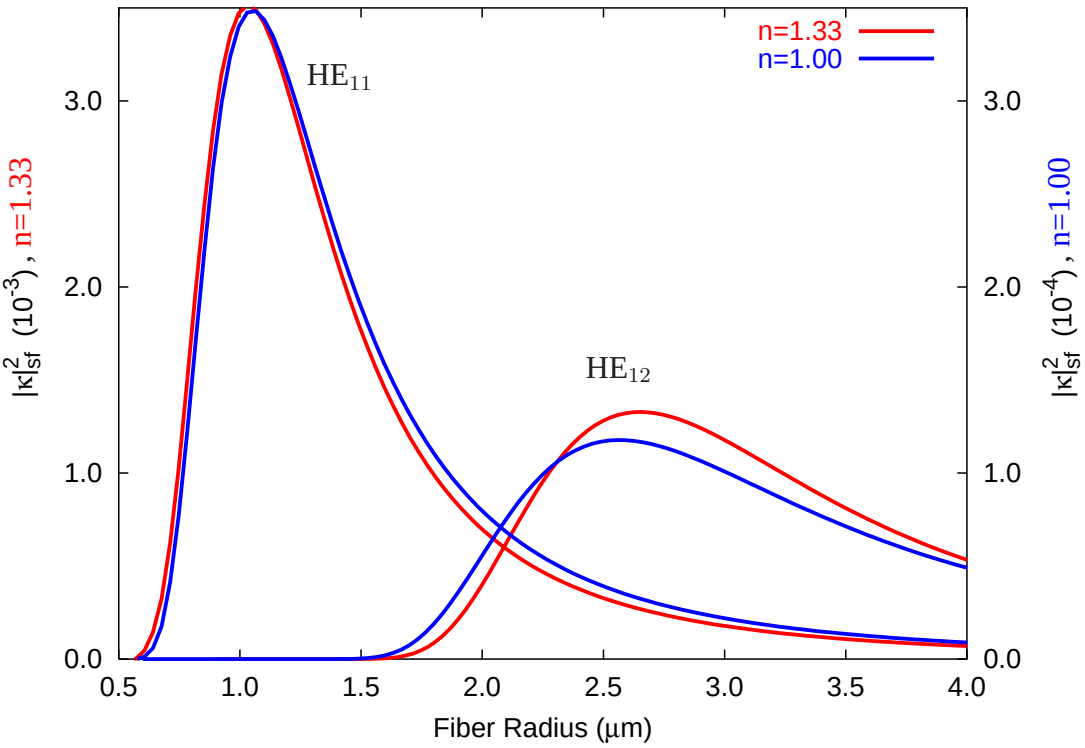

Figure 4.13. Optimal Fiber Radius when Immersed for FMC ($R_s = 300\,\mu$m, $\lambda = 800\,$nm, Fundamental TE WGM). The blue lines indicate the coupling when the system is in air and the red lines indicate the coupling when the system is immersed. The vertical scale on the left and right correspond to coupling in the liquid and air systems, respectively.

HE_{12} coupling is more noticeable, but still small. Also, notice for both the HE_{11} and HE_{12} modes that the coupling strengths are an order of magnitude larger for the immersed system (vertical axes are scaled differently). This is a result of the modes having higher evanescent fractions when the system is immersed. These results are important because they indicate that a fiber-microsphere system that has been designed for gas sensing can be used for liquid sensing as well.

The discussion of optimal taper radius is not complete without some remarks about the polarization of the modes. In FMC, the orientation of the HE_{11} and HE_{12} fiber fields is used to choose whether the coupling is to TE or TM microsphere modes. For coupling to TE microsphere modes, the orientation is chosen such that the transverse fields are parallel to the surfaces of the fiber and microsphere within the interaction region. For coupling to

TM modes, the orientation is chosen so that the fields are perpendicular in the interaction region. In MFC, the orientations are chosen in the same manner. However, coupling is possible for modes whose orientations are in-between being perfectly perpendicular and parallel to the surfaces in the interaction region. In fact, none of the modes can be oriented completely as in either of these situations. This is because the modes of the taper are not linearly polarized. Although the orientation of the fields can be used to cause the coupling to be primarily to microsphere TE or TM modes, the orientation can never entirely eliminate coupling to either of these families of modes. Calculations, not shown here, indicate that at best the opposite polarization has coupling as low as about two and a half orders of magnitude less than the primary polarization.

Coupled-mode theory indicates that FMC and MFC should be equal for cases where the microsphere mode and taper mode are phase-matched. The fact that they are equal in these calculations indicates consistency between the integration methods. Note that, at the optimal taper radius, FMC (Fig. 4.2) is about 10% larger than MFC (Figs. 4.3 and 4.4) because $\beta_s > \beta_f$ when the fiber radius is less than the phase-matched radius (see Eq. (3.8)). This means that light enters the microsphere more easily than in an ordinary ring cavity of the same quality factor.

4.2 Whispering-Gallery Mode Spectra

The microsphere whispering-gallery mode spectra are calculated by numerically integrating the field overlap integral (Eq. (3.29)). However, in this case the fiber is offset from the equatorial plane of the microsphere, as seen in Fig. 4.14, in order to account for imperfect alignment in an experiment. In this configuration, non-zero overlap is possible between the fiber mode and odd polar modes of the microsphere. This is in addition to the even polar modes that are coupled to when the alignment is perfect. Also, the frequency degeneracy of the polar modes is broken by including the eccentricity of the (oblate) microsphere. Converting Eq. (2.23) to wavelength results in

$$\lambda' = \left[\frac{1}{\lambda} - \frac{\varepsilon^2}{4\pi R_s n_s}(m' - m)\right]^{-1}, \tag{4.1}$$

where ε is the eccentricity, $m = l$, and λ' and m' are for the higher order polar modes.

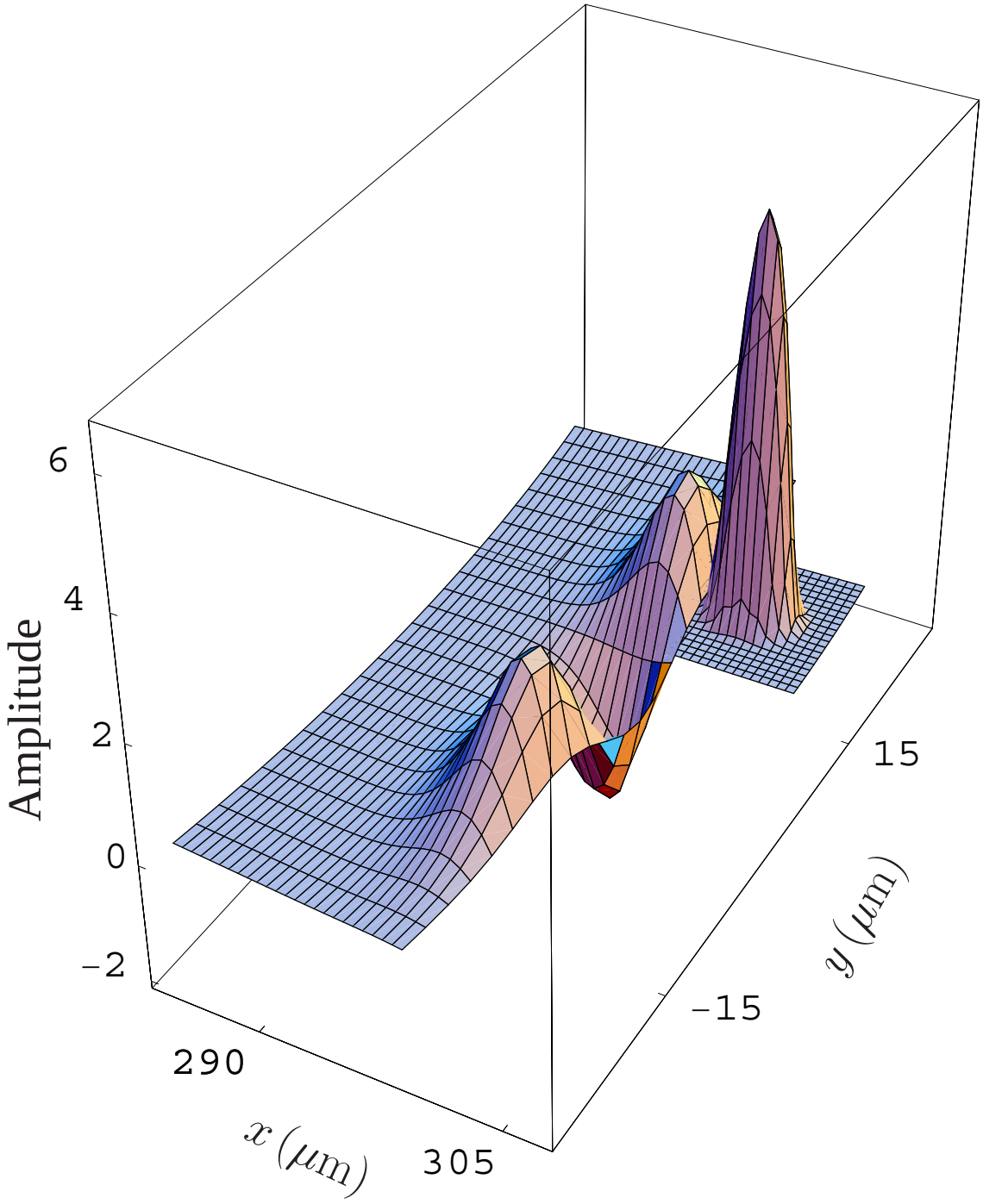

Figure 4.14. Mode Overlap for Offset Fiber. ($R_s = 300\,\mu$m, $R_f = 2.47\,\mu$m, $\lambda = 1550\,$nm, $\varepsilon = 0.29$, $\theta_{\text{off}} = \pi/76$). The WGM shown here is a third order polar mode. The mode's indices are $q = 1$, $l = 1730$, and $m = 1728$.

An example of the results of calculations using Eqs. (3.29) and (4.1) is shown in Fig. 4.15, where the wavelengths are associated with the condition of misalignment of the

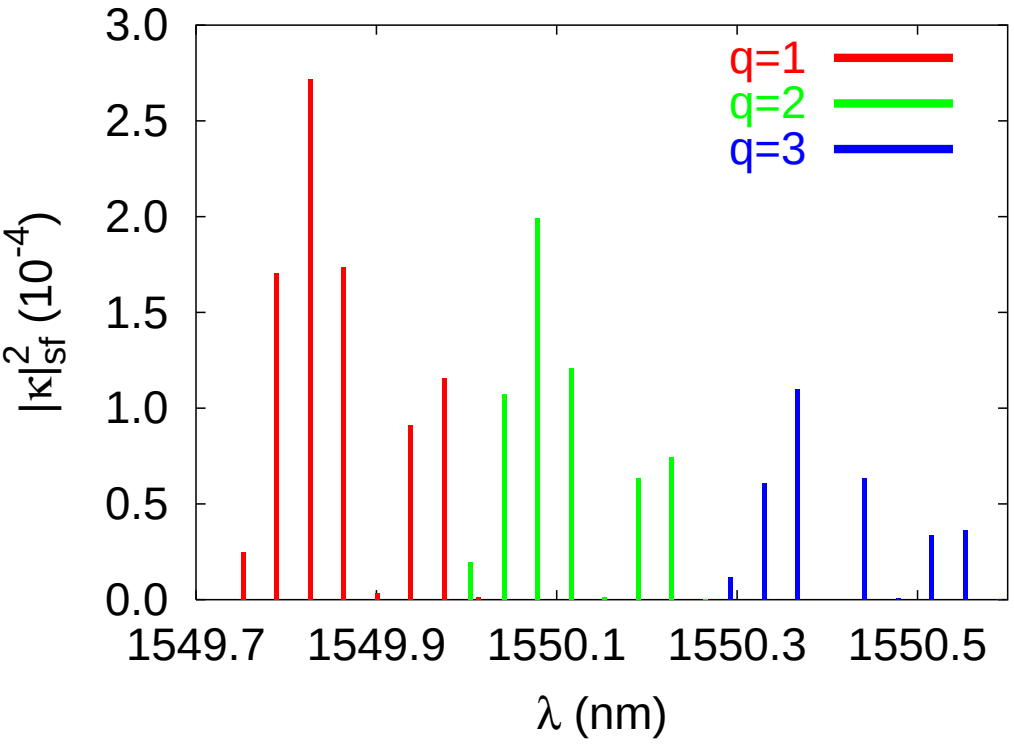

Figure 4.15. WGM TE Spectrum. ($R_s = 300\,\mu$m, $R_f = 2.47\,\mu$m, $\varepsilon = 0.29$, $\theta_{\text{off}} = \pi/76$).

taper modes with the WGMs of the equatorial plane. One free-spectral range of the microsphere is displayed. In this case, the fundamental taper mode has been phase matched to the fundamental microsphere TE mode. The offset from the equatorial plane has been chosen to be $\theta_{\text{off}} = \pi/76$. The different colors indicate modes of different radial order q. Within each color grouping, eight modes are shown, with the polar-mode order increasing from lower to larger wavelength (i.e., $l - |m| = 0, 1, \ldots, 7$). Some of these modes are not visible on the scale of the coupling selected in the figure because of their low coupling coefficients. It is clear that for an offset fiber, higher-order polar modes can have stronger coupling than the fundamental polar mode. In this case the polar modes with $l - |m| = 2$ have the strongest coupling. This is because of the choice of offset. For other offsets, different polar modes have stronger coupling. In the case of no lateral offset, the fundamental

polar modes have the highest coupling. This is followed by weaker coupling for each successive higher-order polar mode. For clarity, only a small fraction of the actual number of modes is shown. Because this graph is over one free-spectral range, modes of higher radial order, if plotted, begin again from the left with $q = 4$. These modes continue to wrap around the plotted wavelength range. Higher-order polar modes overlap with modes of different radial order, if plotted, as well.

The spectrum is different when the fiber radius is chosen to optimally couple the fundamental fiber and microsphere modes. This is shown in Fig. 4.16. As expected, the

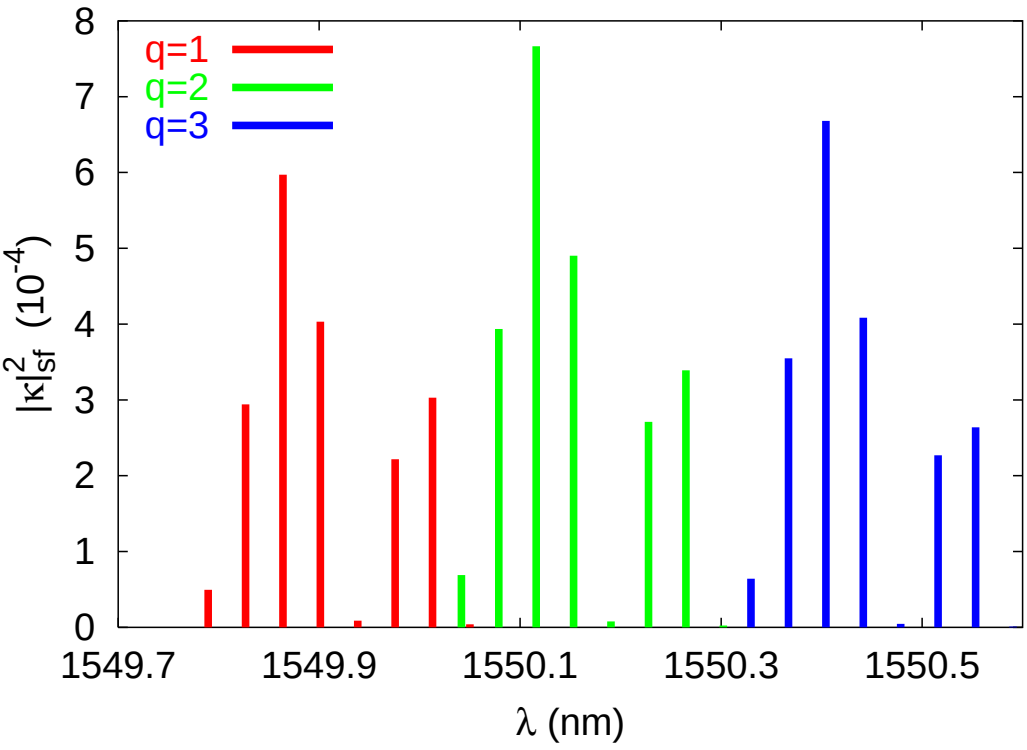

Figure 4.16. WGM TE Spectrum. ($R_s = 300\,\mu$m, $R_f = 1.68\,\mu$m, $\varepsilon = 0.29$, $\theta_{\text{off}} = \pi/76$).

coupling to most modes is stronger. Less expected are that the coupling to higher-order radial modes does not drop off as it does when the fundamental modes are phase matched. The reason for this is that the higher-order radial modes have a higher evanescent fraction. This increases the spatial overlap of the microsphere and fiber fields. The reason that this is not noticeable in Fig. 4.15 is that the phase mismatching between the higher-order microsphere modes and the fiber mode has a stronger effect than the spatial overlap. For the

conditions that produce Fig. 4.16, the spatial overlap has a stronger effect than the phase mismatch. Also, the distribution of the coupling coefficients is different. Although it is more noticeable for $q = 3$, it can be seen also for $q = 1$ and $q = 2$. The reason for this is that the thinner taper for Fig. 4.16 overlaps differently with the extrema of the microsphere mode. The last difference to point out is that within both of these figures the distribution of the polar modes is different for each radial mode order. The reason for this is that for higher radial modes the polar mode distribution is wider. This can be seen from Eq. (2.14b)

$$\psi_\theta(\theta) = H_N\left(\sqrt{m}\theta\right) e^{-\frac{m}{2}\theta^2}, \qquad m \gg 1 \gg \theta.$$

Higher-order radial modes have lower values of l and m. Lower values of m cause the Gaussian part of Eq. (2.14b) to have a wider distribution. For the modes shown here, $l = 1730$ when $q = 1$, $l = 1713$ when $q = 2$, and $l = 1699$ when $q = 3$.

Figure 4.17 shows both the microsphere TE and TM spectra. The distribution of the coupling coefficients are the same except that the TE modes are coupled to more strongly than the TM modes are, as explained in the previous section. Also, there is a shift in the wavelength due to the polarization (see Eq. (2.23).)

In an experiment, the throughput intensity at the end of the fiber is measured. There is a dip in the intensity of the throughput when the frequency is resonant with a WGM. The depth and width of the dip depends on the total quality factor of the mode; this includes the intrinsic Q, which is related to losses due to absorption and scattering, and the external Q, which is related to the coupling loss. The depth of the dip is calculated from

$$d = \frac{4x}{(1+x)^2}, \tag{4.2}$$

where

$$x = \frac{T}{\alpha l}. \tag{4.3}$$

The parameter x is just the ratio of the coupling loss $T = |\kappa|^2$ to the intrinsic loss αl, where l is the circumference of the sphere. The value of x indicates the type of coupling present in the system. If $x > 1$, then the system is overcoupled. If $x < 1$, the system is undercoupled. If $x = 1$, then the intrinsic and external losses balance each other, resulting

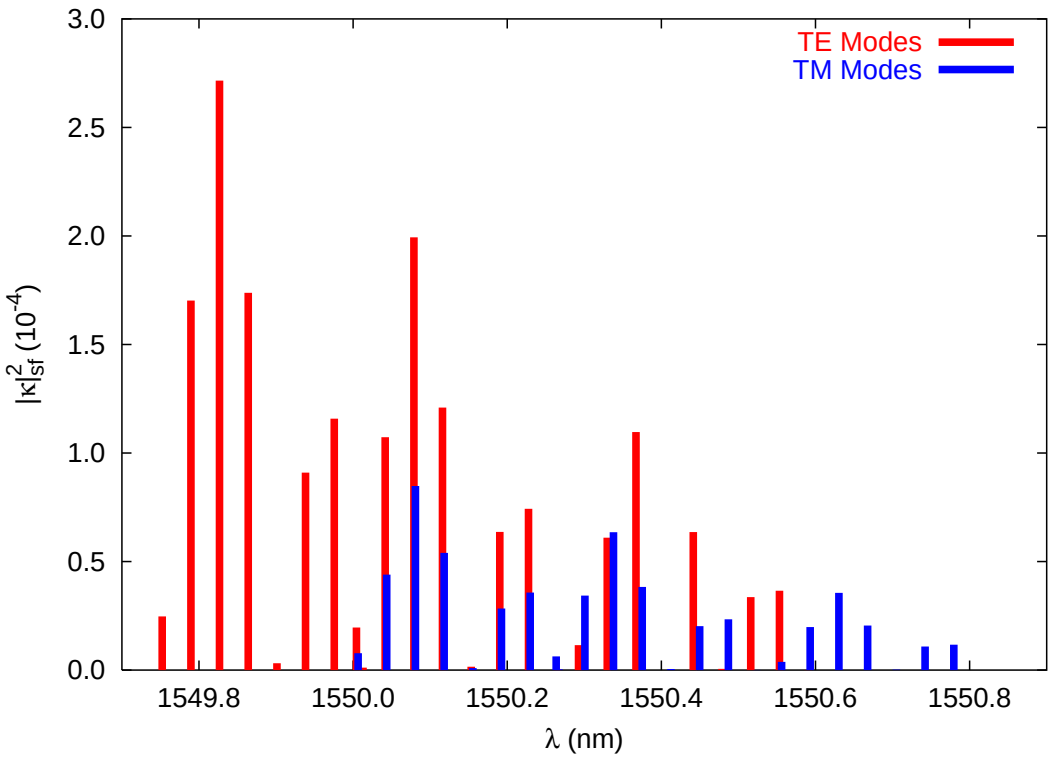

Figure 4.17. WGM TE & TM Spectra. ($R_s = 300\,\mu$m, $R_f = 2.47\,\mu$m, $\varepsilon = 0.29$, $\theta_{\text{off}} = \pi/76$). Here, $l_{\text{TM}} = l_{\text{TE}} - 1$ so that both the TE and TM families of modes will be visible in one free-spectral range.

in critical coupling. For the critically coupled case, the throughput of the system becomes zero, as can be seen from Eq. (4.2). The width $\Delta\lambda$ of a dip is calculated from

$$w \equiv \frac{\Delta\lambda}{2} = \frac{1}{2}\frac{\lambda^2[\alpha l - \ln(1-T)]}{2\pi l n_s} = \frac{1}{2}\frac{\lambda^2[2\pi R_s\alpha - \ln(1-|\tilde{\kappa}_{fs}|^2)]}{4\pi^2 n_s R_s}. \tag{4.4}$$

The spectrum can now be plotted by defining a function f for the throughput of the fiber,

$$f(\lambda) = 1 - \sum_{i=1}^{N} \frac{4x_i}{(1+x_i)^2}\frac{w_i^2}{(\lambda-\lambda_i)^2 + w_i^2}, \tag{4.5}$$

where λ_i is the resonant wavelength of the i^{th} mode and N is the number of modes in the range of the plot. An example of a WGM TE throughput spectrum is shown in Fig. 4.18. In this figure, the intrinsic loss is chosen to be equal to the mean of the coupling losses for all of the modes shown. The high quality factors of the mode are evident from the sharpness of the dips. The line shape is plotted in Fig. 4.19.

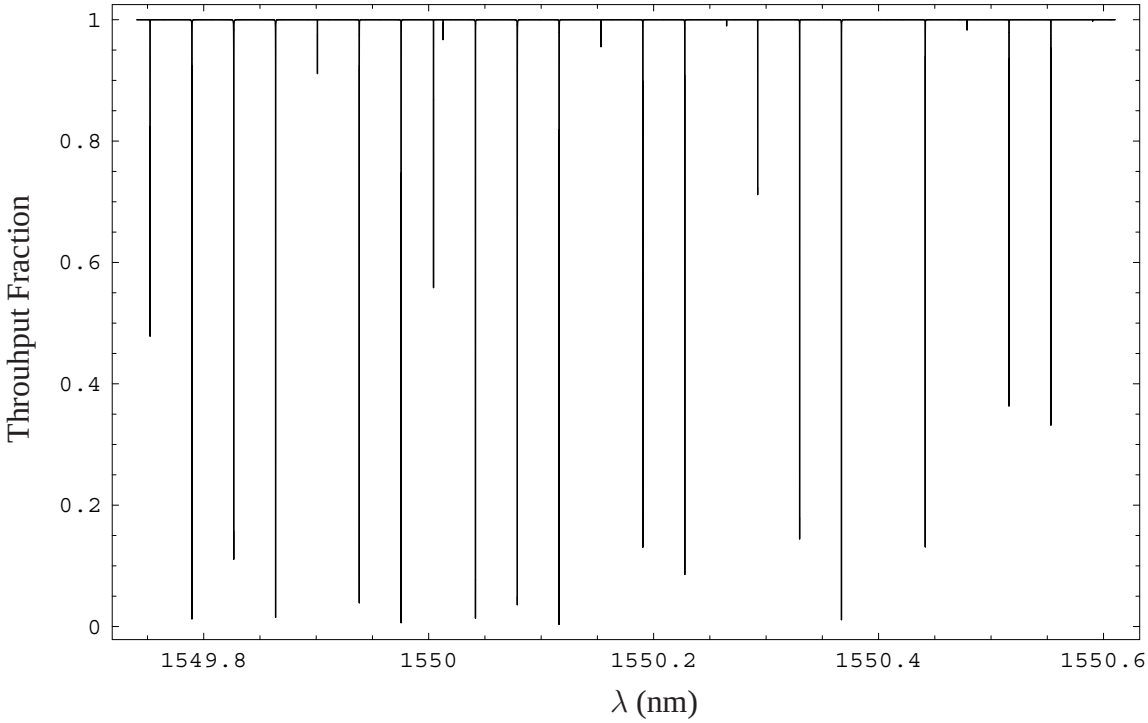

Figure 4.18. WGM TE Throughput Spectrum. ($R_s = 300\,\mu$m, $R_f = 2.47\,\mu$m, $\varepsilon = 0.29$, $\theta_{\text{off}} = \pi/76$).

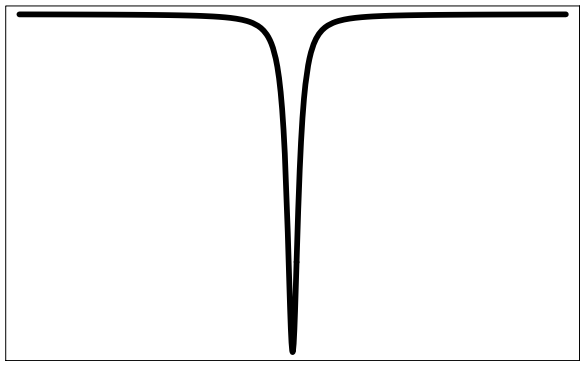

Figure 4.19. WGM Lineshape.

The spectra can be improved even more by including the frequency shift due to the fiber perturbing the microsphere. Without the fiber present, the index of refraction outside of the sphere is just that of air or liquid, depending on the situation. With the fiber present, the microsphere mode sees an effective index that includes the fiber. The value of the effective index is found by averaging the index profile over the evanescent portion of the

microsphere. The expression is

$$n_{o,\text{eff}} = \frac{\iiint\limits_{r>R_s} |\Psi_s(r,\theta,\phi)|^2 \, n_f(r,\theta,\phi) \, r^2 \, \mathrm{d}r \, \mathrm{d}\theta \, \mathrm{d}\phi}{\iiint\limits_{r>R_s} |\Psi_s(r,\theta,\phi)|^2 \, r^2 \, \mathrm{d}r \, \mathrm{d}\theta \, \mathrm{d}\phi}, \tag{4.6}$$

where the integration is performed over the entire region outside of the microsphere. In the actual calculation, the numerator is split into two parts - the total volume and the volume of the fiber. Making use of the step-index profile of the fiber, the numerator becomes

$$\begin{aligned} n_o \iiint\limits_{r>R_s} |\Psi_s(r,\theta,\phi)|^2 \, r^2 \, \mathrm{d}r \, \mathrm{d}\theta \, \mathrm{d}\phi \\ - (n_o - n_f) \iiint\limits_{r<R_f} |\Psi_s(r,\theta,z)|^2 \, r \, \mathrm{d}r \, \mathrm{d}\theta \, \mathrm{d}z, \end{aligned} \tag{4.7}$$

where the second integral is performed in the fiber's coordinate system.

For a microsphere-fiber system with $R_s = 300\,\mu$m, $R_f = 2.47\,\mu$m, $n_s = n_f = 1.44$, $n_o = 1.00$, and the fiber placed in contact with the microsphere exactly at the equator, the effective ambient index is found to be $n_{o,\text{eff}} = 1.0005$ for a fundamental TE mode at $\lambda = 1550\,$nm. This causes the wavelength of the WGM mode to be shifted by only $0.6\,$pm. This is in agreement with experimental measurements.[60]

4.3 Microsphere Lasing

Lasing has been demonstrated in fused silica microspheres in several different systems[39,61–63] including, recently, Raman lasing,[61] using sol-gel coatings,[62] and with HgTe nanoparticle coatings.[63] Modeling the lasing of microspheres is interesting for a couple of reasons. One is that for spheres of experimental interest, there are many possible modes for which emission can occur. This means that the different lasing modes compete for the gain medium. The other reason is that a high fraction of the light spontaneously emitted by particles on the microsphere's surface is captured by a WGM. The effects of these issues on the laser threshold are addressed below.

4.3.1 Mode Competition

Lasing in nanoparticle coated microspheres is achieved by pumping the nanoparticles with light at a wavelength of about 800 nm. This is accomplished by coupling laser light from a tapered fiber into a WGM of the microsphere. The emission is 1550 nm for the numerical example presented here. In general, the threshold condition for a single-mirror ring cavity laser is that the net gain after a single pass be greater than one, or

$$re^{(\gamma_t-\alpha)l} \geq 1, \tag{4.8}$$

where r is the reflection coefficient of the mirror, γ_t is the gain coefficient, and α is the absorption coefficient. Solving for the gain results in

$$\gamma_t = \alpha - \frac{1}{l}\ln(r). \tag{4.9}$$

In the case of the microsphere this is

$$\begin{aligned}\gamma_t &= \alpha - \frac{1}{2\pi R_s n_s}\ln\left[\left(1-|\tilde{\kappa}_{fs}|^2\right)^{1/2}\right] \\ &= \alpha - \frac{1}{4\pi R_s n_s}\ln\left[1-|\tilde{\kappa}_{fs}|^2\right].\end{aligned} \tag{4.10}$$

Equation (4.10) can be converted to find the the threshold condition for the inversion density. It is found to be proportional to the gain, or

$$\Delta N_t \propto \alpha - \frac{1}{4\pi R_s n_s}\ln\left[1-|\tilde{\kappa}_{fs}|^2\right]. \tag{4.11}$$

Because the different WGMs have different coupling coefficients with the fiber, each WGM has a different threshold for the inversion density. This means that as the pump power increases, the output at the emission wavelength does not exhibit an abrupt turn on, but a gradual one as the different modes begin to lase. This isn't a complete picture, however, because the lasing modes compete for the gain medium.

The reason why lasing modes compete for gain medium is that the medium can become saturated. In this analysis, the gain medium is assumed to be homogeneously broadened. This means that there are cross-saturation effects between the different modes. For inhomogeneously broadened media, the frequency difference between the modes would

prevent cross-saturation between the different lasing modes. Although there are many different modes that can lase, this system can be analyzed by considering two-mode competition and expanding to many modes.

The competition of two lasing modes can be analyzed by studying the stability of the rate equations.[64–66] The rate equations for two competing modes in the conventional notation are

$$\frac{\mathrm{d}I_1}{\mathrm{d}t} = (\alpha_1 - \beta_1 I_1 - \theta_{12} I_2) \times I_1, \tag{4.12a}$$

$$\frac{\mathrm{d}I_2}{\mathrm{d}t} = (\alpha_2 - \beta_2 I_2 - \theta_{21} I_1) \times I_2, \tag{4.12b}$$

where the I's are the intensity of the modes, the α's are the unsaturated gains minus losses, the β's are the self-saturation coefficients, and the θ's are the cross-saturation coefficients. Because this notation can be confusing for the fiber-microsphere system, a few changes are made. The unsaturated gains minus losses are proportional to the self-saturation coefficients, so both are replaced by a factor F. The calculation of the cross-saturation coefficients is similar to that of the coupling coefficients, so the symbol is changed to κ. In this notation, the rate equations become

$$\frac{\mathrm{d}I^{(1)}}{\mathrm{d}t} = \left(F^{(1)} - F^{(1)} I^{(1)} - \kappa^{(1,2)} I^{(2)}\right) \times I^{(1)}, \tag{4.13a}$$

$$\frac{\mathrm{d}I^{(2)}}{\mathrm{d}t} = \left(F^{(2)} - F^{(2)} I^{(2)} - \kappa^{(2,1)} I^{(1)}\right) \times I^{(2)}, \tag{4.13b}$$

where $I^{(i)}$ and $F^{(i)}$ are the intensity and self-saturation coefficients of the i^{th} mode, respectively. $\kappa^{(i,j)}$ are the cross-saturation coefficients between the i^{th} and j^{th} modes. For steady-state solutions, either the intensity has to be zero or the saturated gain must be zero, or

$$I^{(1)} = 1 - \left(\frac{\kappa^{(1,2)}}{F^{(1)}}\right) I^{(2)}, \tag{4.14a}$$

$$I^{(2)} = 1 - \left(\frac{\kappa^{(2,1)}}{F^{(2)}}\right) I^{(1)}. \tag{4.14b}$$

If the solutions of Eq. (4.14) do not intersect, then only one of the modes lases. If the solutions do intersect, then both modes can lase simultaneously. In this case, the saturated

gains of the modes are given by

$$F_s^{(1)} = \frac{F^{(1)}}{1 + F^{(1)} I^{(1)} + \kappa^{(1,2)} I^{(2)}}, \tag{4.15a}$$

$$F_s^{(2)} = \frac{F^{(2)}}{1 + F^{(2)} I^{(2)} + \kappa^{(2,1)} I^{(1)}}. \tag{4.15b}$$

The intent of this model is to get a qualitative, rather than a quantitative demonstration of the threshold behavior of a microsphere laser. The unsaturated gain and the self-saturation coefficient of a given lasing mode are found by calculating the overlap between the pump mode and the lasing mode. For simplicity, only the polar dependences of the modes are considered. The value is then

$$F^{(i)} = \sqrt{\int \left| \psi_\theta^{(p)}(\theta) \psi_\theta^{(i)}(\theta) \right| \, \mathrm{d}\theta}, \tag{4.16}$$

where $\psi_\theta^{(p)}(\theta)$ and $\psi_\theta^{(i)}(\theta)$ are the polar dependences of the pump mode and the i^{th} lasing mode, respectively. This is different from the overlap integral used to calculate the coupling coefficients because it integrates over magnitude. In the case of field coupling, sign effects can prevent two modes from coupling if their symmetries conflict. In the case of optical pumping, the signs of the fields do not determine whether the nanoparticles are excited. To determine the cross-saturation coefficients, it is useful to define the integrand of Eq. (4.16) as a separate function

$$\psi_\theta^{(p,i)}(\theta) = K^{(p,i)} \psi_\theta^{(p)}(\theta) \psi_\theta^{(i)}(\theta), \tag{4.17}$$

where $K^{(p,i)}$ is a normalization factor. The cross-saturation coefficients are now

$$\kappa^{(i,j)} = \sqrt{F^{(i)} F^{(j)} \int \left| \psi_\theta^{(p,i)}(\theta) \psi_\theta^{(p,j)}(\theta) \right| \, \mathrm{d}\theta}. \tag{4.18}$$

The power in the i^{th} mode as a function of the pump photon density N_0 is given by

$$\begin{aligned} P^{(i)}(N_0) = {} & \frac{F^{(i)} N_0}{N_t^{(i)}} \left(1 - \mathsf{UnitStep}\left[F^{(i)} N_0 - N_t^{(i)} \right] \right) \\ & + \left(10^6 \mathsf{MdSel}[i] \left(F^{(i)} N_0 - N_t^{(i)} \right) \left(\frac{1}{1 + 0.01 \sum_{j=1}^{24} \kappa^{(i,j)} P^{(j)}} \right) + 1 \right) \\ & \quad * \mathsf{UnitStep}[F^{(i)} N_0 - N_t^{(i)}], \end{aligned} \tag{4.19}$$

where the computer functions UnitStep and MdSel are used to turn the lasing on and off. UnitStep is just the normal step function in *Mathematica*. The user-written function MdSel is a function of the pump power and is determined from the stability analysis. It is equal to unity when no other lasing mode cuts it off and is equal to zero when any of the other lasing modes cut it off. The factor of 10^6 is the ratio of the slope of the mode power when the mode is lasing compared to when it is not. The factor of 0.01 determines the amount of saturation of the gain medium. The total power in the laser is found from the superposition of all of the modes,

$$P^{\text{tot}}(N_0) = \sum_{i=1}^{24} P^{(i)}(N_0). \tag{4.20}$$

A demonstration of multimode lasing is shown in Fig. 4.20. The different colors refer to pump modes of different polar order $N = l - |m|$. The lasing modes are taken from the spectrum of Fig. 4.15. It is clear from Fig. 4.20 that mode competition can result in nonlinear threshold behavior. The difference between the lasing with different pump modes can be explained by the confinement of the pump modes. The fundamental polar mode $N = 0$ has the tightest confinement. This enables the threshold to be lower than when using a higher-order pump mode. Using a higher-order pump mode does have a different advantage, however. The higher-order pump mode, being more spread out spatially, is able to activate more lasing modes with less saturation. This is seen in the crossing of the laser output curves for the different modes $N = 0$, $N = 3$, and $N = 6$.

4.3.2 Spontaneous Emission Capture Fraction

Experiments[39–41,61–63] indicate that the threshold of microsphere lasers can be very low. This indicates that a high fraction of the spontaneous emission is captured by a lasing WGM. This fraction is calculated[67] for a single quantum dot placed near the surface of a sphere using a generalized Lorentz-Mie scattering theory.[33] Using this method for calculating the capture fraction of spontaneous emission, it is found that a high capture fraction is expected.[67] Furthermore, it is found that the emission pattern of a dipole placed on the surface of a dielectric is pulled into the medium of higher refractive index.[68] A topic of current and future research is to better understand and quantify the amount of spontaneous

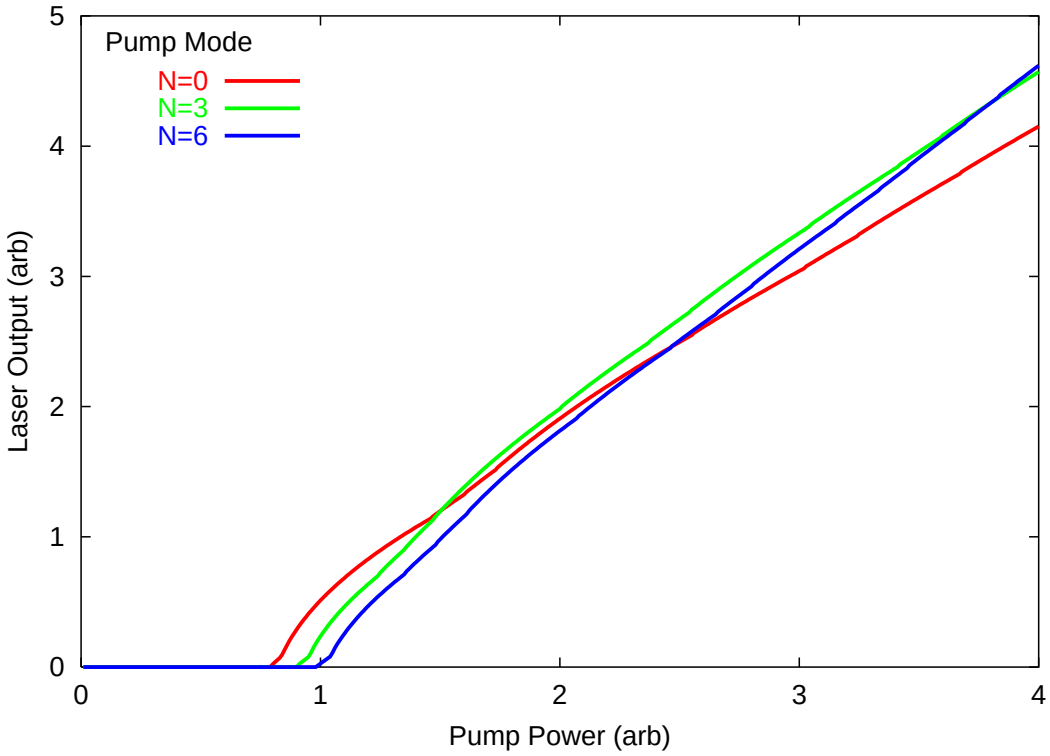

Figure 4.20. Laser Threshold. ($R_s = 300\,\mu$m, $R_f = 2.47\,\mu$m, $\varepsilon = 0.29$, $\theta_{\text{off}} = \pi/76$). The different colors refer to pump modes of different polar order $N = l - |m|$.

emission captured by a WGM for a microsphere under conditions used in lasing experiments where HgTe nanoparticle coatings are used.

CHAPTER 5

CONCLUSIONS AND PERSPECTIVES

Coupled-mode theory is used to calculate the coupling between modes of a tapered fiber and whispering-gallery modes of a fused-silica microsphere. The two important factors that determine the amount of coupling are the spatial overlap of the fields and the phase matching between them. These coupling coefficients are calculated by numerically evaluating the field overlap integrals where the interference due to phase mismatch is included. The method is applied to determine the optimal taper radius for coupling to a microsphere and to calculate WGM spectra that include non-ideal conditions so that they can be compared directly to experiment. The calculated spectra are then used to model multimode lasing in a microsphere.

The calculations of optimal fiber radii indicate that the highest coupling from a fundamental taper mode to a microsphere mode is achieved with a fiber that has a radius about 30% smaller than for perfect phase matching. For these fiber sizes, the coupling is about twice as strong as for the phase-matched condition. This is not the traditionally held belief, however. Common reasoning led to the belief that the effect of phase-mismatch prevents significant coupling between two modes. The reason that this is not correct is that this argument does not consider the changes in spatial overlap of the fields when the fiber radius is altered from the phase-matched radius. The numerical calculations in this study show that for tapers smaller than for phase matching there are two regimes of behavior. In one regime, the spatial overlap has a larger effect than the phase-mismatch. In the other regime, the phase-mismatch has a larger effect than the spatial overlap. An additional advantage of using the smaller taper radii is that losses to higher-order fiber modes are substantial for phase-matched taper radii. Calculations also show that changing from TE to TM microsphere modes does not change the overall conclusion. However, the calculations indicate

that coupling to the microsphere TE modes is stronger than to the TM modes. This is a result of the longitudinal field overlap present when coupling into TM modes. The contribution of the longitudinal field overlap opposes the contribution of the transverse field overlap.

The calculation of WGM spectra shows that there are many possible modes that can be coupled within one free-spectral range of the microsphere. The calculated values of the coupling coefficients are consistent with experimental data.[60] With the fiber taper laterally offset from, but still parallel to the equatorial plane of the microsphere, the coupling to the fundamental polar mode is not as strong as to some of the higher-order polar modes. This is in agreement with experimental data and is a result of higher-order polar modes having more polar extent. The inclusion of eccentricity and lateral offset enables the numerical calculations to be directly compared to experiment. These calculations are then valuable both for designing experiments and interpreting the resulting data. In particular, WGM spectra can be used to model multimode lasing in a microsphere.

The lasing model presented here allows for lasing of multiple modes. Each lasing mode has a different threshold value. One reason for this is that the different lasing modes have different coupling coefficients, taken from the calculation of WGM spectra. This means that the quality factor may not be the same for all modes. The other is that each lasing mode has a different amount of spatial overlap with the pump mode. In addition to each mode having a different threshold, the lasing modes compete for the gain media. This is taken into account by using two-mode stability analysis and applying it to all pairs of modes. The results of this model are that the threshold behavior is nonlinear, as modes are activated and then cut off by other modes. The model indicates that the lowest threshold is attained when using a pump mode of fundamental polar order. This is because of the narrow confinement of the mode along the equator of the microsphere. The highest laser output is found when pumping with a higher-order polar mode. This is because the larger spatial distribution of the pump mode allows more modes to lase with less saturation.

In the process of performing this research several topics in basic physics have come to the surface. One is that the wave nature of light dominates on the size scales used here. This means that the behavior of the fiber-microsphere system is different from that

of a cavity that can be described by classical ray optics. The most obvious difference is in the fact that light can actually couple between the fiber and microsphere. In the ray picture the light stays in the waveguide unless the angle of incidence of a ray is to hit the surface at an angle less than the critical angle. The coupling of light is a tunneling process that violates Snell's Law. This is analogous to a particle tunneling out of a potential well in quantum mechanics. Even so, with a taper-coupled microsphere the term "frustrated total internal reflection" is barely applicable if used to describe the coupling phenomenon. In prism-coupled microspheres, the light ray is actually directed toward the microsphere. In this case, there is a small probability that a photon tunnels across the refractive index barrier between the prism and microsphere. In fiber-coupled microspheres, the situation is different. In a taper, the light does not actually travel by bouncing in a zig-zag path within the fiber. The light travels straight down the fiber, with most of the light contained in the taper and a small portion of it in the taper's surroundings. The spatial distribution of the modes does not change along the direction of propagation. The same is true for whispering-gallery modes in a microsphere. This means that in the coupling region light in the fiber and the microsphere are actually going in the same direction. Thus, the coupling occurs perpendicular to the direction of propagation. One effect of this is that, unlike in the case of a classical resonator, a photon that tunnels from one waveguide to another may tunnel back into the first waveguide within the interaction region.

Another aspect of coupling between a fiber and a microsphere is that the coupling coefficients are not the same for FMC and MFC unless the propagation constants of the two modes are identical. This raises questions about the intracavity intensity and energy conservation. Both of these questions are resolved by the fact that tunneling is perpendicular to the direction of propagation. The intracavity intensity as calculated in a classical resonator but with directionally dependent transmission coefficients is not equal to the intensity as calculated with coupled-mode theory. This is because of the fact that a photon that tunnels from one waveguide to another may tunnel back into the first waveguide within the interaction region. The question about energy conservation lies in how the power flow remains a constant and how time reversal is not violated when the coupling coefficients are unequal ($\kappa_{sf} \neq \kappa_{fs}$). Again, this is not a problem because the tunneling is not in the

direction of propagation. In fact, the difference in coupling coefficients is necessary when the propagation constants are unequal.

The results of this study lead to new research pursuits. As was mentioned in the applications chapter, calculations of the capture fraction of the spontaneous emission of a dipole on the surface of a microsphere by a WGM will greatly improve the understanding of microsphere lasing. Also, this research is being extended to the coupling between two microspheres for application to coupled-resonator induced transparency (CRIT) and absorption (CRIA) theory[69] and experiments.[70] These phenomena are seen by coupling a second microsphere to a microsphere that is already coupled to a tapered fiber. The realization of CRIT and CRIA is strongly dependent on the fiber-microsphere coupling and the microsphere-microsphere coupling. Adding data from microsphere-microsphere coupling to the data already calculated in this study will greatly facilitate coupled-resonator research.

BIBLIOGRAPHY

[1] J. Strutt (Lord Rayleigh), *The theory of sound*, (London: Mcmillan, 1894-96), Vol. 2.

[2] G. Mie, "Contributions to the Optics of Turbid Media, Especially Colloidal Metal Solutions." Ann. Phys. **25**, 377–445 (1908).

[3] P. Debye, "*Der Lichtdruck auf Kugeln von beliebigem Material*," Ann. Phys. **30**, 57–136 (1909).

[4] R. D. Richtmyer, "Dielectric Resonators," J. Appl. Phys. **10**, 391–398 (1939).

[5] J. A. Stratton, *Electromagnetic Theory*, (New York: McGraw-Hill, 1941), pp. 554–558.

[6] L. A. Vainstein, *Open Resonators and Open Waveguides* (Sovetskoe Radio, Moscow, 1964), [L. A. Vainstein, *Open Resonators and Open Waveguides*, (Golem Press, Boulder, CO, 1969)].

[7] V. B. Braginsky and V. S. Ilchenko, "Properties of optical dielectric microresonators," Dokl. Akad. Nauk SSSR **293**, 1358 (1987), [Sov. Phys. Dokl. **32**, 306 (1987)].

[8] V. B. Braginsky, M. L. Gorodetsky, and V. S. Ilchenko, "Quality factor and nonlinear properties of optical whispering-gallery modes," Phys. Lett. A **137**, 393–397.

[9] M. L. Gorodetsky and V. S. Ilchenko, "High-Q optical whispering-gallery microresonators: precession approach for spherical mode analysis and emission patterns with prism," Opt. Commun. **113**, 133–143 (1994).

[10] A. N. Oraevsky and D. K. Bandy, "Semiconductor microballs as bistable optical elements," Opt. Commun. **129**, 75–80 (1996).

[11] V. V. Klimov, M. Ducloy, and V. S. Letokhov, "Vaccum Rabi splitting of an atom dipole near a dielectric microsphere," J. Mod. Opt. **44**, 1081–1092 (1997).

[12] V. V. Vasiliev, V. L. Velichansky, M. L. Gorodetsky, V. S. Ilchenko, L. Hollberg, A. V. Yarovitsky, "High-Coherence Diode Laser with Optical Feedback via a Microcavity with 'Whispering Gallery' Modes," Kvantovaya Elektron. **23**, 675 (1996), [Quantum Electron. **26**, 657–658 (1996)].

[13] V. V. Vasiliev, V. L. Velichansky, V. S. Ilchenko, M. L. Gorodetsky, L. Hollberg, and A. V. Yarovitsky, "Narrow-line-width diode laser with a high-Q microsphere resonator," Opt. Commun. **158**, 182–187 (1998).

[14] L. A. Katomtseva and G. P. Lednyeva, in *Diffractive Optics and Optical Microsystems*, Martellucci and Chester, eds., (Plenum Press, New York, 1997), pp. 83–89.

[15] J. C. Knight, N. Dubreuil, V. Sandoghdar, J. Hare, V. Lefèvre-Seguin, J. M. Raimond, and S. Haroche, "Mapping whispering-gallery modes in microspheres with a near-field probe," Opt. Lett. **20**, 1515–1517 (1995).

[16] J. C. Knight, N. Dubreuil, V. Sandoghdar, J. Hare, V. Lefèvre-Seguin, J. M. Raimond, and S. Haroche, "Characterizing whispering-gallery modes in microspheres by direct observation of the optical standing-wave pattern in the near field," Opt. Lett. **21**, 698–700 (1996).

[17] N. Dubreuil, J. C. Knight, D. K. Leventhal, V. Sandoghdar, J. Hare, and V. Lefèvre, "Eroded monomode optical fiber for whispering-gallery mode excitation in fused-silica microspheres," Opt. Lett. **20**, 813–815 (1995).

[18] D. W. Vernooy, A. Furusawa, N. P. Georgiades, V. S. Ilchenko, and H. J. Kimble, "Cavity QED with high-Q whispering gallery modes," Phys. Rev. A **57**, R2293–R2296 (1998).

[19] J.-Z. Zhang, D. H. Leach, and R. K. Chang, "Photon lifetime within droplet: temporal determination of elastic and stimulated Raman Scattering," Opt. Lett. **13**, 270–272 (1988).

[20] G. S. Agarwal and S. Dutta Gupta, "Spherical microstructures for the study of strong coupling between radiation and matter," Opt. Commun. **93**, 173–178 (1992).

[21] *Optical Effects Associated with Small Particles*, P. W. Barber and R. K. Chang, eds., (World Scientific, Singapore, 1988).

[22] D. Braunstein, A. M. Khazanov, G. A. Koganov, and R. Shuker, "Lowering of threshold conditions for nonlinear effects in a microsphere," Phys. Rev. A **53**, 3565–3572 (1996).

[23] A. T. Rosenberger, "Nonlinear Optical Effects in the Whispering-Gallery Modes of Microspheres," in *Operational Characteristics and Crystal Growth of Nonlinear Optical Materials*, R. B. Lal and D. O. Frazier, eds., Proc. SPIE **3793**, 179–186 (1999).

[24] A. T. Rosenberger and J. P. Rezac, "Evanescent-wave sensor using microsphere whispering-gallery modes," in *Laser Resonators III*, A. V. Kudryashov and A. H. Paxton, eds., Proc. SPIE **3930**, 186–192 (2000).

[25] A. N. Oraevsky, M. O. Scully, and V. L. Velichansky, "Quantum dot laser," Kvantovaya Elektron. (1998), [Quantum Electron. **28**, 203–208 (1998)].

[26] S. L. McCall, A. F. J. Levi, R. E. Sluster, S. J. Pearton, and R. A. Logan, "Whispering-gallery mode microdisk lasers," Appl. Phys. Lett. **60**, 289–291 (1992).

[27] A. Eschmann and C. W. Gardiner, "Stability and switching in whispering-gallery-mode microdisk lasers," Phys. Rev. A **49**, 2907–2913 (1994).

[28] H. Chew, D.-S. Wang, and M. Kerker, "Elastic scattering of evanescent electromagnetic waves," Opt. Commun. **18**, 2670–2686 (1979).

[29] A. V. Zvyagin and K. Goto, "Mie scattering of evanescent waves by a dielectric sphere: comparison of multipole expansion and group-theory methods," J. Opt. Soc. Am. A, **15**, 3003–3008 (1998).

[30] M. L. Gorodetsky and V. S. Ilchenko, "Optical microsphere resonators: optimal coupling to high-Q whispering-gallery modes," J. Opt. Soc. Am. B **16**, 147–154 (1999).

[31] H. Ishikava, H. Tamaru, and K. Miyano, "Microsphere resonators strongly coupled to a plane dielectric substrate: coupling via the optical near field," J. Opt. Soc. Am. A **17**, 802–813 (2000).

[32] B. E. Little, J.-P. Laine, and H. A. Haus, "Analytic theory of coupling from tapered fibers and half-blocks into microsphere resonators," J. Lightwave Technol. **17**, 704–715 (1999).

[33] J. P. Barton, D. R. Alexander, and S. A. Schuab, "Internal and near-surface electromagnetic fields for a spherical particle irradiated by a focused laser beam," J. Appl. Phys. **64**, 1632–1639 (1988).

[34] G. Gouesbet, B. Maheu, and G. Grehan, "Light scattering from a sphere arbitrarily located in Gaussian beam, using Bromwich formulation," J. Opt. Soc. Am. A **5**, 1427–1443 (1988)

[35] J. A. Lock, "Excitation efficiency of a morphology-dependent resonance by focused Gaussian beam," J. Opt. Soc. Am. A **15**, 2986–2994 (1998).

[36] C. Lu, T. Kaiser, S. Lange, and G. Schweiger, "Structural resonances in a dielectric sphere illuminated by an evanescent wave," Opt. Commun. **117**, 521–531 (1995).

[37] D. W. Vernooy, V. S. Ilchenko, H. Mabuchi, E. W. Streed, and H. J. Kimble, "High-Q measurements of fused-silica microspheres in the near infrared," Opt. Lett. **23**, 247–249 (1998).

[38] T. Baer, "Continuous-wave laser oscillation in Nd:YAG sphere," Opt. Lett. **12**, 392–394 (1987).

[39] V. Sandoghdar, F. Treussart, J. Hare, V. Lefèvre-Seguin, J.-M. Raimond, and S. Haroche, "Very low threshold whispering-gallery-mode microsphere laser," Phys. Rev. A **54**, 1777–1780 (1996).

[40] M. Cai, O. Painter, K. J. Vahala, and P. C. Sercel, "Fiber-coupled microsphere laser," Opt. Lett. **25**, 1430–1432 (2000).

[41] F. Lissillour, P. Féron, N. Dubrieuil, P. Dupriez, M. Poulain, and G. M. Stéphan, "Erbium-doped microspherical lasers at 1.56 μm," Electron. Lett. **36**, 1382–1384 (2000).

[42] A. T. Rosenberger and J. P. Rezac, "Whispering-gallery-mode evanescent-wave microsensor for trace-gas detection," in *Biomedical Instrumentation Based on Micro- and Nanotechnology*, R. P. Mariella, Jr. and D. V. Nicolau, eds., Proc. SPIE **4265**, 102–112 (2001).

[43] V. S. Ilchenko, P. S. Volikov, V. L. Velichansky, F. Treussart, V. Lefèvre-Seguin, J.-M. Raimond, and S. Haroche, "Strain-tunable high-Q optical microsphere resonator," Opt. Commun. **145**, 86–90 (1998).

[44] J. P. Rezac and A. T. Rosenberger, "Locking and laser-frequency tracking of a microsphere whispering-gallery mode," in *Laser Resonators IV*, A. V. Kudryashov and A. H. Paxton, eds., Proc. SPIE **4270**, 112–119 (2001).

[45] J. P. Rezac and A. T. Rosenberger, "Locking a microsphere whispering-gallery mode to a laser," Opt. Express **8**, 605–610 (2001).

[46] J. C. Knight, G. Cheung, F. Jacques, and T. A. Birks, "Phased-matched excitation of whispering-gallery mode resonances by a fiber taper," Opt. Lett. **25**, 1129–1131 (1997).

[47] S. M. Spillane, T. J. Kippenberg, O. J. Painter, and K. J. Vahala, "Ideality in a fiber-taper-coupled microresonator system for application to cavity quantum electrodynamics," Phys. Rev. Lett. **91**, 043902 (2003).

[48] E. E. Nariminov, "Light in Asymmetric Resonators: Chaos, Tunneling and Localization," in *Digest of the LEOS Summer Topical Meetings* (2004).

[49] L. A. Vainstein, *Elektromagnitnye volny* (Electromagnetic Waves), (Moscow: Sovetskoe Radio, 1957).

[50] A. N. Oraevsky, "Whispering-gallery waves," Kvantovaya Elektron. (2002), [Quantum Electronics **32**, 377–400 (2002)].

[51] S. Schiller and R. L. Byer, "High-resolution spectroscopy of whispering gallery modes in large dielectric spheres," Opt. Lett. **16**, 1138–1140 (1991).

[52] A. Yariv, *Optical Electronics*, (CBS College Publishing, 1985), Ch. 3.

[53] M. S. Dinleyici and D. B. Patterson, "Vector modal solution of evanescent coupler," J. Lightwave Technol. **LT-15**, 2316–2324 (1997).

[54] S.-L. Chuang, "A coupled mode formulation by reciprocity and a variational principle," J. Lightwave Technol. **LT-5**, 5–15 (1987).

[55] A. W. Snyder and J. D. Love, *Optical Waveguide Theory*, (Massachusetts: Kluwer Academic Publishers, 1983), Ch. 31.

[56] A. Hardy and W. Streifer, "Coupled Mode Theory of Parallel Waveguides," J. Lightwave Technol. **LT-3**, 1135–1142 (1985).

[57] A. T. Rosenberger, Department of Physics, Oklahoma State University, 145 Physical Sciences, Stillwater, OK 74078-3072 (personal communication, 2004).

[58] J. D. Love, *et al.*, "Tapered single-mode fibres and devices - Part 1: Adiabaticity criteria", *IEE Proceedings-J* **138**, 343–354 (1991).

[59] J. D. Love, *et al.*, "Tapered single-mode fibres and devices - Part 2: Experimental and theoretical quantification", *IEE Proceedings-J* **138**, 355–364 (1991).

[60] J. Rezac, *Properties and Applications of Whispering-Gallery Mode Resonances in Fused Silica Microspheres*, Ph.D. thesis, Oklahoma State University (2002).

[61] S. M. Spillane, T. J. Kippenberg, and K. J. Vahala, "Ultralow-threshold Raman laser using a spherical dielectric microcavity," Nature **415**, 621–623 (2002).

[62] L. Yang and K. J. Vahala, "Gain functionalization of silica microresonators," Opt. Lett. **28**, 592–594 (2003).

[63] S. I. Shopova, G. Farca, A. T. Rosenberger, W. M. S. Wickramanayake, and N. A. Kotov, "Microsphere whispering-gallery-mode laser using HgTe quantum dots," (Submitted, 2004).

[64] A. E. Siegman, *Lasers*, (University Science Books, 1986), pp. 992–1003.

[65] W. E. Lamb, Jr., "Theory of an optical maser," Phys. Rev. A **134**, 1429–1450 (1964).

[66] M. Sargent III, M. O. Scully, and W. E. Lamb, Jr., *Laser Physics*, (Addison-Wesley, 1974) Ch. 9–12.

[67] M. Pelton and Y. Yamamoto, "Ultralow threshold laser using a single quantum dot and a microsphere cavity," Phys. Rev. A **59**, 2418–2421 (1999).

[68] J.-Y. Courtois, J.-M. Courty, and J. C. Mertz, "Internal dynamics of multilevel atoms near a vacuum-dielectric interface," Phys. Rev. A **53**, 1862–1878 (1996).

[69] D. D. Smith, H. Chang, K. A. Fuller, A. T. Rosenberger, and R. W. Boyd, "Coupled-resonator-induced transparency," Phys. Rev. A **69**, 063804 (2004).

[70] A. Naweed, Department of Physics, Oklahoma State University, 145 Physical Sciences, Stillwater, OK 74078-3072 (personal communication, 2004).

APPENDICES

APPENDIX A

STEP-INDEX FIBER MODES

The fields of step-index fiber modes are calculated by solving the wave equation in cylindrical coordinates. Step-index fibers have the index profile

$$n(r) = \begin{cases} n_1, & \text{for} \quad r < R_f, \\ n_2, & \text{for} \quad r > R_f, \end{cases} \tag{A.1}$$

where R_f is the radius of the core. The following development closely follows that of Yariv.[52] The direction of propagation is taken to be the z-direction. The wave equation in the longitudinal direction is

$$\left(\nabla^2 + k^2\right) \begin{pmatrix} E_z \\ H_z \end{pmatrix} = 0, \tag{A.2}$$

where

$$\nabla^2 = \frac{\partial^2}{\partial r^2} + \frac{1}{r}\frac{\partial}{\partial r} + \frac{1}{r^2}\frac{\partial^2}{\partial \theta^2} + \frac{\partial^2}{\partial z^2}. \tag{A.3}$$

The solutions are assumed to have the harmonic form,

$$\begin{pmatrix} \mathbf{E}(\mathbf{r}, t) \\ \mathbf{H}(\mathbf{r}, t) \end{pmatrix} = \begin{pmatrix} \mathbf{E}(r, \theta) \\ \mathbf{H}(r, \theta) \end{pmatrix} e^{i(\omega t - \beta z)}. \tag{A.4}$$

The Maxwell equations can then be expressed as

$$E_r = \frac{-i\beta}{\omega^2\mu\epsilon - \beta^2}\left(\frac{\partial}{\partial r}E_z + \frac{\omega\mu}{\beta}\frac{\partial}{r\partial\theta}H_z\right), \tag{A.5a}$$

$$E_\theta = \frac{-i\beta}{\omega^2\mu\epsilon - \beta^2}\left(\frac{\partial}{r\partial\theta}E_z - \frac{\omega\mu}{\beta}\frac{\partial}{\partial r}H_z\right), \tag{A.5b}$$

$$H_r = \frac{-i\beta}{\omega^2\mu\epsilon - \beta^2}\left(\frac{\partial}{\partial r}H_z - \frac{\omega\epsilon}{\beta}\frac{\partial}{r\partial\theta}E_z\right), \tag{A.5c}$$

$$H_\theta = \frac{-i\beta}{\omega^2\mu\epsilon - \beta^2}\left(\frac{\partial}{r\partial\theta}H_z + \frac{\omega\epsilon}{\beta}\frac{\partial}{\partial r}E_z\right). \tag{A.5d}$$

The wave equation in the longitudinal direction is now

$$\left(\frac{\partial^2}{\partial r^2}+\frac{1}{r}\frac{\partial}{\partial r}+\frac{1}{r^2}\frac{\partial^2}{\partial\theta^2}+\left(k^2-\beta^2\right)\right)\begin{pmatrix}E_z\\H_z\end{pmatrix}=0. \tag{A.6}$$

The solutions of the separable equation take the form ,

$$\begin{pmatrix}E_z\\H_z\end{pmatrix}=\psi(r)e^{\pm il\theta},\qquad l=0,1,2,...\quad . \tag{A.7}$$

Then the wave equation becomes

$$\frac{\partial^2\psi}{\partial r^2}+\frac{1}{r}\frac{\partial\psi}{\partial r}+\left(k^2-\beta^2-\frac{l^2}{r^2}\right)\psi=0, \tag{A.8}$$

which is the Bessel differential equation. In general, the solutions are of the form

$$\psi(r)=\begin{cases}c_1J_l(hr)+c_2Y_l(hr), & k^2-\beta^2>0, \quad \text{in the core,}\\ c_1I_l(qr)+c_2K_l(qr), & k^2-\beta^2<0, \quad \text{in the cladding,}\end{cases} \tag{A.9}$$

where

$$h^2=k^2-\beta^2,$$

$$q^2=\beta^2-k^2.$$

Here, h and q are the magnitudes of the vectors $\mathbf{h}=\mathbf{k}-\boldsymbol{\beta}$ in the core and $\mathbf{q}=\boldsymbol{\beta}-\mathbf{k}$ in the cladding. Thus, they indicate the deviations of the core and cladding wave vectors from the propagation vector. The Bessel functions are labeled as follows

$$J_l(x)=\text{first kind,}$$

$$Y_l(x)=\text{second kind,}$$

$$I_l(x)=\text{modified first kind,}$$

$$K_l(x)=\text{modified second kind.}$$

For the modes to be confined and finite, the solutions take the form,

$$\psi(r)=\begin{cases}cJ_l(hr), & k^2-\beta^2>0,\\ cK_l(qr), & k^2-\beta^2<0.\end{cases} \tag{A.10}$$

The longitudinal components of the fields are now

$$E_z = \begin{cases} AJ_l(hr)e^{i(\omega t+l\theta-\beta z)}, & r < R_f, \\ CK_l(qr)e^{i(\omega t+l\theta-\beta z)}, & r > R_f, \end{cases} \tag{A.11a}$$

$$H_z = \begin{cases} BJ_l(hr)e^{i(\omega t+l\theta-\beta z)}, & r < R_f, \\ DK_l(qr)e^{i(\omega t+l\theta-\beta z)}, & r > R_f. \end{cases} \tag{A.11b}$$

The tangential components can be found using the Maxwell equations. Here is the work for the fields inside the core:

$$\begin{aligned} E_r(r<R_f) &= \frac{-i\beta}{\omega^2\mu\epsilon_1-\beta^2}\left(\frac{\partial}{\partial r}E_z + \frac{\omega\mu}{\beta}\frac{\partial}{r\partial\theta}H_z\right) \\ \frac{\partial}{\partial r}(E_z) &= \frac{\partial}{\partial r}\left(AJ_l(hr)e^{i(\omega t+l\theta-\beta z)}\right) \\ &= AhJ_l'(hr)e^{i(\omega t+l\theta-\beta z)}, \\ \frac{\partial}{\partial\theta}(H_z) &= \frac{\partial}{\partial\theta}\left(BJ_l(hr)e^{i(\omega t+l\theta-\beta z)}\right) \\ &= ilBJ_l(hr)e^{i(\omega t+l\theta-\beta z)}, \\ &= \frac{-i\beta}{\omega^2\mu\epsilon_1-\beta^2}\left(AhJ_l'(hr)+\frac{i\omega\mu l}{\beta r}BJ_l(hr)\right)e^{i(\omega t+l\theta-\beta z)} \\ \omega^2\mu\epsilon_1-\beta^2 &= n_1^2\omega^2\mu\epsilon_o-\beta^2 = n_1^2\left(\frac{\omega}{c}\right)^2-\beta^2 \\ &= n_1^2k^2-\beta^2 = h^2, \\ &= \frac{-i\beta}{h^2}\left(AhJ_l'(hr)+\frac{i\omega\mu l}{\beta r}BJ_l(hr)\right)e^{i(\omega t+l\theta-\beta z)}. \end{aligned}$$

$$\begin{aligned} E_\theta(r<R_f) &= -\frac{i\beta}{h^2}\left(\frac{\partial}{r\partial\theta}E_z - \frac{\omega\mu}{\beta}\frac{\partial}{\partial r}H_z\right) \\ \frac{\partial}{\partial\theta}(E_z) &= \frac{\partial}{\partial\theta}\left(AJ_l(hr)e^{i(\omega t+l\theta-\beta z)}\right) \\ &= ilAJ_l(hr)e^{i(\omega t+l\theta-\beta z)}, \\ \frac{\partial}{\partial r}(H_z) &= \frac{\partial}{\partial r}\left(BJ_l(hr)e^{i(\omega t+l\theta-\beta z)}\right) \\ &= BhJ_l'(hr)e^{i(\omega t+l\theta-\beta z)}, \\ &= -\frac{i\beta}{h^2}\left(\frac{il}{r}AJ_l(hr)-\frac{\omega\mu}{\beta}BhJ_l'(hr)\right)e^{i(\omega t+l\theta-\beta z)}. \end{aligned}$$

$$\begin{aligned} H_r(r<R_f) &= -\frac{i\beta}{h^2}\left(\frac{\partial}{\partial r}H_z - \frac{\omega\epsilon_1}{\beta}\frac{\partial}{r\partial\theta}E_z\right) \\ &= -\frac{i\beta}{h^2}\left(BhJ_l'(hr) - \frac{i\omega\epsilon_1 l}{\beta r}AJ_l(hr)\right)e^{i(\omega t+l\theta-\beta z)}. \end{aligned}$$

$$\begin{aligned} H_\theta(r<R_f) &= -\frac{i\beta}{h^2}\left(\frac{\partial}{r\partial\theta}H_z + \frac{\omega\epsilon_1 l}{\beta}\frac{\partial}{\partial r}E_z\right) \\ &= -\frac{i\beta}{h^2}\left(\frac{il}{r}BJ_l(hr) + \frac{\omega\epsilon_1}{\beta}AhJ_l'(hr)\right)e^{i(\omega t+l\theta-\beta z)}. \end{aligned}$$

The fields outside of the core are found in the same manner using

$$q^2 = \beta^2 - \omega^2\mu\epsilon_2. \tag{A.12}$$

All of the fields are

for the core ($r < R_f$),

$$E_r = -\frac{i\beta}{h^2}\left(AhJ_l'(hr) + \frac{i\omega\mu l}{\beta r}BJ_l(hr)\right)\cos(\omega t + l\theta - \beta z), \tag{A.13a}$$

$$E_\theta = \frac{\beta}{h^2}\left(\frac{il}{r}AJ_l(hr) - \frac{\omega\mu}{\beta}BhJ_l'(hr)\right)\sin(\omega t + l\theta - \beta z), \tag{A.13b}$$

$$E_z = AJ_l(hr)\cos(\omega t + l\theta - \beta z), \tag{A.13c}$$

$$H_r = \frac{\beta}{h^2}\left(BhJ_l'(hr) - \frac{i\omega\epsilon_1 l}{\beta r}AJ_l(hr)\right)\sin(\omega t + l\theta - \beta z), \tag{A.13d}$$

$$H_\theta = -\frac{i\beta}{h^2}\left(\frac{il}{r}BJ_l(hr) + \frac{\omega\epsilon_1}{\beta}AhJ_l'(hr)\right)\cos(\omega t + l\theta - \beta z), \tag{A.13e}$$

$$H_z = BJ_l(hr)\cos(\omega t + l\theta - \beta z), \tag{A.13f}$$

and for the cladding ($r > R_f$),

$$E_r = \frac{i\beta}{q^2}\left(CqK_l'(qr) + \frac{i\omega\mu l}{\beta r}DK_l(qr)\right)\cos(\omega t + l\theta - \beta z), \tag{A.14a}$$

$$E_\theta = -\frac{\beta}{q^2}\left(\frac{il}{r}CK_l(qr) - \frac{\omega\mu}{\beta}DqK_l'(qr)\right)\sin(\omega t + l\theta - \beta z), \tag{A.14b}$$

$$E_z = CK_l(qr)\cos(\omega t + l\theta - \beta z), \tag{A.14c}$$

$$H_r = -\frac{\beta}{q^2}\left(DqK_l'(qr) - \frac{i\omega\epsilon_2 l}{\beta r}CK_l(qr)\right)\sin(\omega t + l\theta - \beta z), \tag{A.14d}$$

$$H_\theta = \frac{i\beta}{q^2}\left(\frac{il}{r}DK_l(qr) + \frac{\omega\epsilon_2}{\beta}CqK_l'(qr)\right)\cos(\omega t + l\theta - \beta z), \tag{A.14e}$$

$$H_z = DK_l(qr)\cos(\omega t + l\theta - \beta z), \tag{A.14f}$$

where the convention is used that the tangential components of the electric field are real and the longitudinal components are imaginary. This requires A and C to be imaginary, and B and D to be real. A can be chosen to be imaginary, and the other amplitudes are calculated from A using the boundary conditions.

A.1 Boundary Conditions

The boundary conditions that are used to calculate B, C, and D from A are the continuity of the θ and z-components of the fields.

$E_\theta|_{r\to R_f^-} = E_\theta|_{r\to R_f^+}$,

$$-\frac{i\beta}{h^2}\left(AhJ_l'(hR_f) + \frac{i\omega\mu l}{\beta R_f}BJ_l(hR_f)\right) = \frac{i\beta}{q^2}\left(CqK_l'(qR_f) + \frac{i\omega\mu l}{\beta R_f}DK_l(qR_f)\right),$$

$$A\left(\frac{il}{h^2R_f}J_l(hR_f)\right) + B\left(-\frac{\omega\mu}{h\beta}J_l'(hR_f)\right) + C\left(\frac{il}{q^2R_f}K_l(qR_f)\right) + D\left(-\frac{\omega\mu}{q\beta}K_l'(qR_f)\right) = 0. \tag{A.15}$$

$E_z|_{r\to R_f^-} = E_z|_{r\to R_f^+}$,

$$AJ_l(hR_f) = CK_l(qR_f),$$

$$AJ_l(hR_f) - CK_l(qR_f) = 0. \tag{A.16}$$

$H_\theta|_{r\to R_f^-} = H_\theta|_{r\to R_f^+}$,

$$-\frac{i\beta}{h^2}\left(\frac{il}{R_f}BJ_l(hR_f) + \frac{\omega\epsilon_1}{\beta}AhJ_l'(hR_f)\right) = \frac{i\beta}{q^2}\left(\frac{il}{R_f}DK_l(qR_f) + \frac{\omega\epsilon_2}{\beta}CqJ_l'(qR_f)\right),$$

$$A\left(\frac{\omega\epsilon_1}{h\beta}J_l'(hR_f)\right) + B\left(\frac{il}{h^2R_f}J_l(hR_f)\right) + C\left(\frac{\omega\epsilon_2}{q\beta}K_l'(qR_f)\right) + D\left(\frac{il}{q^2R_f}K_l(qR_f)\right) = 0. \tag{A.17}$$

$H_z|_{r\to R_f^-} = H_z|_{r\to R_f^+}$,

$$BJ_l(hr) = DK_l(qr),$$

$$BJ_l(hR_f) - DK_l(qR_f) = 0. \tag{A.18}$$

From Eq. (A.16),

$$\frac{C}{A} = \frac{J_l(hR_f)}{K_l(qR_f)}. \tag{A.19}$$

From Eq. (A.18),

$$\frac{D}{B} = \frac{J_l(hR_f)}{K_l(qR_f)}. \tag{A.20}$$

Now, combining Eqs. (A.15), (A.19), and (A.20)

$$A\left(\frac{il}{h^2R_f}J_l(hR_f)\right) - B\left(\frac{\omega\mu}{h\beta}J_l'(hR_f)\right) + A\left(\frac{J_l(hR_f)}{K_l(qR_f)}\frac{il}{q^2R_f}K_l(qR_f)\right) - B\left(\frac{J_l(hR_f)}{K_l(qR_f)}\frac{\omega\mu}{q\beta}K_l'(qR_f)\right) = 0,$$

$$A\left(\frac{il}{h^2R_f}J_l(hR_f) + \frac{il}{q^2R_f}J_l(hR_f)\right) - B\left(\frac{\omega\mu}{h\beta}J_l'(hR_f) + \frac{\omega\mu}{q\beta}\frac{J_l(hR_f)}{K_l(qR_f)}K_l'(qR_f)\right) = 0,$$

$$AJ_l(hR_f)\frac{il}{R_f}\left(\frac{1}{h^2}+\frac{1}{q^2}\right)=B\frac{\omega\mu}{\beta}\left(\frac{1}{h}J_l'(hR_f)+\frac{1}{q}\frac{J_l(hR_f)}{K_l(qR_f)}K_l'(qR_f)\right),$$

$$\frac{B}{A}=\frac{J_l(hR_f)\frac{il}{R_f}\left(\frac{1}{h^2}+\frac{1}{q^2}\right)}{\frac{\omega\mu}{\beta}\left(\frac{1}{h}J_l'(hR_f)+\frac{1}{q}\frac{J_l(hR_f)}{K_l(qR_f)}K_l'(qR_f)\right)},$$

$$\frac{B}{A}=\frac{i\beta l}{R_f\omega\mu}\left(\frac{1}{h^2}+\frac{1}{q^2}\right)\left(\frac{J_l'(hR_f)}{hJ_l(hR_f)}+\frac{K_l'(qR_f)}{qK_l(qR_f)}\right)^{-1},$$

$$\frac{B}{A}=\frac{i\beta l}{\omega\mu}\left(\frac{1}{(hR_f)^2}+\frac{1}{(qR_f)^2}\right)\left(\frac{J_l'(hR_f)}{hR_fJ_l(hR_f)}+\frac{K_l'(qR_f)}{qR_fK_l(qR_f)}\right)^{-1}. \tag{A.21}$$

Finally, the equations used to calculate B, C, and D from A are

$$\frac{B}{A}=\frac{i\beta l}{\omega\mu}\left(\frac{1}{(hR_f)^2}+\frac{1}{(qR_f)^2}\right)\left(\frac{J_l'(hR_f)}{hR_fJ_l(hR_f)}+\frac{K_l'(qR_f)}{qR_fK_l(qR_f)}\right)^{-1}, \tag{A.22a}$$

$$\frac{C}{A}=\frac{J_l(hR_f)}{K_l(qR_f)}, \tag{A.22b}$$

$$\frac{D}{B}=\frac{J_l(hR_f)}{K_l(qR_f)}. \tag{A.22c}$$

A.2 Propagation Constants

Modes occur when all the boundary conditions are met. This requires that the boundary condition matrix has a determinant of zero. In matrix form, the boundary conditions are

$$\begin{pmatrix} \frac{il}{h^2R_f}J_l(hR_f) & -\frac{\omega\mu}{h\beta}J_l'(hR_f) & \frac{il}{q^2R_f}K_l(qR_f) & -\frac{\omega\mu}{q\beta}K_l'(qR_f) \\ J_l(hR_f) & 0 & -K_l(qR_f) & 0 \\ \frac{\omega\epsilon_1}{h\beta}J_l'(hR_f) & \frac{il}{h^2R_f}J_l(hR_f) & \frac{\omega\epsilon_2}{q\beta}K_l'(qR_f) & \frac{il}{q^2R_f}K_l(qR_f) \\ 0 & J_l(hR_f) & 0 & -K_l(qR_f) \end{pmatrix}\begin{pmatrix} A \\ B \\ C \\ D \end{pmatrix}=0. \tag{A.23}$$

Setting the determinant to zero and dropping the arguments of the Bessel functions:

$$-\frac{JK\mu\omega^2\epsilon_1 J'K'}{\beta^2 hq} - \frac{JK\mu\omega^2\epsilon_2 J'K'}{\beta^2 hq} + \frac{J^2K^2l^2}{R_f^2h^4} + \frac{J^2K^2l^2}{R_f^2q^4} + \frac{2J^2K^2l}{R_f^2h^2q^2} - \frac{K^2\mu\omega^2\epsilon_1 J'^2}{\beta^2h^2} - \frac{J^2\mu\omega^2\epsilon_2 K'^2}{\beta^2q^2} = 0,$$

$$-\frac{JK\mu\omega^2 J'K'}{\beta^2 hq}(\epsilon_1+\epsilon_2) + \frac{J^2K^2l^2}{R_f^2}\underbrace{\left(\frac{1}{h^4}+\frac{1}{q^4}+\frac{2}{h^2q^2}\right)}_{\left(\left(\frac{1}{h}\right)^2+\left(\frac{1}{q}\right)^2\right)^2} - \frac{\mu\omega^2}{\beta^2}\left(\frac{K^2\epsilon_1 J'^2}{h^2}+\frac{J^2\epsilon_2 K'^2}{q^2}\right) = 0,$$

$$\frac{JK\mu\omega^2 J'K'}{\beta^2 hq}(\epsilon_1+\epsilon_2) + \frac{\mu\omega^2}{\beta^2}\left(\frac{K^2\epsilon_1 J'^2}{h^2}+\frac{J^2\epsilon_2 K'^2}{q^2}\right) = \frac{J^2K^2l^2}{R_f^2}\left(\left(\frac{1}{h}\right)^2+\left(\frac{1}{q}\right)^2\right)^2,$$

$$\frac{\mu\omega^2 J'K'}{JKhqR_f^2}\epsilon_o\left(n_1^2+n_2^2\right) + \mu\omega^2\left(\frac{n_1^2J'^2}{(hR_f)^2J^2}+\frac{n_2^2K'^2}{(qR_f)^2K^2}\right) = l^2\left(\left(\frac{1}{hR_f}\right)^2+\left(\frac{1}{qR_f}\right)^2\right)^2\beta^2.$$

Because

$$\epsilon_o = \frac{1}{\mu c^2} = \frac{1}{\mu(\omega/k_o)^2} = \frac{k_o^2}{\mu\omega^2},$$

this becomes

$$\frac{J'K'}{JKhqR_f^2}\left(n_1^2+n_2^2\right) + \frac{n_1^2J'^2}{(hR_f)^2J^2} + \frac{n_2^2K'^2}{(qR_f)^2K^2} = l^2\left(\left(\frac{1}{hR_f}\right)^2+\left(\frac{1}{qR_f}\right)^2\right)^2\left(\frac{\beta}{k_o}\right)^2,$$

$$\left(\frac{J'}{hR_fJ}+\frac{K'}{qR_fK}\right)\left(\frac{n_1J'}{hR_fJ}+\frac{n_2K'}{qR_fK}\right)=l^2\left(\left(\frac{1}{hR_f}\right)^2+\left(\frac{1}{qR_f}\right)^2\right)^2\left(\frac{\beta}{k_o}\right)^2.$$

With the arguments it follows that

$$\left(\frac{J_l'(hR_f)}{hR_fJ_l(hR_f)}+\frac{K_l'(qR_f)}{qR_fK_l(qR_f)}\right)\left(\frac{n_1J_l'(hR_f)}{hR_fJ_l(hR_f)}+\frac{n_2K_l'(qR_f)}{qR_fK(qR_f)}\right)$$
$$=l^2\left(\left(\frac{1}{hR_f}\right)^2+\left(\frac{1}{qR_f}\right)^2\right)^2\left(\frac{\beta}{k_o}\right)^2. \quad \text{(A.24)}$$

Because h and q are dependent on the propagation constant β, Eq. (A.24) can be used to calculate the propagation constants. The solutions are found and classified by solving Eq. (A.24) for

$$\frac{J_l'(hR_f)}{hR_fJ_l(hR_f)}.$$

Slightly rewriting Eq. (A.24) as

$$n_1^2\left(\frac{J'}{hR_fJ}\right)^2+\left(n_1^2+n_2^2\right)\frac{K'}{qR_fK}\left(\frac{J'}{hR_fJ}\right)+n_2^2\left(\frac{K'}{qR_fK}\right)^2$$
$$-l^2\left(\left(\frac{1}{hR_f}\right)^2+\left(\frac{1}{qR_f}\right)^2\right)^2\left(\frac{\beta}{k_o}\right)^2=0, \quad \text{(A.25)}$$

and solving Eq. (A.25) results in

$$\frac{J'}{hR_fJ} = -\frac{(n_1^2+n_2^2)}{2n_1^2}\frac{K'}{qR_fK} \pm \frac{1}{2n_1^2}\Bigg\{\left(n_1^2+n_2^2\right)^2\left(\frac{K'}{qR_fK}\right)^2 - 4n_1^2\left[n_2^2\left(\frac{K'}{qR_fK}\right)^2 - l^2\left(\frac{1}{h^2R_f^2}+\frac{1}{q^2R_f^2}\right)^2\left(\frac{\beta}{k_o}\right)^2\right]\Bigg\}^{1/2},$$

$$\frac{J'}{hR_fJ} = -\frac{(n_1^2+n_2^2)}{2n_1^2}\frac{K'}{qR_fK} \pm \frac{1}{2n_1^2}\sqrt{(n_1^4-2n_1^2n_2^2+n_2^4)\left(\frac{K'}{qR_fK}\right)^2 + 4n_1^2l^2\left(\frac{\beta}{k_o}\right)^2\left(\frac{1}{h^2R_f^2}+\frac{1}{q^2R_f^2}\right)^2},$$

$$\frac{J'}{hR_fJ} = -\frac{(n_1^2+n_2^2)}{2n_1^2}\frac{K'}{qR_fK} \pm \sqrt{\left(\frac{n_1^4-2n_1^2n_2^2+n_2^4}{4n_1^4}\right)\left(\frac{K'}{qR_fK}\right)^2 + \frac{l^2}{n_1^2}\left(\frac{\beta}{k_o}\right)^2\left(\frac{1}{h^2R_f^2}+\frac{1}{q^2R_f^2}\right)^2},$$

$$\frac{J'}{hR_fJ} = -\left(\frac{n_1^2+n_2^2}{2n_1^2}\right)\frac{K'}{qR_fK} \pm \sqrt{\left(\frac{n_1^2-n_2^2}{2n_1^2}\right)^2\left(\frac{K'}{qR_fK}\right)^2 + \frac{l^2}{n_1^2}\left(\frac{\beta}{k_o}\right)^2\left(\frac{1}{h^2R_f^2}+\frac{1}{q^2R_f^2}\right)^2}. \tag{A.26}$$

Using the recurrence relations

$$J_l'(x) = -J_{l+1}(x) + \frac{l}{x}J_l(x),$$
$$J_l'(x) = J_{l-1}(x) - \frac{l}{x}J_l(x),$$

the solutions are for the EH modes,

$$\frac{J_{l+1}(hR_f)}{hR_fJ_l(hR_f)} = \frac{n_1^2+n_2^2}{2n_1^2}\frac{K_l'(qR_f)}{qR_fK_l(qR_f)} + \left(\frac{l}{(hR_f)^2} - R\right), \tag{A.28}$$

and for the HE modes,

$$\frac{J_{l-1}(hR_f)}{hR_fJ_l(hR_f)} = -\frac{n_1^2+n_2^2}{2n_1^2}\frac{K_l'(qR_f)}{qR_fK_l(qR_f)} + \left(\frac{l}{(hR_f)^2} - R\right), \tag{A.29}$$

where

$$R = \sqrt{\left(\frac{n_1^2-n_2^2}{2n_1^2}\right)^2\left(\frac{K_l'(qR_f)}{qR_fK_l(qR_f)}\right)^2 + \frac{l^2}{n_1^2}\left(\frac{\beta}{k_o}\right)^2\left(\frac{1}{h^2R_f^2}+\frac{1}{q^2R_f^2}\right)^2}. \tag{A.30}$$

When $l = 0$, the EH and HE modes are reduced to TM and TE modes, respectively, and their characteristic equations are

TM modes,

$$\frac{J_1(hR_f)}{hR_fJ_0(hR_f)} = -\frac{n_2^2}{n_1^2}\frac{K_1(qR_f)}{qR_fK_0(qR_f)}, \tag{A.31}$$

and TE modes,

$$\frac{J_1(hR_f)}{hR_fJ_0(hR_f)} = -\frac{K_1(qR_f)}{qR_fK_0(qR_f)}. \tag{A.32}$$

APPENDIX B

RECIPROCITY RELATION

The reciprocity relation is a tool for relating the fields of two electromagnetic modes. In this derivation, the modes are allowed to have different permittivity profiles ϵ_1 and ϵ_2. Maxwell equations in general form,

$$\nabla \times \mathbf{E} = ik\sqrt{\frac{\mu_0}{\epsilon_0}}\mathbf{H}, \tag{B.1}$$

$$\nabla \times \mathbf{H} = \mathbf{J} - ik\epsilon\sqrt{\frac{\mu_0}{\epsilon_0}}\mathbf{E}, \tag{B.2}$$

and the vector identity in general form,

$$\nabla \cdot (\mathbf{A} \times \mathbf{B}) = \mathbf{B} \cdot (\nabla \times \mathbf{A}) - \mathbf{A} \cdot (\nabla \times \mathbf{B}), \tag{B.3}$$

are used to find the reciprocity relation.

$$\begin{aligned}
&\nabla \cdot (\mathbf{E}_1 \times \mathbf{H}_2^*) \\
&\quad = \nabla \cdot \left(\mathbf{E}_1 \times \frac{i}{k}\sqrt{\frac{\epsilon_0}{\mu_0}}(\nabla \times \mathbf{E}_2^*) \right) \\
&\quad = \frac{i}{k}\sqrt{\frac{\epsilon_0}{\mu_0}}(\nabla \times \mathbf{E}_2^*) \cdot (\nabla \times \mathbf{E}_1) - \mathbf{E}_1 \cdot \left(\nabla \times \frac{i}{k}\sqrt{\frac{\epsilon_0}{\mu_0}}(\nabla \times \mathbf{E}_2^*) \right) \\
&\quad = \frac{i}{k}\sqrt{\frac{\epsilon_0}{\mu_0}} \left(-ik\sqrt{\frac{\mu_0}{\epsilon_0}}\mathbf{H}_2^* \right) \cdot \left(ik\sqrt{\frac{\mu_0}{\epsilon_0}}\mathbf{H}_1 \right) - \mathbf{E}_1 \cdot \left(\nabla \times \frac{i}{k}\sqrt{\frac{\epsilon_0}{\mu_0}}(\nabla \times \mathbf{E}_2^*) \right) \\
&\quad = ik\sqrt{\frac{\mu_0}{\epsilon_0}}\mathbf{H}_1\mathbf{H}_2^* - \frac{i}{k}\sqrt{\frac{\epsilon_0}{\mu_0}}\mathbf{E}_1 \cdot (\nabla \times \nabla \times \mathbf{E}_2^*) \\
&\quad = ik\sqrt{\frac{\mu_0}{\epsilon_0}}\mathbf{H}_1\mathbf{H}_2^* - \frac{i}{k}\sqrt{\frac{\epsilon_0}{\mu_0}}\mathbf{E}_1 \cdot \left(\nabla \times \left(-ik\sqrt{\frac{\mu_0}{\epsilon_0}}\mathbf{H}_2^* \right) \right) \\
&\quad = ik\sqrt{\frac{\mu_0}{\epsilon_0}}\mathbf{H}_1\mathbf{H}_2^* - \mathbf{E}_1 \cdot \left(\mathbf{J}_2^* + ik\epsilon_2\sqrt{\frac{\epsilon_0}{\mu_0}}\mathbf{E}_2^* \right) \\
&\quad = ik\sqrt{\frac{\mu_0}{\epsilon_0}}\mathbf{H}_1\mathbf{H}_2^* - ik\sqrt{\frac{\epsilon_0}{\mu_0}}\epsilon_2\mathbf{E}_1\mathbf{E}_2^* - \mathbf{E}_1 \cdot \mathbf{J}_2^*.
\end{aligned} \tag{B.4}$$

$$
\begin{aligned}
&\nabla \cdot (\mathbf{E}_2^* \times \mathbf{H}_1) \\
&\quad = -\nabla \cdot \left(\mathbf{E}_2^* \times \frac{i}{k} \sqrt{\frac{\epsilon_0}{\mu_0}} (\nabla \times \mathbf{E}_1) \right) \\
&\quad = -\frac{i}{k} \sqrt{\frac{\epsilon_0}{\mu_0}} (\nabla \times \mathbf{E}_1) \cdot (\nabla \times \mathbf{E}_2^*) + \mathbf{E}_2^* \cdot \left(\nabla \times \frac{i}{k} \sqrt{\frac{\epsilon_0}{\mu_0}} (\nabla \times \mathbf{E}_1) \right) \\
&\quad = -\frac{i}{k} \sqrt{\frac{\epsilon_0}{\mu_0}} \left(-ik \sqrt{\frac{\mu_0}{\epsilon_0}} \mathbf{H}_1 \right) \cdot \left(ik \sqrt{\frac{\mu_0}{\epsilon_0}} \mathbf{H}_2^* \right) + \mathbf{E}_2^* \cdot \left(\nabla \times \frac{i}{k} \sqrt{\frac{\epsilon_0}{\mu_0}} (\nabla \times \mathbf{E}_1) \right) \\
&\quad = -\frac{i}{k} \sqrt{\frac{\epsilon_0}{\mu_0}} \mathbf{H}_1 \mathbf{H}_2^* + \frac{i}{k} \sqrt{\frac{\epsilon_0}{\mu_0}} \mathbf{E}_2^* \cdot (\nabla \times \nabla \times \mathbf{E}_1) \\
&\quad = -ik \sqrt{\frac{\mu_0}{\epsilon_0}} \mathbf{H}_1 \mathbf{H}_2^* + \frac{i}{k} \sqrt{\frac{\epsilon_0}{\mu_0}} \mathbf{E}_2^* \cdot \left(\nabla \times \left(ik \sqrt{\frac{\mu_0}{\epsilon_0}} \mathbf{H}_1 \right) \right) \\
&\quad = -ik \sqrt{\frac{\mu_0}{\epsilon_0}} \mathbf{H}_1 \mathbf{H}_2^* - \mathbf{E}_2^* \cdot \left(\mathbf{J}_1 - ik\epsilon_1 \sqrt{\frac{\epsilon_0}{\mu_0}} \mathbf{E}_1 \right) \\
&\quad = -ik \sqrt{\frac{\mu_0}{\epsilon_0}} \mathbf{H}_1 \mathbf{H}_2^* + ik \sqrt{\frac{\epsilon_0}{\mu_0}} \epsilon_1 \mathbf{E}_1 \mathbf{E}_2^* - \mathbf{E}_2^* \cdot \mathbf{J}_1.
\end{aligned} \tag{B.5}
$$

The reciprocity relation, found by combining Eqs. (B.4) and (B.5), is

$$
\nabla \cdot (\mathbf{E}_1 \times \mathbf{H}_2^* + \mathbf{E}_2^* \times \mathbf{H}_1) = i\omega(\epsilon_1 - \epsilon_2) \mathbf{E}_1 \cdot \mathbf{E}_2^* - (\mathbf{E}_2^* \cdot \mathbf{J}_1 + \mathbf{E}_1 \cdot \mathbf{J}_2^*). \tag{B.6}
$$

For a source-free system, the reciprocity relation reduces to

$$
\nabla \cdot (\mathbf{E}_1 \times \mathbf{H}_2^* + \mathbf{E}_2^* \times \mathbf{H}_1) = i\omega(\epsilon_1 - \epsilon_2) \mathbf{E}_1 \cdot \mathbf{E}_2^*. \tag{B.7}
$$

This can be expressed in integral form over an infinitesimal range Δz in the direction of propagation:

$$
\begin{aligned}
\frac{\partial}{\partial z} \iint (\mathbf{E}_1 \times \mathbf{H}_2^* + \mathbf{E}_2^* \times \mathbf{H}_1) \cdot \hat{z} \, \mathrm{d}x \, \mathrm{d}y \\
= i\omega \iint (\epsilon_1(x, y) - \epsilon_2(x, y)) \mathbf{E}_1 \cdot \mathbf{E}_2^* \, \mathrm{d}x \, \mathrm{d}y.
\end{aligned} \tag{B.8}
$$

APPENDIX C

RING CAVITY MODEL

The fiber-coupled microsphere may be modeled as a ring cavity with one reflecting mirror. Because the coupling coefficients κ_{sf} and κ_{fs} are generally not equal, the intracavity field must be calculated in a slightly different way than usual. The field strength in the microsphere after N passes is given, on resonance, by

$$E_s = \underbrace{t_{sf} E_f \left(}_{\text{incident}} \underbrace{1}_{} + \underbrace{r_{fs}\, e^{i\delta}}_{\text{one}} + \underbrace{\left(r_{fs}\, e^{i\delta}\right)^2}_{\text{two}} + \ldots + \underbrace{\left(r_{fs}\, e^{i\delta}\right)^N}_{\text{round trips}} \Bigg), \tag{C.1}$$

where t_{sf} is the transmission coefficient when light passes from the fiber into the sphere, r_{fs} is the reflection coefficient when light inside of the sphere is internally reflected when incident with the fiber, and δ is the phase shift upon refection. Because the coupling coefficients indicate the probability of a photon to tunnel between waveguides, they are equivalent to transmission coefficients. The microsphere is field is calculated by summing over an infinite number of round trips and by replacing t_{sf} with $|\tilde{\kappa}_{sf}|$ and r_{fs} with $\sqrt{1-|\tilde{\kappa}_{fs}|^2}$. Assuming, with no loss of generality, that there is no phase shift upon reflection, the result is

$$\begin{aligned} E_s &= \sum_{N=0}^{\infty} (|\tilde{\kappa}_{sf}| E_f) \left(\sqrt{1-|\tilde{\kappa}_{fs}|^2}\right)^N \\ &= \frac{|\tilde{\kappa}_{sf}| E_f}{1-\sqrt{1-|\tilde{\kappa}_{fs}|^2}}. \end{aligned} \tag{C.2}$$

For small coupling coefficients, the binomial expansion may be used to approximate the field. The microsphere field then becomes

$$\begin{aligned} E_s &\cong \frac{|\tilde{\kappa}_{sf}| E_f}{1-\left(1-\frac{1}{2}|\tilde{\kappa}_{fs}|^2\right)} \\ &\cong \left(\frac{2|\tilde{\kappa}_{sf}|}{|\tilde{\kappa}_{fs}|^2}\right) E_f. \end{aligned} \tag{C.3}$$

VITA

MICHAEL JOSEPH HUMPHREY

Candidate for the Degree of

Doctor of Philosophy

Thesis: CALCULATION OF COUPLING BETWEEN TAPERED FIBER MODES AND WHISPERING-GALLERY MODES OF A SPHERICAL MICRO-LASER

Major Field: Physics

Biographical:

Personal Data: Born in Maryland on May 15, 1972.

Education: Received Bachelor of Science degree with Honors in Physics from The University of Maryland, College Park, MD in May 1994; Completed the requirements for the Doctor of Philosophy degree with a major in Physics at Oklahoma State University in July 2004.

Experience: Science and Engineering Apprentice, Harry Diamond Laboratories/DoD. (George Washington University Science and Engineering Apprenticeship Program) from 1989–1990. Science/Engineering Technician, Science Systems and Applications, Inc. (Contract support to NASA/Goddard Space Flight Center, Greenbelt, MD) from 1991–1994. Scientist/Engineer, Science Systems and Applications, Inc. (Contract support to NASA/ Goddard Space Flight Center, Greenbelt, MD) from 1994–1995. Employed by Oklahoma State University, Department of Physics, as a graduate teaching assistant and graduate research assistant from 1995–present.

Professional Membership: Optical Society of America.

Name: Michael Joseph Humphrey Date of Degree: July 2004

Institution: Oklahoma State University Location: Stillwater, Oklahoma

Title of Study: CALCULATION OF COUPLING BETWEEN TAPERED FIBER MODES AND WHISPERING-GALLERY MODES OF A SPHERICAL MICROLASER

Pages in Study: 96 Candidate for the Degree of Doctor of Philosophy

Major Field: Physics

Scope and Method of Study: Coupled-mode theory is used to numerically calculate the coupling coefficients between modes of a tapered fiber and those of a fused-silica microsphere. The coupling coefficients are used to determine the optimal fiber taper radius. They are also used to calculate whispering-gallery mode spectra that take into account the eccentricity of the microsphere and the fact that in an experiment the tapered fiber is not necessarily perfectly aligned with the equatorial plane of the microsphere. The spectra are used to model multimode lasing in a microsphere.

Findings and Conclusions: The calculations of optimal fiber radii indicate that the highest coupling from a fundamental fiber mode to a sphere mode is achieved with a fiber that has a radius somewhat smaller (about 30%) than for perfect phase matching. For fibers of this size, the coupling is about twice as strong as when phase-matched. Another advantage of using the smaller sizes is that losses to higher-order fiber modes is substantial for phase-matched sizes. Also, the calculations indicate that coupling to the microsphere TE modes is stronger than to the TM modes. This is a result of the longitudinal field overlap present when coupling into TM modes.

The calculation of WGM spectra shows that there are many possible modes that can be coupled within one free-spectral range of the microsphere. The calculated values of the coupling coefficients are consistent with experimental data. With the fiber laterally offset from, but still parallel to the equatorial plane of the microsphere, the coupling to the fundamental polar mode is not as strong as to some of the higher-order polar modes. This is in agreement with experimental data and is a result of higher-order polar modes having more polar extent. The inclusion of eccentricity and lateral offset enables the numerical calculations to be directly compared to experiment. These calculations are then valuable both for designing experiments and interpreting the resulting data.

The WGM spectra have been used to develop a laser model for a coated microsphere. Nonlinear threshold behavior is found by including the effects of mode competition.

ADVISOR'S APPROVAL: Donna K. Bandy